Integrated Bragg Grating and Carbon Nanotube Devices Using UV-Written Silica-Based Planar Waveguides

(紫外光描画石英系平面導波路によるブラッググレーティングとカーボンナノチューブ集積デバイス)

by

Ken Kashiwagi

A Thesis Submitted in Partial Fulfillment of
the Requirements for the Degree of
Doctor of Engineering

Department of Electronic Engineering
School of Engineering
The University of Tokyo

Supervisor : Shinji Yamashita Associate Professor

December 2006

Table of Contents

Chapter 1 : Introduction

1.1 Prologue

Silica-based optical planar waveguide technology is promising to realize diversified functional devices. Current requirements for optical devices are flexibility and cost effective fabrication. Ultra violet (UV)-written silica-based planar waveguide devices are alternative option which may meat the requirements. We first investigate UV-written waveguide structures for future highly functional devices. Sampled Bragg grating-contained waveguides are fabricated by UV beam fabrication technique.

Although silica-based waveguide devices have many advantages, they have less tunability than semiconductor-based devices. Recently, carbon nanotubes (CNTs) for optical device applications are attracted much attention because of their distinctive features as an optical material. Structures of conventional devices based on CNTs are all bulky, and they have difficulty in integration. Another difficulty of CNT-based optical devices is the difficulty of CNT handling. Hybridization of silica-based optical waveguides and CNT devices are investigated in order to achieve synergistic effects of the two and compensate their disadvantages with each other. Furthermore, a novel handling method of CNTs is proposed.

1.2 Research Backgrounds and Motivation

Scientists have intensively investigated the optical communication after the invention of laser to employ higher frequency of lights than that of microwaves. In 1970, the two historic inventions were made, thereby optical communication technology has been developed in drastic speed since then. One was low loss optical fiber (20dB/km) developed by Corning Corporation, and the other was continuous wave oscillation of a semiconductor laser in room temperature explored by Bell Laboratory. These two

innovations have brought us the optical communication which can transmit data in much higher bit-rates than electric communication.

Enhancing the data rate have been realized by densifying the data in time domain, and a recent data rate in research stage reaches the data rate of 160 Giga Bit/sec (Gbps), 640Gbps or even higher [1]. However, high data rate systems require electronic components which can handle high frequency as high as 100GHz, and these components make the system cost higher. To increase the data transmission capacity for single optical fiber in low cost, wavelength devision multiplexing (WDM) technique, where the lights which have different wavelengths and signals with each other are transmitted in a single optical fiber, was invented. Although the loss of optical fiber was reached almost the theoretic limit ($\sim$ 0.153dB/km at 1.55 μm), the loss limits the transmission length and is not low enough for submarine systems that enables intercontinental communication networks without repeaters. Invention of Er doped fiber amplifier (EDFA) allowed us to realize the submarine system by WDM system in low cost because EDFA can simultaneously amplify multichannels without converting the optical signals into electronic signals. Densification of frequency spacing of data signals (channel spacing) in WDM systems have been improved from 100GHz to 50 or 25 GHz [2, 3] reach the maximized spectral efficiency in the EDFA gain bandwidth. Thus, optical communication systems cover and connect all over the world efficiently.

The optical communication systems were employed first in long haul systems. Recent transmission systems with much shorter span length that adopt the optical communication systems include metro networks and subscriber networks, fiber-to-the-home (FTTH) and fiber-to-the-office (FTTO). Reconfigurability and scalability of the network are required in such networks to manage the network traffic efficiently to meet with the user demands. Therefore, the networks need functional and flexible devices such as optical filters, optical add-drop multiplexers(OADMs), optical cross connects(OXCs), optical switches. Planar waveguide devices are the one of the technologies which can realize the functional devices. Silica-based waveguides have a lot of benefits, such as high compatibility with optical fibers, long term stability, and low insertion loss. Figure 1.1 shows the various devices which have been realized by

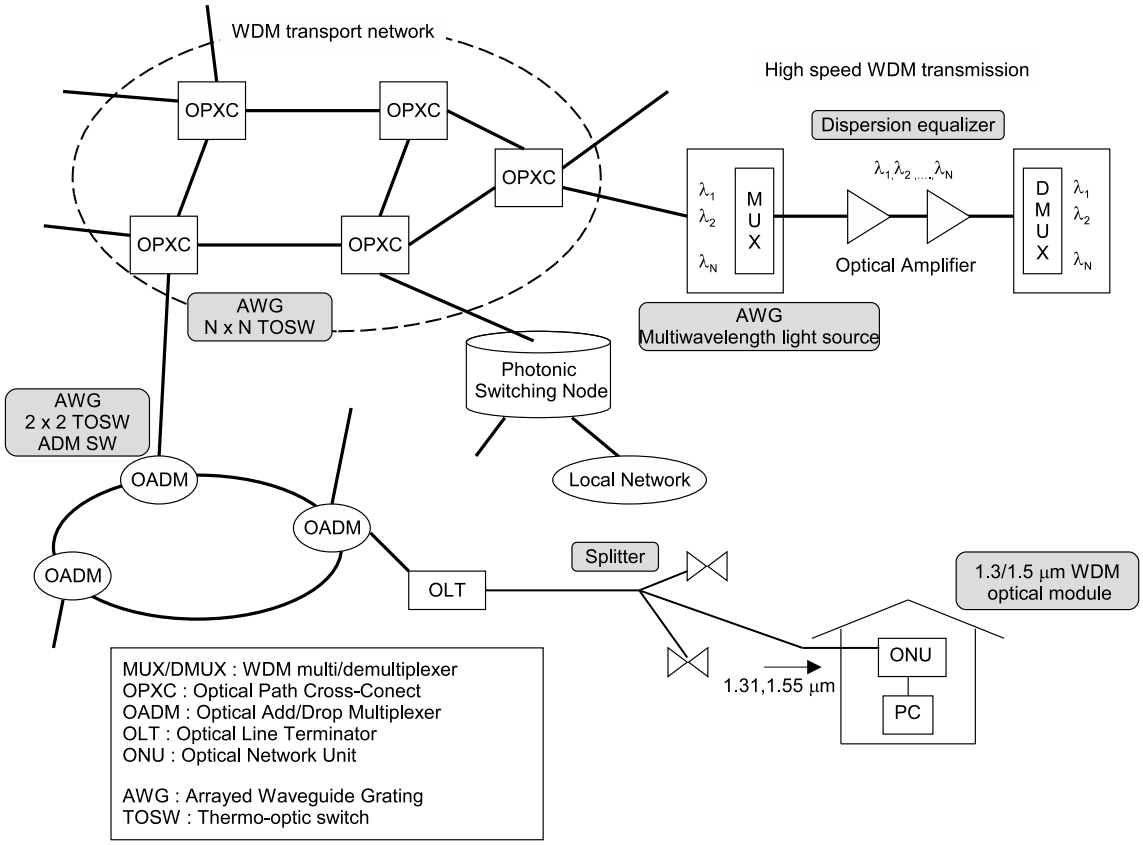

Fig. 1.1: Applications of silica-based planar optical waveguide devices [4]

silica-based waveguides [4]. Devices shadowed are the applications which include not only silica-based waveguide devices, but also the hybrids of the silica-based waveguide and semiconductor active devices. Thus, silica-based waveguide technologies are applicable to broad areas.

The silica-based waveguides have been commonly fabricated with silicon (Si) large scale integrated (LSI) circuit technology, such as lithography, etching, etc. Recently, a fabrication technique of silica-based waveguides by UV beam scanning has been studied [5]. Optical devices have to be low-cost especially for subscriber networks. Device flexibility, low cost and novel device realization are expected by the technique. The UV beam scanning technique is a main scope in this thesis.

The principle of UV beam scanning technique is the photosensitivity in silica-glass. The photosensitivity in silica-glass is occurs in Ge-doped silica-glass. We can induce

permanent refractive index change of Ge-doped silica-glass by irradiating UV beam through photosensitivity. The photosensitivity first discovered by K.O. Hill [6] and has been utilized for realizing various optical fiber-based devices, such as fiber Bragg gratings (FBGs) [7], long period fiber gratings (LPFGs) [8]. In silica-based planar waveguides, Bragg gratings are inscribed in waveguides and used as mirrors for external cavity lasers [9], and OADMs with Mach-Zehnder circuits [10]. Compensating phase errors of optical circuits originated from fabrication errors is another important usage of photosensitivity [11, 12].

Photosensitivity has a lot of usages as mentioned above. The waveguide fabrication by UV beam irradiation was first reported by Mizrahi et al. [13]. In the report, they used pulsed excimer laser source. They needed a mask for every targeted waveguide patterns, however as a result, laser beam power was not efficiently used. When the dimension of the waveguide pattern was larger than the laser beam spot, they had to scan the spot [14] because it is difficult to obtain wide and uniform laser beam. On the other hand, a method of scanning the focused UV beam spot from a continuous wave laser has the benefits in that we can utilize laser power efficiently and fabricate the devices without patterning masks. Various waveguide patterns have already been fabricated by the technique, such as low loss waveguides [15, 16], Y-shape power splitters [17], directional couplers [18, 19], Mach-Zehnder circuit based attenuators [20], and Bragg grating written waveguides [21]. Silica-based waveguide based integrated devices have many benefits. However, one of the drawbacks of the devices is small tunability. Tunable devices can be realized only by thermo-optic (TO) effect have the response time is slow ($\sim$10msec), so that the devices cannot be employed in future high speed communication systems.

Recently, carbon nanotubes (CNTs) emerged as a novel attractive material for photonics devices. The material has attractive features, such as mechanical and chemical stability, fabrication simplicity, easy attachment and embedding, small footprint, high third order nonlinearity, ultrafast saturable absorption, and ultrafast recovery time. Optical properties of CNTs have been investigated by many researchers, and saturable absorber applications were demonstrated [22–24]. However, the device structures were all

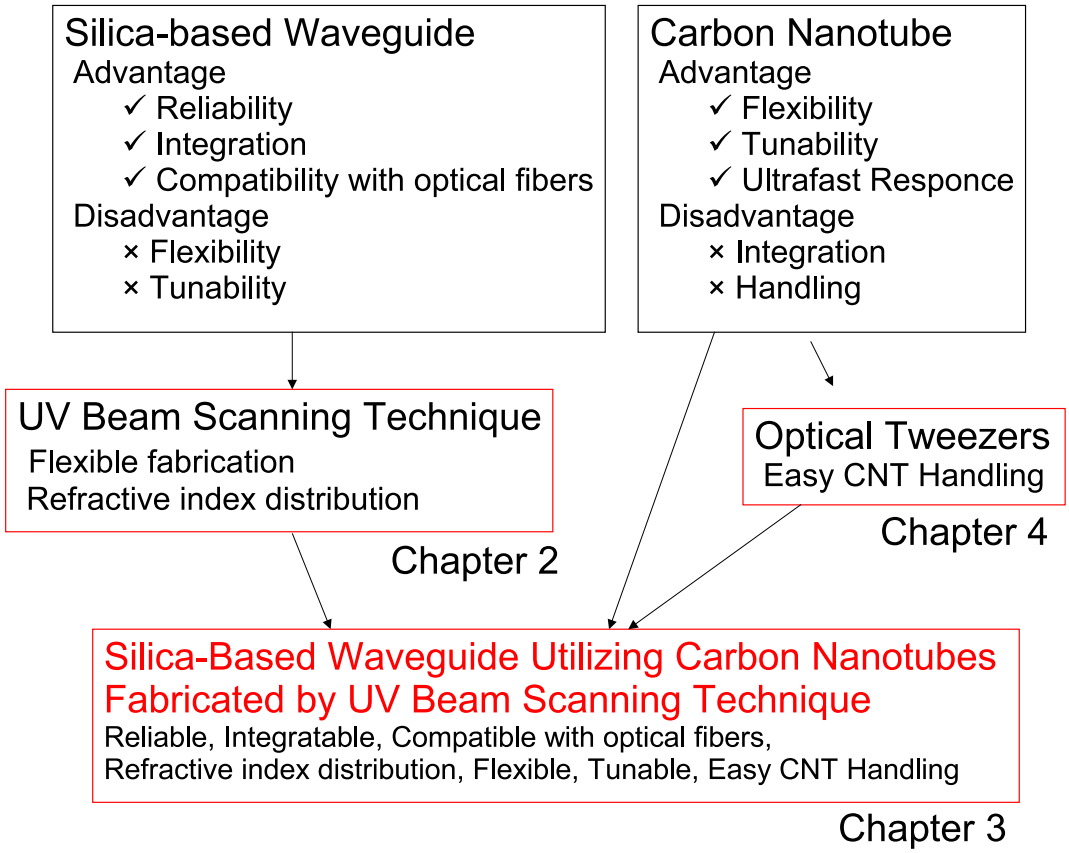

Fig. 1.2: Topics of this thesis

bulky and not suitable for integration. The handling of the CNTs can be considered as an additional problem since the CNTs have small footprint and difficulty in being dispersed in common solvents. Thus, a novel method for easy and efficient handling of CNTs is required. In order to overcome the drawbacks, CNT-based planar waveguide-type devices will be required for further highly functional and integrated devices. In this work, we study the combination of silica-based waveguides and CNTs in this thesis to achieve the additional advantages from the two as well as to overcome the drawbacks. We propose and demonstrate a technique to handle CNTs which is based on optical tweezers. Topics of this thesis are illustrated in Fig. 1.2.

Our device concept investigated in this thesis is depicted in Fig. 1.3. By UV beam scanning technique, we fabricate functional planar waveguide circuits, such as directional couplers, Mach-Zehnder interferometers. UV beam scanning technique make

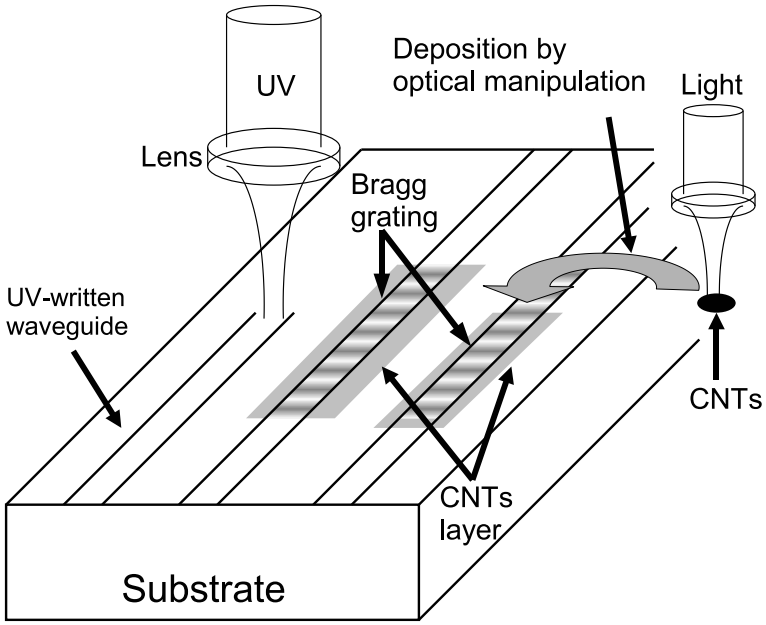

Fig. 1.3: Device concept investigated in this thesis

easy to integrate Bragg grating based devices and planar waveguide circuits. One of our objectives is to fabricate optically tunable Bragg gratings based devices by using interaction with CNTs in planar waveguide strucuture. This device is realized by both advantages of UV-written waveguides and CNTs. Another objective is deposition of CNTs with optical tweezers onto top surface of planar waveguides to realize CNT based planar waveguide type devices. Optical tweezers allow us to fabricate CNT based optical devices cost effectively. In this thesis, we investigate on these three topics, UV-written waveguides, CNT based optical devices and optical tweezer for CNT manipulation, and also study their combination.

1.3 Overview

This thesis is structured as follows.

In chapter 2, we study the fabrication of functional silica-based waveguide devices by UV beam scanning. Comparison between two silica-based waveguide fabrication techniques, conventionally used deposition and etching techniques and UV beam

scanning technique, is explained. The cross sectional refractive indices of waveguides fabricated by UV beam scanning are measured as fundamental data for further complex device realization. Sampled Bragg grating-based devices are examined for integrated multi-wavelength OADMs. We introduce multiple phase shift technique to decrease the device size and densify the channel spacing of sampled grating.

Chapter 3 focuses planar waveguide-type CNT devices. First, fundamental properties of CNTs are reviewed. We propose and demonstrate CNT-based planar waveguide-type devices. For the first step of planar waveguide-type CNT device, we fabricate a saturable absorber in planar structure. The saturable absorber is used to modelock a fiber ring laser to achieve femtosecond pulses. All-optical switching with nonlinear optical loop mirror configuration is also demonstrated using planar waveguide-type CNT-based nonlinear device.

In chapter 4, we propose, for the first time, to use optical tweezers to handle the CNTs in fabricating optical devices. We deposit CNTs employing the optical tweezers onto only a desired core region of fiber end facet . We also propose to use optical reflectometry to monitor the CNT deposition to control the CNT layer condition precisely. We present the formation of sphere-shaped super structures of the CNTs only by optical tweezers without any chemical functionalization.

Finally, summary of this thesis is added in chapter 5.

Chapter 2 : Fabrication of Silica-Based Optical Channel Waveguides by UV Beam Scanning

2.1 Introduction to This Chapter

In this chapter, we study UV beam scanning technique and fabrication of functional devices by the technique. Section 2.2 introduces a comparison between conventional process and UV beam scanning technique. Principle of UV beam scanning technique, photosensitivity in Ge-doped silica-glass, is also introduced.

For further sophistication of the devices which will be fabricated by UV beam scanning, more fundamental data is necessary. In section 2.3, we present structure characterization of silica-based optical channel waveguides fabricated by UV beam scanning technique.

Section 2.4 regards with fabrication of Bragg grating based devices by using only UV beam scanning technique. We fabricate optical channel waveguides containing sampled Bragg gratings, and introduce multiple phase shift technique to densify the channel spacing of sampled Bragg gratings.

2.2 Fabrication Techniques of Silica-Based Optical Channel Waveguides

2.2.1 Conventional Fabrication Technique

Generally, the optical waveguides have the structure where high refractive index material is surrounded by low refractive index material. A light is guided by total reflection at the boundary of the two materials. High and low refractive index regions are called “core” and “cladding”, respectively. Functional devices have been realized by

diversified waveguide patterns. The two materials are based on silica-glass in silica-based waveguides. Doping of germanium (Ge) increases a refractive index of silica-glass, and doping fluorine (F) or boron (B) into silica-glass decreases the refractive index of the glass. These techniques are used in silica-based optical fiber fabrication. By these techniques, we control the cross sectional refractive index profiles. In general, we just dope Ge into the core region to form the refractive index difference of core and cladding.

Typically, silica-based planar waveguides are fabricated on silicon (Si) substrates. Figure 2.1 shows the conventional fabrication process of silica-based planar waveguides [25].

The process is as follows.

1. Depositing under-cladding layer and core layer by depositing glass particles with flame hydrolysis deposition (FHD) method

2. Pattering desired waveguide design by lithography followed by reactive ion etching (RIE) to get ridge waveguides

3. Covering core ridge with over-cladding by FHD method

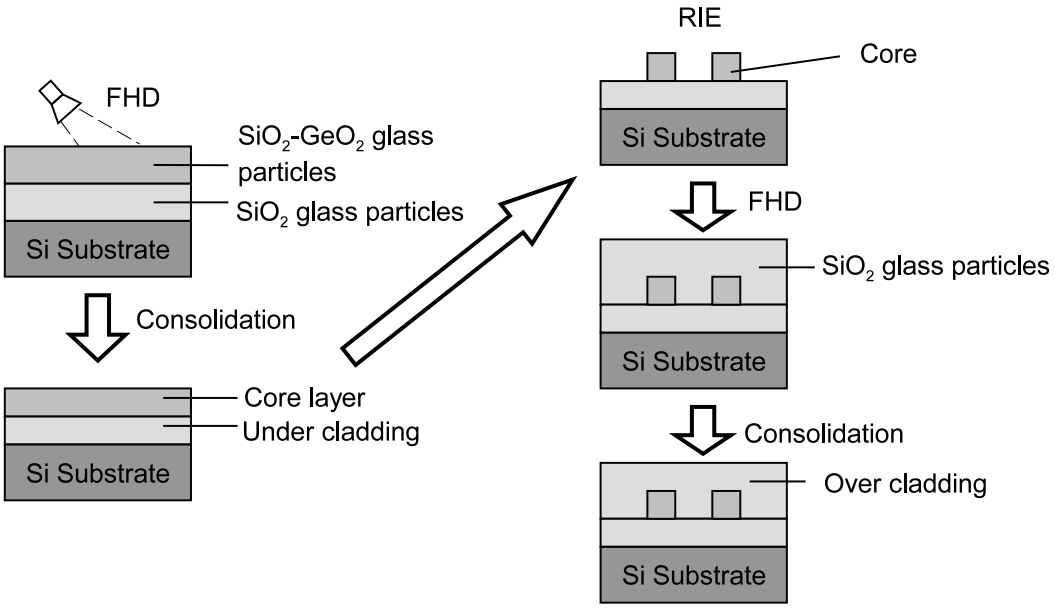

Fig. 2.1: Conventional fabrication process of silica-based waveguides [25]

As explained above, silica-based waveguides are fabricated by silicon large scale integration (LSI) technology, and the technology is well matured during the long history. However, the technique is complicated and high cost. On the other hand, optical devices require the lower cost and flexibility. To meet with these requirements, one of the option is to fabricate silica-based waveguides by UV beam. The next subsection introduces principle of UV beam induced silica-based waveguide fabrication, photosensitivity.

2.2.2 Photosensitivity

The phenomenon which is denoted "photosensitivity" in this thesis represents UV induced refractive index change in silica-glass. This phenomenon strongly occurs in Ge-doped silica-glass, the material of core in silica-based optical fibers and waveguides. Fiber Bragg gratings (FBGs) and long period fiber gratings (LPFGs) are the main applications. In general, the refractive index of UV irradiated glass increases. K.O. Hill first discovered the photosensitivity when he observed a formation of a Bragg grating by injecting 488nm Ar-ion laser into optical fiber [6]. After then, scientists found that the refractive index change was caused by two photon absorption, and the Ge-doped silica-glass had an absorption band in UV light region [26]. The initial attainable refractive index change was in the order of 10^{-5}. This value is not large enough to fabricate waveguides or the complicated fiber Bragg gratings. Subsequently, high pressure hydrogen loading was discovered to enhance the photosensitivity drastically [27], and the refractive index increase reached up to the order of 10^{-2} [13]. This value is as high as that of the refractive index difference between the cores and the claddings of optical fibers. The refractive index change depends on conditions of glasses, such as glass-type, Ge concentration, the wavelength of the UV source, whether continuous wave laser or pulsed laser, power density, whether hydrogen loaded or not, etc [28].

We review the photosensitivity in Ge-doped silica-glass, hydrogen loading technique and the mechanism of the photosensitivity in followings. Photosensitivity had been recognized to be inherent in UV light, at the wavelength of 240∼250nm, and in highly Ge-doped core of silica fibers. It was found that the light at the other wavelength could

induce the refractive index change, and optical fibers having other dopants also possesed photosensitivity. Photosensitivity was revealed even in the glass without OH groups [13]. However, there is no any other atoms which enhance photosensitivity better than Ge. Therefore, optical absorption around 240nm wavelength range is very important. 240nm wavelength is corresponds to the photon energy of 5eV.

The origin of photosensitivity is defects in Ge-doped silica glass. In Fig. 2.2, the defects in Ge doped silica glass are depicted. The defect which contributes to photosensitivity is called neutral oxygen mono vacancy (NOMV), a direct bonding between two Ge atoms.

During high temperature process, GeO_2 is decomposed to GeO molecule (Ge^{2+}) because GeO molecule is stable at high temperature. The GeO molecules tend to form "Ge - Ge" bondings (NOMV) and contribute to the index change. Therefore, doping concentration of GeO_2 directly determine sensitivity to the index change. NOMV forms an absorption band which has the center wavelength around 240nm. When UV light which has the wavelength in the absorption band is irradiated, the bonds break, and glass matrix changes as shown in Fig.2.3 . Subsequently, absorption peak changes, and the refractive index changes due to Kramers-Kronig relationship. Another origin of refractive index change is strain change in the glass. Glass matrix change results in

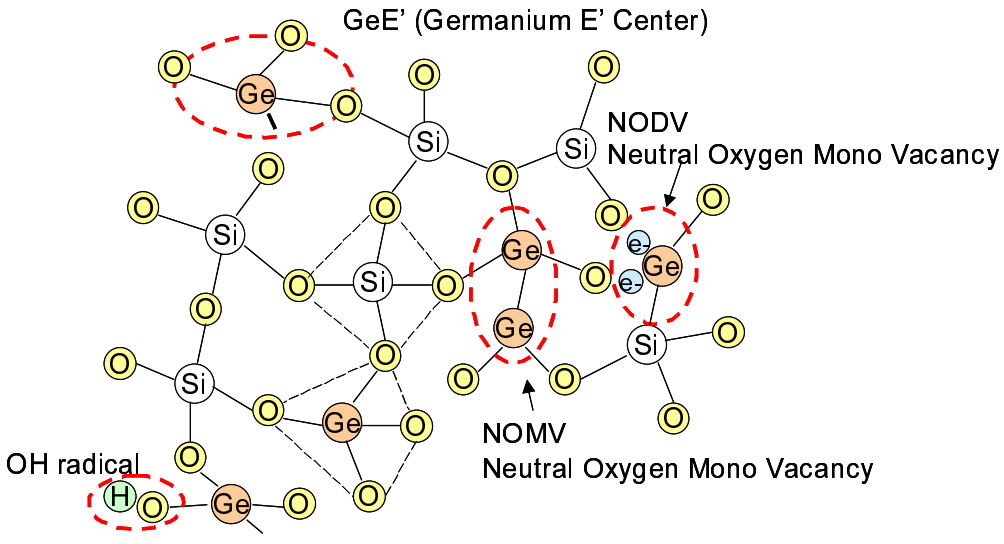

Fig. 2.2: Various defects in Ge-doped silica glass

strain distribution change in the glass. The strain change causes refractive index change because of elasto-optic effect.

Since the photosensitivity was discovered, the studies about photosensitivity focused on not only the mechanism but also how to enhance photosensitivity. Typical Ge-doping concentration of 3% into silica-fiber core produces refractive index change of 10^{-5} order. High concentration of Ge allows to get refractive index change of 10^{-3} order [13]. However, enhancing photosensitivity of standard single mode fiber (SMF) is necessary to keep compatible with optical communication systems. Enhancement of photosensitivity in standard SMF was revealed by high pressure hydrogen loading technique, and refractive index change exceeded 10^{-2} [27].

High pressure hydrogen loading technique enhances photosensitivity by diffusion of hydrogen into silica-glasses with keeping silica-glasses in hydrogen atmosphere at 20 $\sim$ 75°C in 20 $\sim$ 750 atm (typically around 150atm) for 2 $\sim$ 3 weeks. Hydrogen can be diffused over 95% of saturation concentration even by treating hydrogen loading at room temperature. Formation of OH-groups by hydrogen diffusion enhances the photosensitivity because they absorb the electrons which emerge in the reaction which was shown in Fig. 2.3. The reaction is not perfectly one-way. In a certain probability, opposite reaction occurs and the refractive index change is suppressed. Absorption of the electrons by OH-group prevents the opposite reaction. In Fig. 2.4, absorption spectrum change due to hydrogen loading is shown [29]. The longer hydrogen loading treating time, the stronger absorption band around 240nm wavelength range was formed. The spectrum change indicates the enhancement of photosensitivity.

One of the benefits of high pressure hydrogen loading technique is that the technique

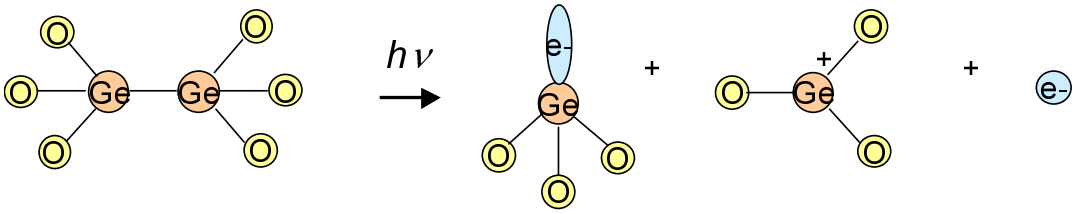

Fig. 2.3: Reaction when refractive index changes

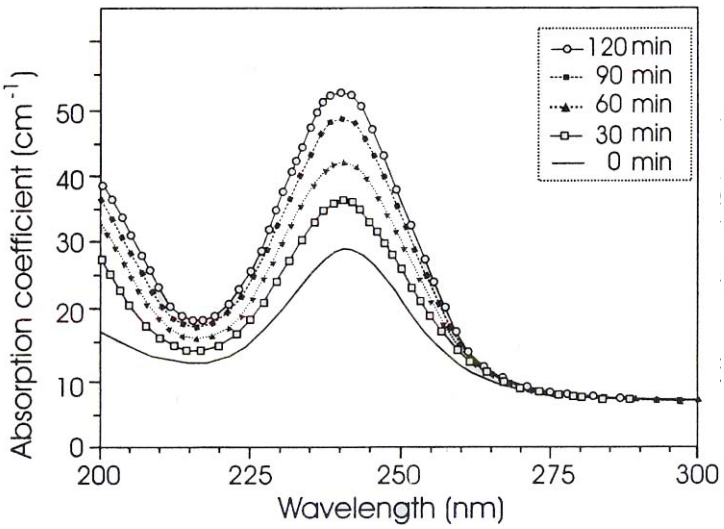

Fig. 2.4: Absorption spectrum change depend on hydrogenation time [29]

is applicable to various kinds of silica-glass, such as less concentration of Ge or lack of Ge silica-glass. Another benefit is excess loss due to the technique is negligible because hydrogen atoms in the area without UV light irradiation will out-diffuse. The wavelength band which loss increase due to the technique are 1.39μm band and 1.41μm band due to absorption of Si-OH bonding and Ge-OH bonding, respectively. The loss at the wavelength bands can be avoided by using deuterium instead of hydrogen, because absorption band shift to longer wavelength band, around 1.7μm [13].

Mechanism of refractive index change starts from light absorption is often explained mainly by Kramers-Kronig model and compression model. Typical Kramers-Kronig model is that the refractive index change is calculated by absorption spectrum change. During the UV-induced refractive index change process, NOMV absorbs the UV light, releases an electron, atom arrangement changes, and finally the absorption spectrum changes. Refractive index and absorption spectrum change have the relationships which is expressed as next formula.

$$\Delta n(\lambda) = \frac{1}{2\pi^2} P \int_0^\infty \frac{\Delta\alpha_{\text{eff}}(\lambda')}{1 - \left(\frac{\lambda'}{\lambda}\right)^2} \mathrm{d}\lambda \tag{2.1}$$

where P is main value of integration, λ is the wavelength, $\Delta\alpha_{\text{eff}}$ the difference of

effective optical absorption coefficient. $\Delta\alpha_{\text{eff}}$ is expressed in terms of the length of a sample(L) as

$$\Delta\alpha_{\text{eff}}(\lambda) = \left(\frac{1}{L}\right)\int_0^L \Delta\alpha(\lambda, z)\text{dz} \tag{2.2}$$

Since the irradiated UV light is attenuated by absorption, we have to consider effective optical absorption coefficient.

However, only by the model UV induced refractive index change cannot be explained clearly. The value of the refractive index change which was calculated from this model had big difference with the value of experimental result [30]. To explain the difference, usually compaction model is used additional to Kramers-Kronig model. The atom rearrangement due to UV light absorption results in physical compaction of the glass. There is a report which represents observation of glass compaction with a microscope in the preform of optical fibers [31]. The compaction is typically originated from the atom rearrangement shown in Fig. 2.4. The bondings from Ge atom are three dimensional in left hand side in Fig. 2.4. On the other hand, in right hand side the bondings from Ge atom are all in the same plane, two dimension. This change of dimension denotes the glass is compressed from three dimensional structure to two dimensional structure. Hence, UV irradiation increase refractive index of Ge-doped silica-glass.

In this thesis, we utilize the refractive index increase to fabricate optical channel waveguides. We form the refractive index difference between core and cladding by UV-induced refractive index increase. Next subsection explains fabrication process of silica-based optical channel waveguides by UV beam scanning.

2.2.3 Fabrication Technique by UV Beam Scanning

The fabrication process of UV-written waveguides is illustrated in Fig. 2.5. Under-cladding layer, Ge-doped layer, over-cladding layer are deposited on the Si substrate by single FHD process and consolidated. We scan focused UV beam spot in desired waveguide pattern, and only the refractive index of Ge-doped layer increases. The refractive index increase forms the refractive index contrast between core and cladding. Through the process, we get desired waveguide pattern. Typically, the silica-based

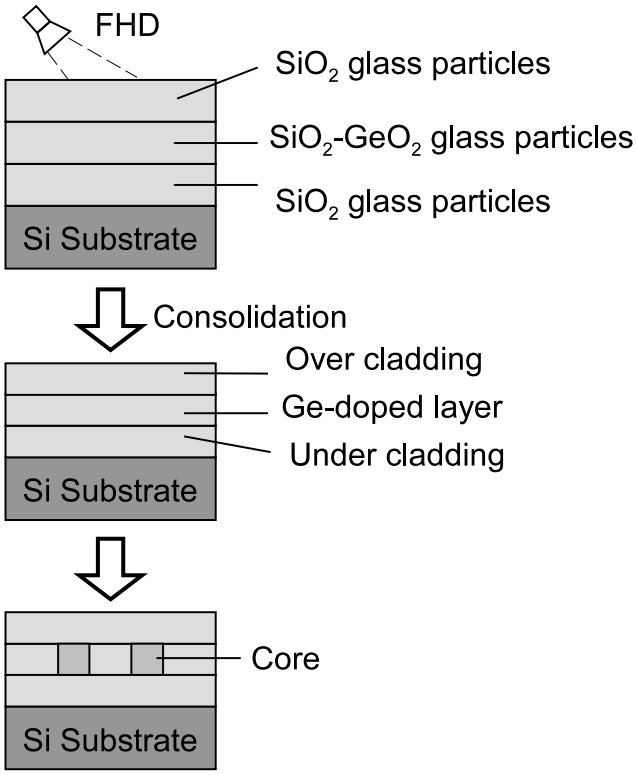

Fig. 2.5: Fabrication process of silica-based optical channel waveguides by UV beam scanning

optical waveguides have the refractive index difference (delta, Δ) as high as 0.2 $\sim$ 0.3 %. However, the refractive index increase only originated from Ge-doping is not enough for the light confinement. It is difficult to achieve the refractive index difference of $3 \times 10^{-3} \sim 5 \times 10^{-3}$ by UV-induced refractive index increase. Therefore, we treat the samples hydrogen loading in advance. We keep our samples in 130atm hydrogen atmosphere for 1 week. The hydrogen loaded samples are kept in -70°C to prevent out diffusion of hydrogen atoms because diffused hydrogen atoms are not stable in the glass at room temperature.

After waveguide fabrication by UV beam scanning, we anneal the sample in high temperature. The annealing process have two meanings.

- Removing the bondings which are unstable at room temperature
- Out-diffusing the hydrogen atoms which did not react during UV irradiation

The out-diffusion of hydrogen atoms has two meanings.

1. As well know from history of optical fiber fabrication, OH-group in silica-glass form 1.4 μm absorption band and propagation loss drastically increase within the band. Out-diffusion of hydrogen reduces the 1.4μm band propagation loss. However, annealing process cannot out-diffuse all the OH-groups and weak absorption occurs in the wavelength band. The absorption loss can be avoided by not using 1.4μm band or using deuterium instead of hydrogen for loading process. Deuterium loading enhances photosensitivity, and absorption band is formed at 1.7μm band, not in 1.4 μm band. However, in this thesis, we use hydrogen instead of deuterium because of the high cost of deuterium.

2. Hydrogen or deuterium atoms are unstable in silica-glass, therefore samples are reserved in low temperature. At room temperature the atoms will out-diffuse and the waveguide characteristics will change. The time-dependent change is prevented by annealing-induced hydrogen out-diffusion process before the device use.

Distribution of refractive index pattern along a waveguide can be easily formed by changing UV beam irradiated power. Bragg gratings are based on refractive index perturbation along a waveguide, and they are useful to realize functional devices with high integration and low loss. Functional devices based on Bragg gratings will be further examined in section 2.4. Subsection 2.2.4 introduces experimental setup for waveguide fabrication by UV beam scanning.

2.2.4 Experimental Setup for Waveguide Fabrication by UV Beam Scanning

The experimental setup for waveguides fabrication by UV beam scanning is shown in Fig. 2.6. We use a frequency doubled Argon (Ar) ion laser for UV light source. An Ar-ion laser is a gas laser which utilizes excited states of Ar^+-ion, and posses several lasing wavelengths in visible region. In this thesis, we select fundamental mode of 488nm wavelength, and generate UV light of frequency doubled 244nm continuous wave (CW)

light by inserting a second harmonics generation (SHG) crystal into the laser cavity. The SHG crystal is inserted into laser cavity, and purged by nitrogen to be blocked from humidity in air. The output light has beam diameter of 0.6∼0.8mm, ∼100mW output power and 100:1 horizontal polarization.

To start the setup, we first insert a SHG crystal into laser cavity and align the laser cavity. Front and back mirrors, the SHG crystal position and angle are controlled to maximize the UV light output power. Since effective cavity changes by thermal effect due to a lasing light in the laser cavity, it takes about an hour for warm-up to get stable laser output. Typical maximum output power is about 100mW. If the cavity is considerably misaligned, we first align the 488nm fundamental mode laser cavity to maximize 488nm laser output, and align the 244nm cavity through the procedure explained above. During the two cavities alignment, laser optics must be changed for each wavelength.

As explained above, the laser cavity needs alignment for every use, and optical path changes every time. Therefore, we have to align the optical path every experiment. First, angles of mirrors are adjusted without a lens so that an angle of incident to a

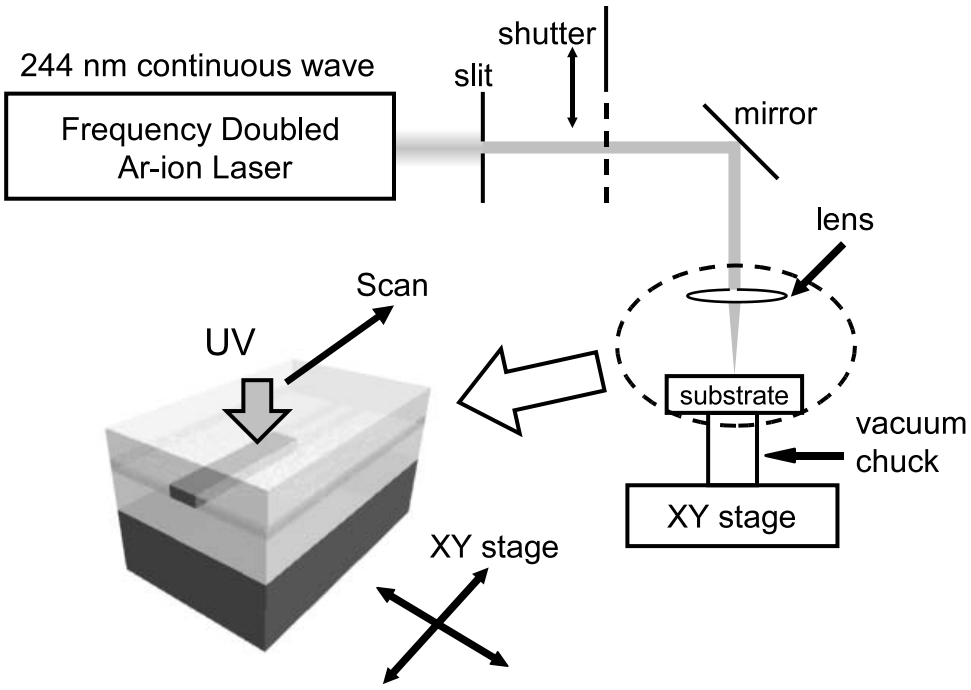

Fig. 2.6: Experimental setup for waveguide fabrication

sample is roughly perpendicular. After a lens is inserted, we adjust optical path to go through center of the lens. The mirrors are aligned so that only a beam spot size changes without shifting the incident position by moving the lens. When the path is shifted from the center, the incident position at the sample moves by moving the lens up and down.

By the procedure mentioned above, the mirrors and lens are roughly adjusted, and we perform succeeding precise alignments. The opposite direction light is used for final precise alignment. We adjust the mirror angles so that the reflected light propagates through the same optical path in opposite direction.

Then, we insert a slit to eliminate fringes of the laser beam. The output laser beam profile has fringes because of phase match condition with SHG crystal. However, narrow slit causes strong diffraction. Therefore, the width of the slit is adjusted with observing the beam profile just before the lens. A shutter is inserted to select UV beam irradiate position. In case that lens position is in proper position, we can observe the red luminescence, and adjust the lens to get the strongest luminescence.

UV beam spot is aligned with the procedure mentioned above. To fabricate a waveguide, we scan the focused spot desired waveguide pattern by moving a XY translation stage where a sample is fixed. After the use, we take out the SHG crystal and stop the nitrogen purging. Therefore, we need optical alignment for every use of the laser.

Experimental setup for waveguide fabrication by UV beam scanning is constructed and aligned as explained above. From next section, we investigate silica-based optical channel waveguides fabricated by UV beam scanning.

2.3 Structural Characterization of Silica-Based Optical Channel Waveguides

2.3.1 Introduction

Structures and properties of silica-based waveguides fabricated by the conventional process which were explained in 2.2.1 have been well studied in their long history. On the other hand, those of waveguides fabricated by UV beam irradiation are not fully investigated. One of the reason is the fabrication technique does not have long history compared with the conventional technique. The another reason is the waveguides do not have the steep refractive index distribution, and the refractive index profiles make an analytic study difficult. Since Mizrahi et al. first reported the fabrication of a silica-based optical channel waveguide by UV beam irradiation [13], all most all of the reports were focused on the fabrication of functional devices, such as optical power splitter [17, 18], directional coupler [18], Bragg grating [21]. There are few reports which have studied about the waveguide characteristics [32–34]. However, the reports are indirect study such as constructing a model from microscope image or using scanning near-field optical microscope (SNOM) to measure asperity of waveguide top. For further highly functional and integrated devices, we investigate on the structural characterization of the waveguides. In this section, we present structures of silica-based waveguides fabricated by UV beam scanning measured by refracted near field method.

2.3.2 Refracted Near Field Method

The basic physical characteristics of optical waveguides are given by cross-sectional refractive index distributions. From the distributions, we can derive all optical characteristics, such as mode profiles, dispersions, etc. However, characteristics of planar optical waveguides cannot be calculated analytically in spite of some certain waveguide profiles. Therefore, we simulate the waveguide properties by numerical analysis, such as finite element method, beam propagation method. Cross sectional refractive index profiles provide fundamental datas for the numerical analysis. The refracted near

field method is the most advanced technique to measure refractive index profiles of optical fibers [35] and optical planar waveguides. Since a reflection from Si substrate affects the measurement accuracy, simple refracted near field method cannot be used to silica-on-silicon planar waveguides. The experimental setup of refracted near field method for silica-on-silicon waveguides is modified from that of optical fibers as shown in Fig. 2.7.

Basic principle of refracted near field method is Snell's law. A laser is focused on the sample, and the intensity of the rerefracted light is measured to calculate refractive index. We place the sample vertically and irradiate the focused laser at 656.5nm onto

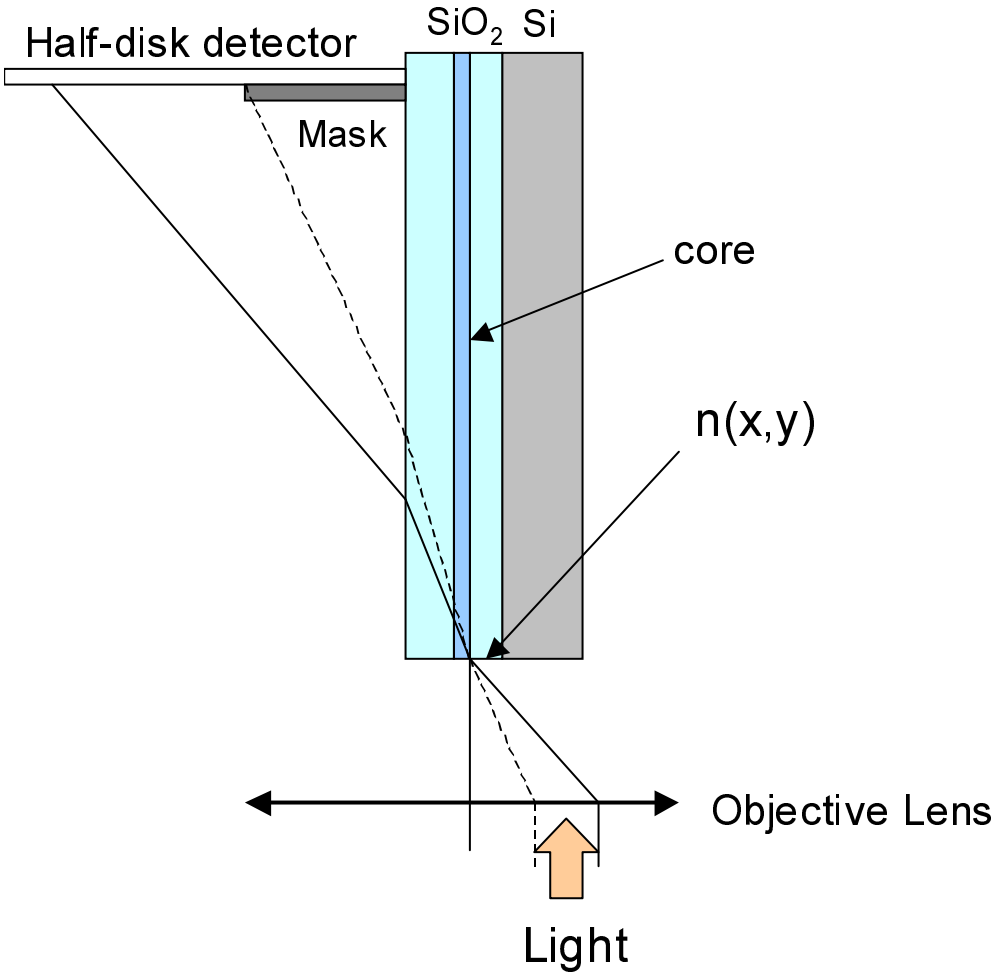

Fig. 2.7: Experimental setup of refracted near field method [36]

an end facet by an immersion objective lens. The sample cell contains index matching oil to prevent reflection from various boundaries. It is necessary that the end facet is perpendicularly cleaved and refractive index profile does not change along the waveguide for about 1mm from the end facet. Three quarters of parallel beam were blocked to prevent any light reflected from silicon substrate. For each (x, y) position, the detector signal correspond to refracted light intensity $I(x, y)$ is measured. From the $I(x, y)$ datas, refractive index profile $n(x, y)$ is calculated.

2.3.3 Experimental Results and Discussion

First, we fabricated channel waveguides by UV beam scanning in various scanning speeds, 1000, 500, 250, 100, 90, 80 ,70, 60, 50 ,40 , 30, 20, 10 μm/s. The waveguide fabrication setup was just same as explained in subsection 2.2.4, Fig.2.6. We used UV beam at 244nm from a frequency doubled Ar-ion laser which has the optical power of 70mW after the slit. The beam was focused down to around 5μm at the sample. The substrates had a silica-on-silicon three-layer structure which was deposited by the FHD method. The thickness of the under-cladding layer, the Ge-doped layer and the over-cladding layer were 15, 6, 30μm, respectively. The refractive index difference between Ge-doped layer and cladding layers was 0.75%. To enhance the photosensitivity, the substrates had been loaded with hydrogen at 130 atm for 1 week. After UV scanning, the substrates were annealed at 80°C for 24 hours to stabilize the UV-induced refractive index change. We measured cross sectional refractive index distribution with the refracted near field method.

Figures 2.8, 2.9 and 2.10 show the examples of cross sectional refractive index profiles of the waveguides measured at 656.5nm. The refractive index distribution of the waveguide fabricated at 30μm/s was found to be the most square contours. In Fig.2.11, the maximum refractive index increases of each waveguides are shown. The maximum refractive index increases was saturated around 0.01 at scanning speeds slower than 100μm/s. Figures 2.12 and 2.13 show the horizontal refractive index distributions at the mid-plane of Ge-doped layers and vertical refractive index distributions at the center of

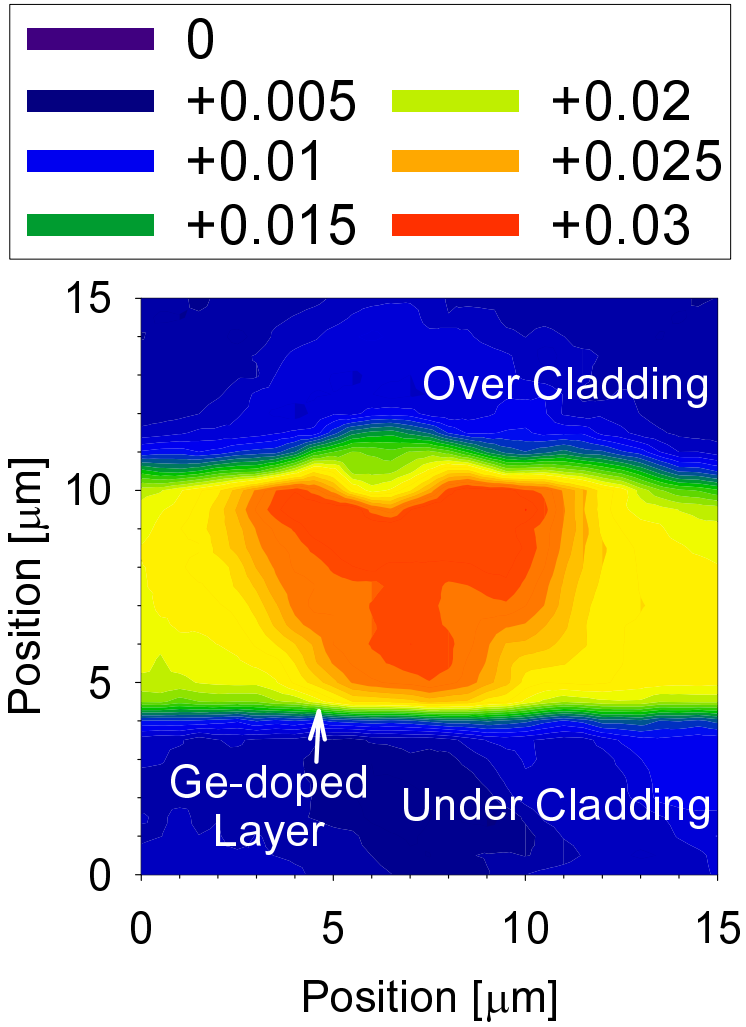

Fig. 2.8: Cross sectional refractive index distribution of the waveguide fabricated at the scanning speed of 10μm/s

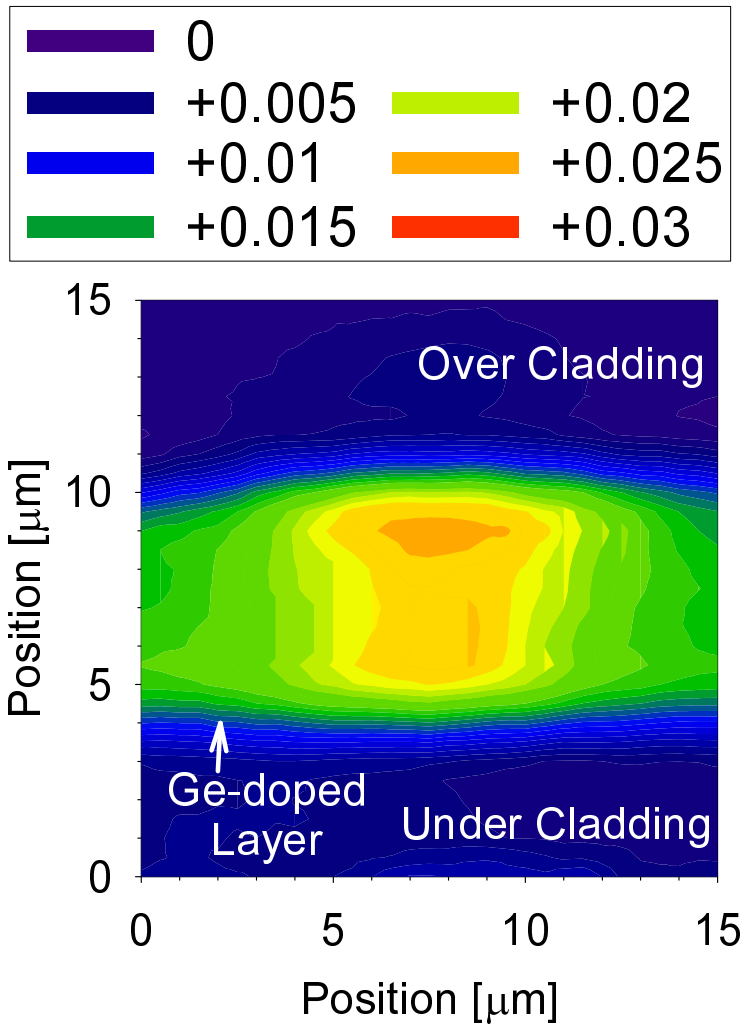

Fig. 2.9: Cross sectional refractive index distribution of the waveguide fabricated at the scanning speed of 30μm/s

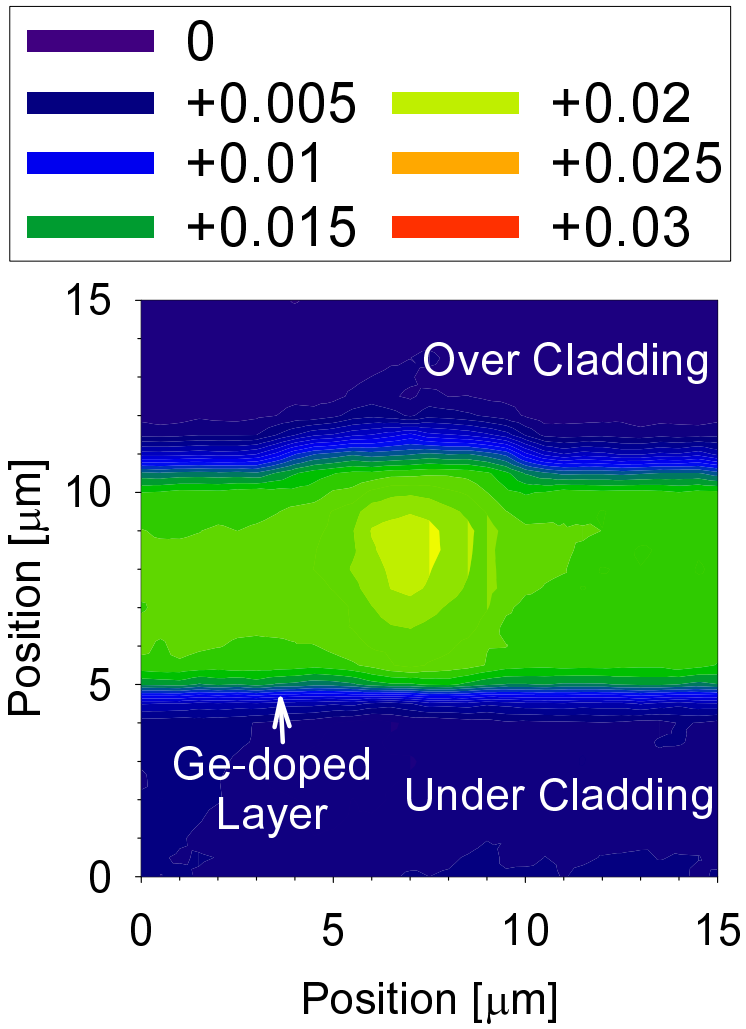

Fig. 2.10: Cross sectional refractive index distribution of the waveguide fabricated at the scanning speed of 1000μm/s

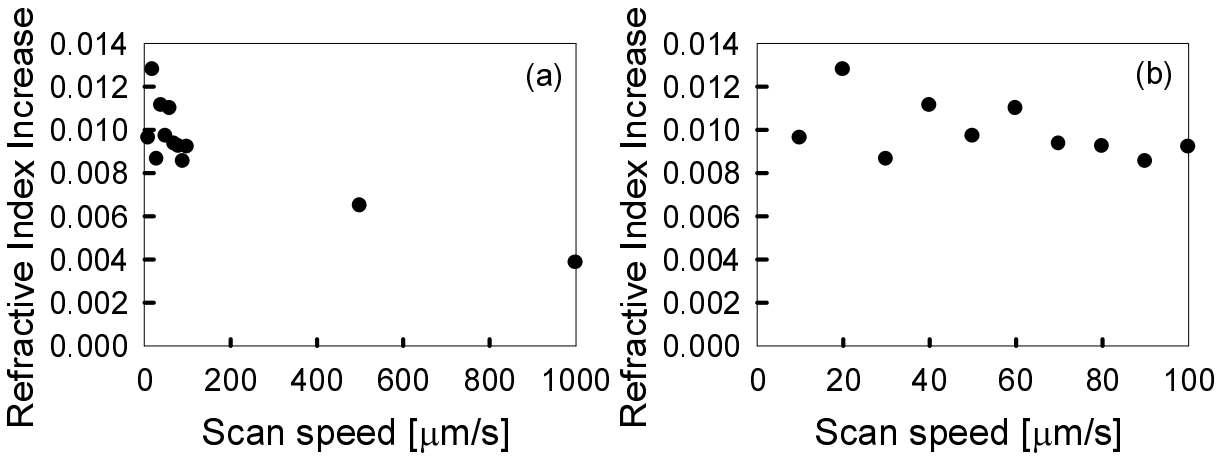

Fig. 2.11: Maximum refractive index increase (a) Whole Range (b) Under 100μm/s

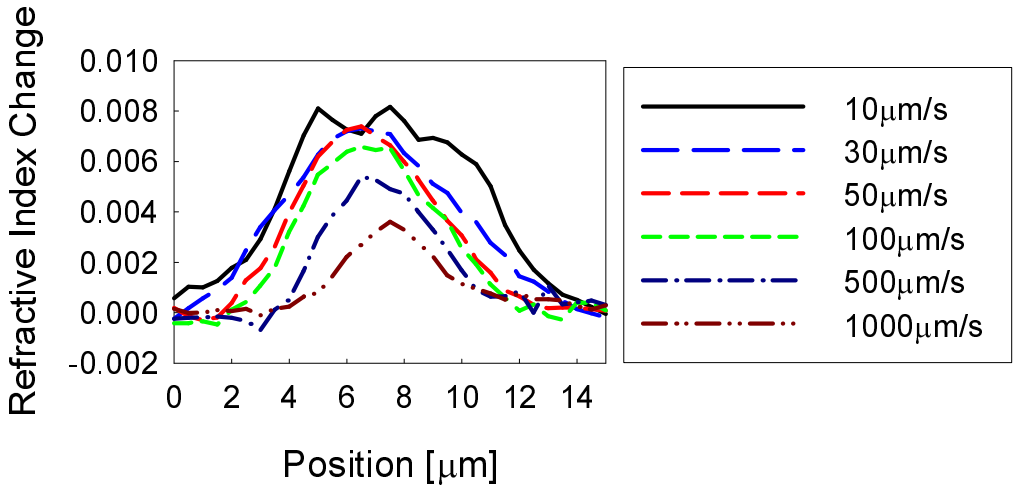

Fig. 2.12: Horizontal refractive index distribution at mid-plane of Ge-doped layer

the waveguides, respectively. The refractive index distributions had the Gaussian profiles in the horizontal direction, and the refractive index distributions were almost uniform in the vertical direction. The channel width actually became wider as the scanning speed became slower (Fig.2.14). We defined the waveguide width as the horizontal full width of 1/e maximum at the mid-plane of the Ge-doped layer. With slow scanning speed, the saturation of refractive index increase occured at the center of the UV beam spot, whereas it did not occur at the other area. Thus, by changing the scanning speed, we can control effective channel width. The controllability indicates that there is an

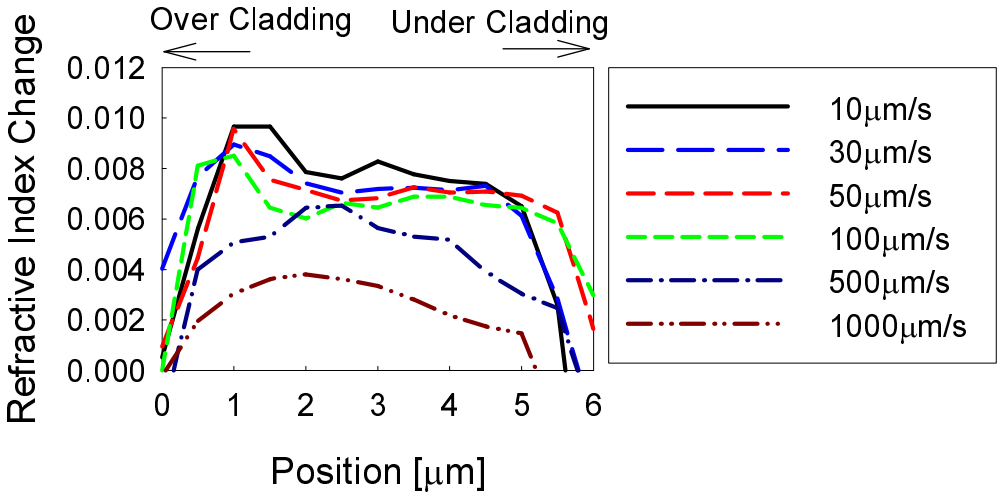

Fig. 2.13: Vertical refractive index distribution at center of the waveguide.

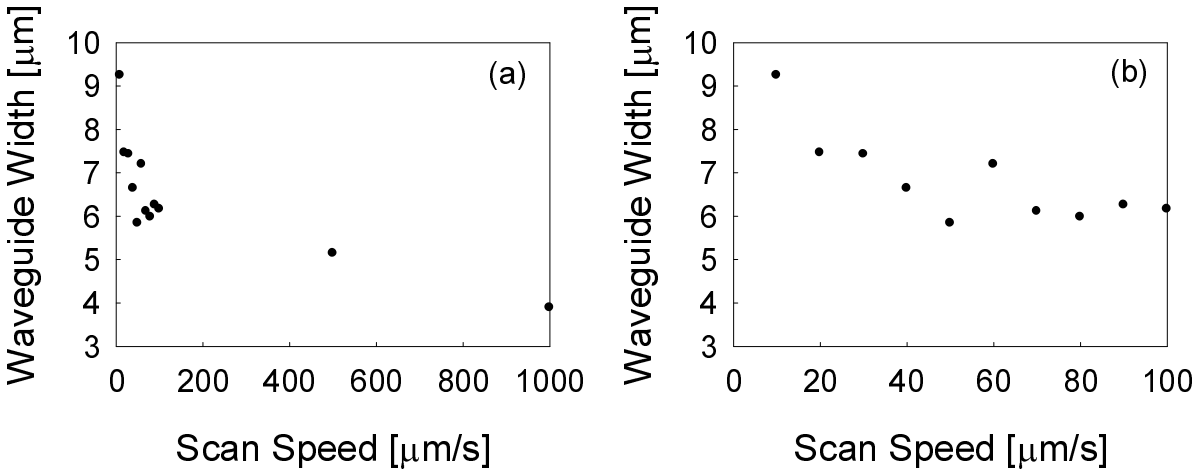

Fig. 2.14: Waveguide width (a) Whole Range (b) Under 100μm/s

optimum scanning speed for minimizing coupling loss between the waveguide and SMF. On the other hand, the waveguides fabricated by slow scanning speed could be affected by deviation of experimental conditions, such as vibration and fluctuation of UV beam power. Therefore, there is an optimum scanning speed for minimizing propagation loss. Propagation loss and coupling loss can be optimized by changing the scanning speed. This is an advantage of this waveguide fabrication technique.

2.4 Fabrication of Optical Channel Waveguides Containing Sampled Gratings

2.4.1 Introduction

Since writing Bragg grating into silica-based optical fiber was first demonstrated by K.O. Hill [6], FBGs have been intensively studied for OADMs, dispersion compensators, optical sensor heads, etc. There are several types of Bragg gratings, uniform Bragg gratings, phase shifted Bragg gratings, chirped Bragg gratings, sampled Bragg gratings, etc [7]. Writing Bragg gratings into waveguides are promising technique to realize functional and integrated devices. Bragg gratings are periodic refractive index perturbations along the optical waveguide, and the structure can be written by UV beam irradiation. Thus, Bragg gratings and UV beam scanning technique well match with each other.

Sampled Bragg gratings are suitable for WDM systems because we can handle multiple wavelength simultaneously with a single device. Sampled gratings are reflection type filters which have comb-like reflection spectrums. Applications are multiwavelength filters (multiwavelength OADMs and interleavers) [37, 38], multiwavelength dispersion compensators [39–41], filters for light sources, etc. Integration of sampled gratings with other functional component decreases the number of required devices in the optical communication systems. To handle the many signals with a single sampled grating, we need the sampled grating which has a wide bandwidth and dense channel spacing. However, widening the bandwidth and densification of the channel spacing is difficult in some aspects, especially in planar waveguide structure. For example, longer device size is necessary for sampled grating to densify its channel spacing. Since the device length of planar waveguides directly correspond to device cost, elongating the sampled grating should be avoided for planar waveguide devices. In this section, we investigate on the fabrication of silica-based waveguides containing sampled gratings by UV beam scanning. We first fabricate the simple sampled gratings in subsection 2.4.4, and we introduced multiple phase shift technique [42] in subsection 2.4.5 to solve the device

elongation problem.

2.4.2 Principles of Bragg gratings and Phase Mask Method

The periodic refractive index perturbation along the optical waveguides work as band-reflection filter, and they are called "Bragg gratings". Bragg gratings, for instance, which reflect the 1.5μm light have about 500nm period of the refractive index in silica-based waveguides.

In Fig.2.15, schematics of Bragg gratings is shown. When a light propagates through a Bragg grating, the light is slightly reflected at every position where the refractive index changes. The reflected light grows if the lights which are reflected at the different positions have the phase difference which is multiple of 2π. In case the phase difference is 2π, the Bragg grating is especially called "fundamental Bragg gratings". Reflected light intensity depends on modulation depth of the refractive index and the length of the Bragg grating. The reflection wavelength (λ_B) corresponds to the period of the refractive index perturbation. The wavelength and the period are called "Bragg wavelength" and "Bragg period", respectively. The reflection which have induced by fundamental Bragg gratings is called "fundamental reflection", and the wavelength of the light is called "fundamental Bragg wavelength". In case that phase difference is 4π, the wavelength is called "second order Bragg wavelength". Generally, we use the fundamental Bragg wavelength. Bragg gratings written in optical fibers are called "Fiber Bragg Gratings (FBGs)". The lights which are not at the Bragg wavelength propagate through the Bragg grating because the phase matching conditions are not satisfied.

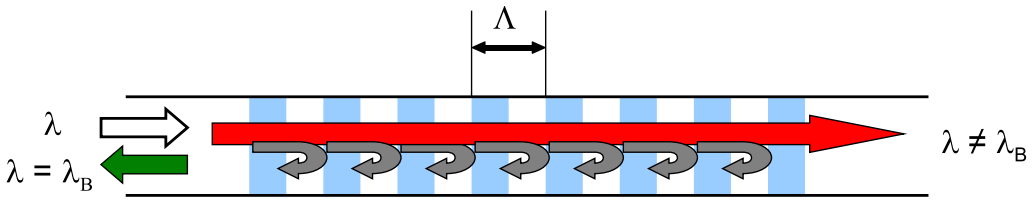

Fig. 2.15: Schematics of Bragg gratings

Bragg wavelength λ_B is expressed as

$$\lambda_B = 2n_{eff}\Lambda \tag{2.3}$$

where n_{eff} is an effective refractive index of a waveguide and Λ is a period of refractive index distribution. For a single mode waveguide, only a single wavelength match with the Eq. 2.3. However, a birefringence generate two different reflection peaks for transverse electric (TE) and transverse magnetic (TM) mode. The silica-on-silicon waveguides usually have birefringence due to the strain from the silicon substrate. Therefore, the Bragg wavelengths of TE and TM modes are different in the waveguides.

Figure 2.16 shows the schematics of considering Bragg gratings in wave number domain. Black and white circles represent core-modes and cladding-modes, respectively. Shadowed region express radiation modes, and the radiation modes have the continuous propagation constant(β). The lights which have negative propagation constants propagate in "$-z$" direction. If the propagation constant (β_1) of the light change into β_2 by $2\pi/\Lambda$ perturbation due to the periodic refractive index distribution and β_2 is the propagation constant which the light can propagate in the waveguide, the light will be reflected by the Bragg grating. β_2 is expressed as

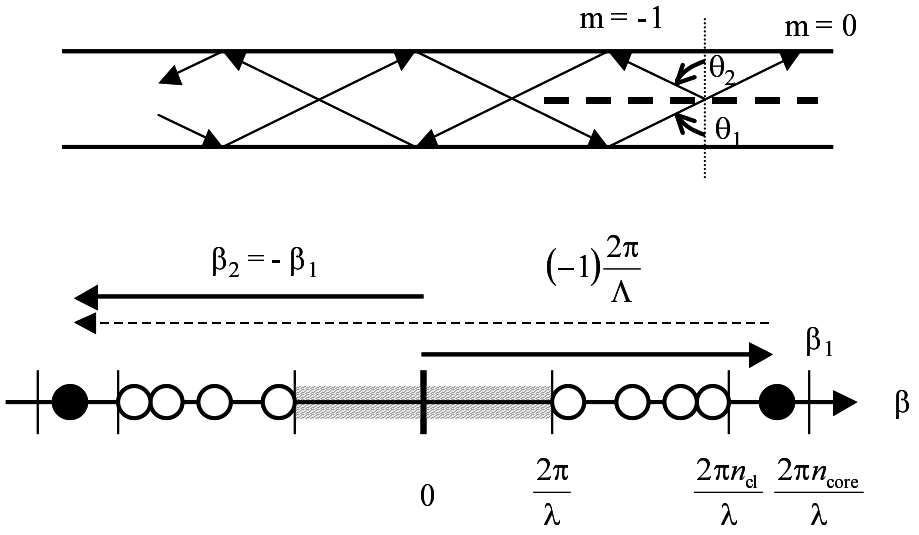

Fig. 2.16: Schematics of wave number domain

$$\beta_2 = \beta_1 + m\frac{2\pi}{\Lambda} \tag{2.4}$$

For single mode waveguides, β_2 which satisfy the Eq. 2.4 is only $\beta_2 = -\beta_1$. $m = -1$ represents the fundamental Bragg reflection. To increase the reflectivity of a Bragg grating, the modulation depth of refractive index and the elongation of the Bragg grating is necessary. Narrowing the reflection band of the Bragg grating can be realized by elongation of the length.

There is non-uniform Bragg grating which is called "apodized Bragg grating". The apodized Bragg gratings have the distribution of the modulation depth of the refractive index along the waveguides. The apodized Bragg gratings are used to suppress the sidelobes which strongly emerge in uniform Bragg gratings [7, 43–45]. In general, we use apodization profiles of commonly used profiles, such as Gaussian, Sinc, etc.

Here, the fabrication methods of Bragg gratings are explained. K.O. Hill et al. [6] first fabricated Bragg gratings by using counter propagating beams. By this method, the wavelengths of writing and reflection lights are identical, and there is no controlability to fabricate Bragg gratings which have various Bragg wavelengths. For example, the period of refractive index distribution of Bragg gratings is around 500nm for 1550nm reflection band in silica-based waveguides. The sub-micrometer order periodicity cannot be written by focused UV beam because of the diffraction limit. Then, a technique of transversely irradiating interference pattern in suitable angled two UV beams was invented. There are two major methods to form interference patterns, the two beam interference method [46] and the phase mask method. Emmerson et al. proposed and demonstrated the simultaneous fabrication of silica-based optical channel waveguides and Bragg gratings by two beam interference method [21]. This method needs precise control of two beam interference angle and UV irradiation position. In this work, we employ phase mask method because of its simplicity.

A schematic of phase mask method is illustrated in Fig. 2.17. Phase mask is a quarts substrate which has periodic grooves (period d and groove depth d_g). The UV beam is separated into +1st and -1st diffraction beams after the phase mask. The two diffracted

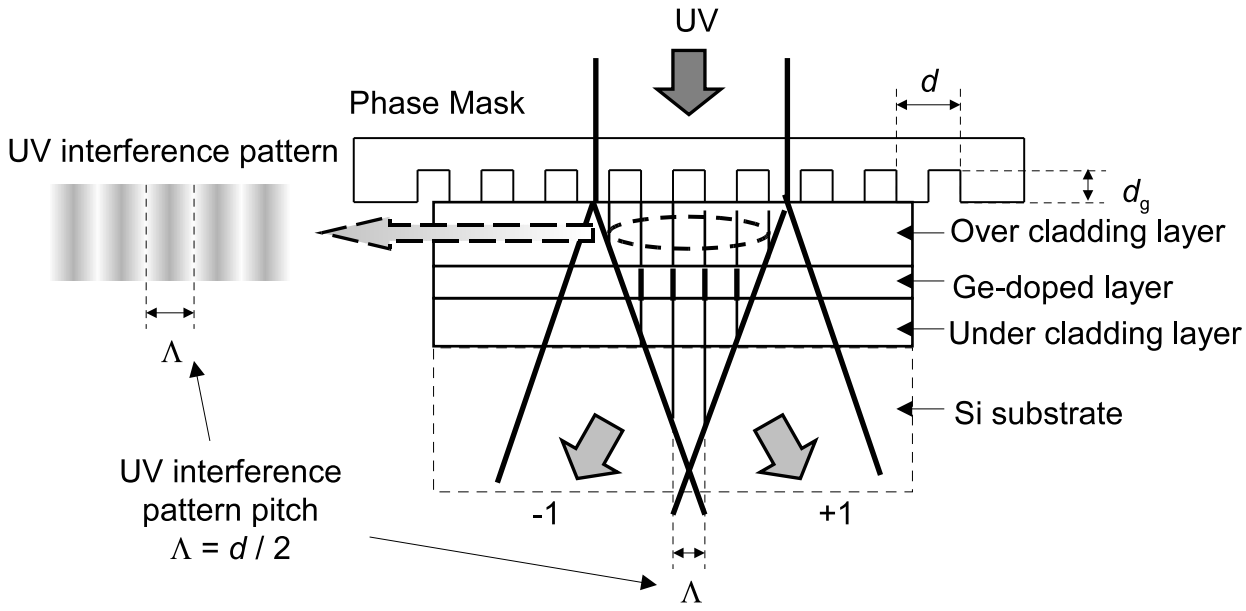

Fig. 2.17: Schematics of phase mask method

beams interfere with each other and form a interference pattern which has a period of $d/2$. The periodic UV beam power distribution which correspond to the interference pattern is written into the silica-based waveguides. The depth of the grooves (d_g) is designed to suppress the 0th order diffraction beam. The advantages of the method are its simplicity and reproducibility.

In this subsection, we introduced basics of Bragg gratings. Next subsection 2.4.3 explains our main topic of this section, sampled Bragg gratings and multiple phase shift technique.

2.4.3 Sampled Gratings and Multiple Phase Shift Technique

Here, we introduce the basic principle of sampled gratings. Sampled gratings consists of several separated individual Bragg gratings as shown in Fig. 2.18. Sampled gratings have a multiwavelength reflection spectrum originated from the Fabry-Perot interference. The width of the spectrum envelope is inversely proportional to the length of individual Bragg gratings (L_g), and the channel spacing (Δf) is inversely proportional to the sampling period(L_s). Therefore, to achieve dense channel spacing and wide-bandwidth, writing

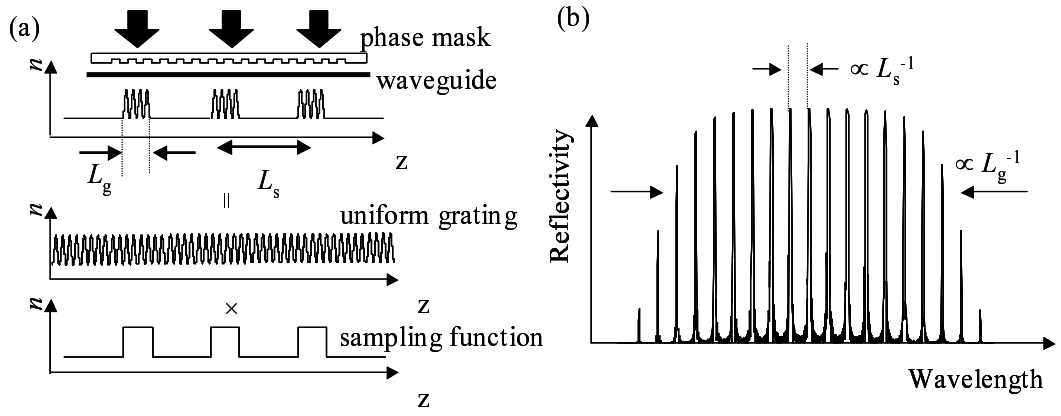

Fig. 2.18: Schematics of Sampled gratings
(a) Schematics of refractive index distribution of sampled grating and fabrication method
(b) Relation between reflection spectrum and sampled grating parameters

short individual grating with long sampling period is necessary. However, the total length becomes long for high reflectivity because the individual gratings are short. Multiple phase shift (MPS) technique can solve the problem [42].

The channel spacing (Δf) is expressed in terms of the speed of light in vacuum (c) and effective refractive index (n_{eff}) as

$$\Delta f = \frac{c}{2n_{\text{eff}}L_{\text{s}}} \tag{2.5}$$

From this equation, sampling period becomes $2L_{\text{s}}$ to densify channel spacing to be $\Delta f/2$, and the total length needs twice length ($2L_{\text{total}}$) to maintain the reflectivity. In like manner, sampling period becomes $3L_{\text{s}}$ to densify channel spacing to be $\Delta f/3$, and the total length is $3L_{\text{total}}$.

By MPS technique, we can densify channel spacing without elongating sampling period. For example, we can halve the channel spacing to $\Delta f/2$ by applying phase shift between individual Bragg gratings as $0, \pi, 2\pi, 3\pi, \cdots$ or $0, \pi, 0, \pi, 0, \pi$. Triple densification can be realized by applying phase shift as $0, 2\pi/3, 4\pi/3, 6\pi/3, \cdots$ or $0, 2\pi/3, 4\pi/3, 0, \cdots$. In the two cases, the total length of sampled grating (L_{total}) is maintained. To densify channel spacing to be $\Delta f/m$, phase shift (ϕ_k) between kth and $(k+1)$th Bragg gratings

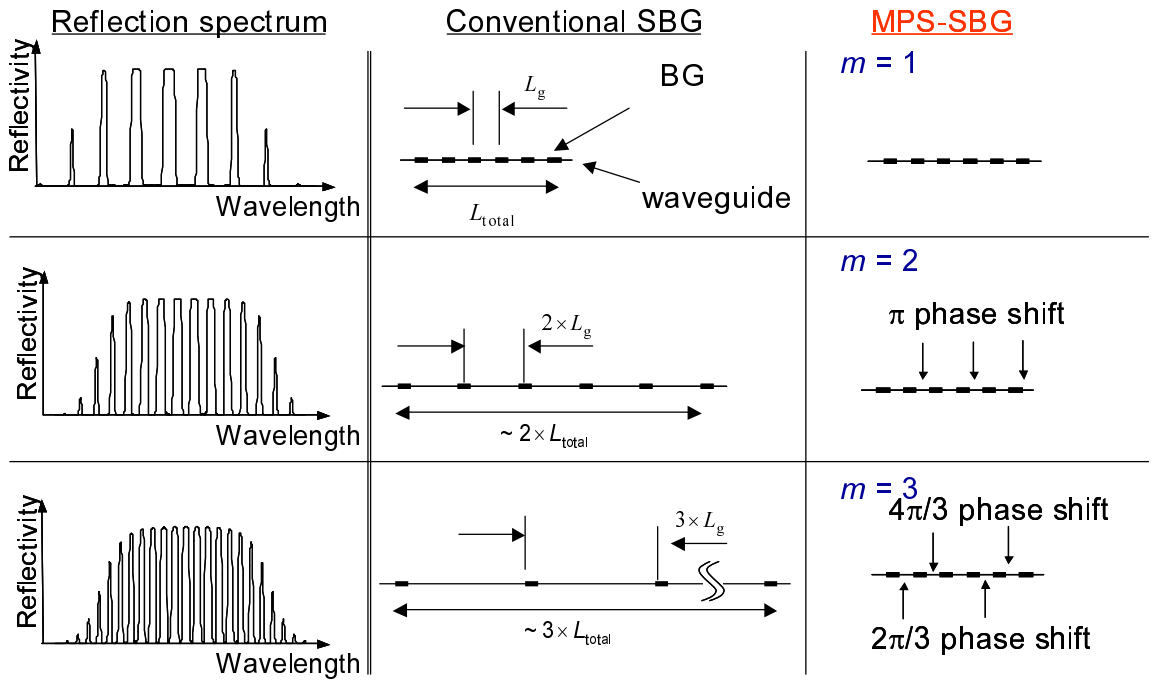

Fig. 2.19: Schematics of Multiple phase shift technique

is expressed as,

$$\phi_k = \frac{2\pi}{m}(k-1) \qquad [0 \leq k \leq N_{\mathrm{BG}}] \tag{2.6}$$

where N_{BG} expresses total number of Bragg gratings. By applying these phase shifts, channel spacing will be densified to be $1/m$.

In the next subsection 2.4.4, we represents the fabrication of sampled Bragg gratings by UV beam scanning.

2.4.4 Sampled Grating Fabrication

First of all, we prepared the silica-on-silicon substrates which had been treated hydrogen loading. The substrates had silica-on-silicon three-layer structures which were deposited by the FHD technique. The thickness of the under-cladding layer, the Ge-doped layer and the over-cladding layer were 15, 6, 30μm, respectively. The refractive index difference between Ge-doped layer and cladding layers was 0.75%. We treated the

substrates hydrogen loading at 130 atm for 1 week. The substrates were ready after the hydrogenation process.

We fabricated optical channel waveguides containing sampled gratings in two steps (Fig.2.20). First, we fabricated uniform channel waveguides by scanning the focused UV beam. Then, we exposed the UV beam through the phase mask to write sampled Bragg gratings.

Experimental setup was explained in section 2.2.4, Fig.2.6. After fabricating a uniform waveguide at the scanning speed of 100μm/s, we removed the lens to make the beam parallel, and fixed a phase mask which had 1068.52nm pitch just above the waveguides. The length of the individual Bragg gratings were controlled by a slit. We measured the waveguide transmission spectrum by butt-coupling SMFs with index matching oil to suppress Fresnel reflection.

Figure 2.21 shows the transmission spectrum of the 10mm-long waveguide containing sampled gratings whose individual gratings length is 300 and 500μm. The number of gratings was 10. Sampling period was 1mm which correspond to 100GHz channel spacing.

Sampled gratings which have the channel spacing of 100GHz(0.8nm) were successfully fabricated. The reflectivity was as high as 99%. Sampled Bragg gratings which have shorter length of individual Bragg gratings have the wider bandwidth of reflection envelope. Since the waveguides posses birefringence, whole the reflection spectra of TE and TM modes was shifted with each other. To achieve polarization independence,

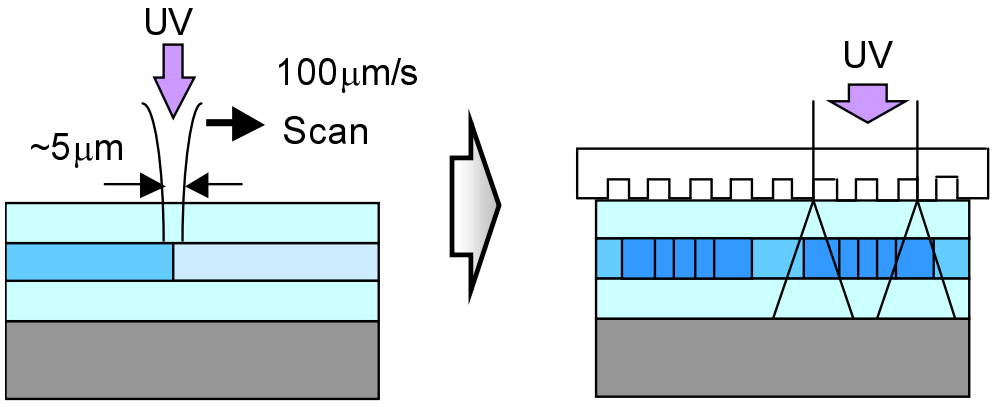

Fig. 2.20: Schematics of Sampled grating fabrication process

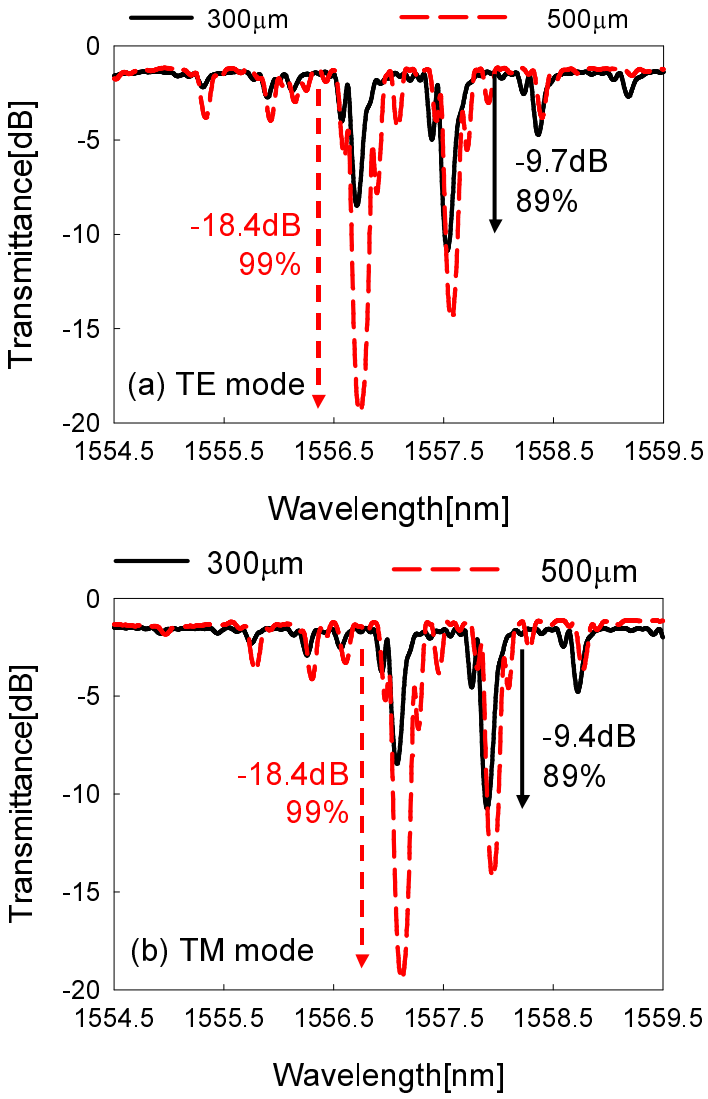

Fig. 2.21: Transmittance spectrum of waveguide containing sampled grating (a)TE mode (b)TM mode

we have to eliminate the birefringence. However, only by UV beam scanning technique, it is difficult to solve the problem. We usually make a groove beside the waveguides to protect the waveguides from the strain due to the Si substrate.

From Fig. 2.21, the number of channels seems to be small. However, from the reflection spectrum in Fig. 2.22 shows the more reflection channels which are hided by the high reflectivity channels in 2.21. Since there was a coupling loss between the waveguides and SMFs, we could not measure reflectivity. The reflection spectrums in Fig. 2.22

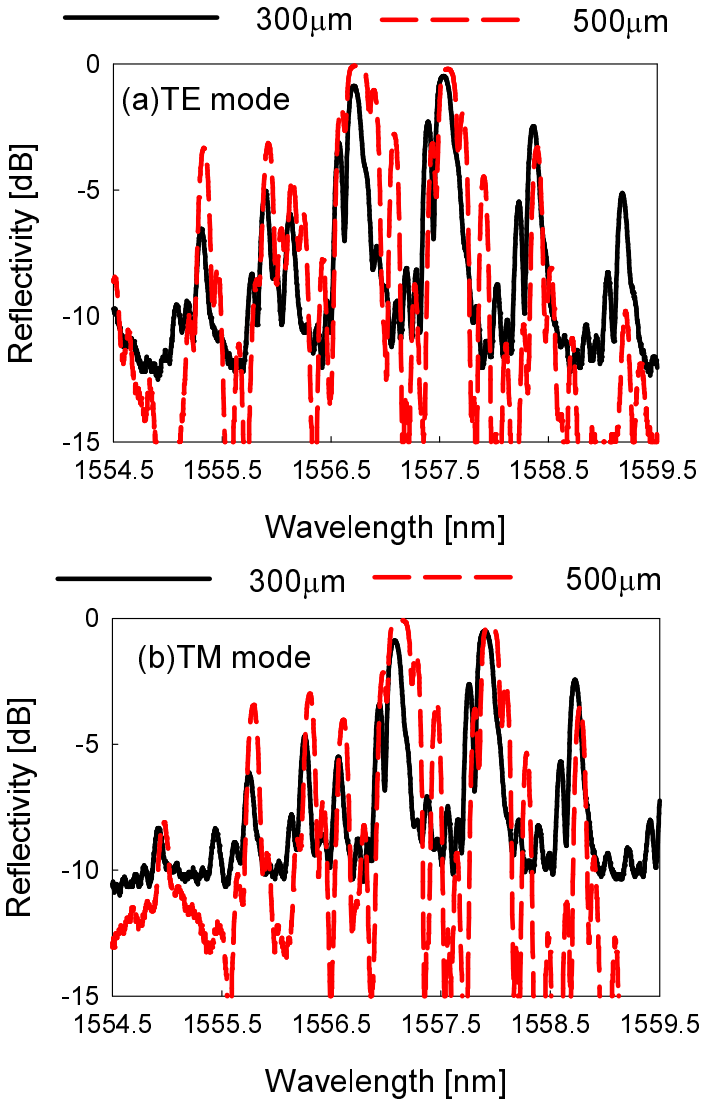

Fig. 2.22: Reflectivity spectrum of waveguide containing sampled grating
(a)TE mode (b)TM mode

are calculated from the transmission spectrum in Fig. 2.21. Although there is a large background reflection about -10 dB in Fig. 2.22, this does not represent actual reflection. Small deviation in the data of transmission spectrum causes large difference in reflection spectrum because we calculated reflectivity from transmittance. Therefore, only the reflection peaks have the meanings in Fig. 2.22. The large side peaks in every channels might be caused by the reflection of UV beam from Si substrate affected the Bragg gratings. We successfully fabricated the optical waveguides containing sampled grating

which have 100GHz channel spacing and 99% reflectivity. To enhance the channel density, we introduce MPS technique in the next section.

2.4.5 Fabrication of Sampled Grating with Multiple Phase Shifts

In this subsection, we examine the densification of channel spacing with MPS technique. There are several methods to induce the phase shift between the individual Bragg gratings, such as shifting the phase of Bragg gratings, UV beam irradiation, thermo-optic effect, opto-elastic effect. We used the simplest method to introduced the phase shifts, the UV beam induced refractive index change.

Figure 2.23 shows the waveguide design for double densified sampled grating ($m = 2$). We fabricated waveguides containing MPS introduced sampled gratings in two steps (Fig. 2.24). First, we fabricated a straight waveguide which has a periodic refractive index distribution like long period grating by periodic UV beam scanning speed. The period of twice of the sampling period of the sampled grating, in this case 2mm. Phase shift regions which have higher refractive index than other waveguide sections were preprocessed by slowing the scanning speed and located between the Bragg gratings every four Bragg gratings. The other waveguide sections were fabricated at the scanning speed of 100μm/s. Then, we exposed the UV beam through a phase mask. We fabricated sampled grating which has sampling period of 1mm correspond to 100GHz channel spacing with 1068.52nm pitch phase mask. Individual Bragg gratings were 300μm long, and the number of the gratings was 9. The lengths of phase shift sections were 500μm.

To determine the scanning speed of the phase shifting region, we estimated scanning speed dependence of effective refractive index increase by utilizing weak Bragg gratings.

The phase shift ($\Delta\phi$) induced by refractive index change is expressed as following equation.

$$\Delta\phi = \frac{2\pi}{\lambda}\Delta n_{\text{eff}}\Delta L \tag{2.7}$$

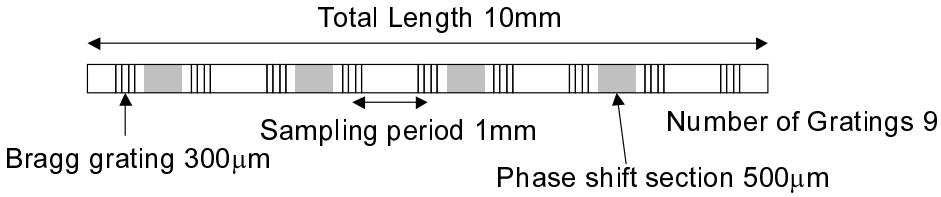

Fig. 2.23: Designed Waveguide containing MPS Introduced Sampled Grating

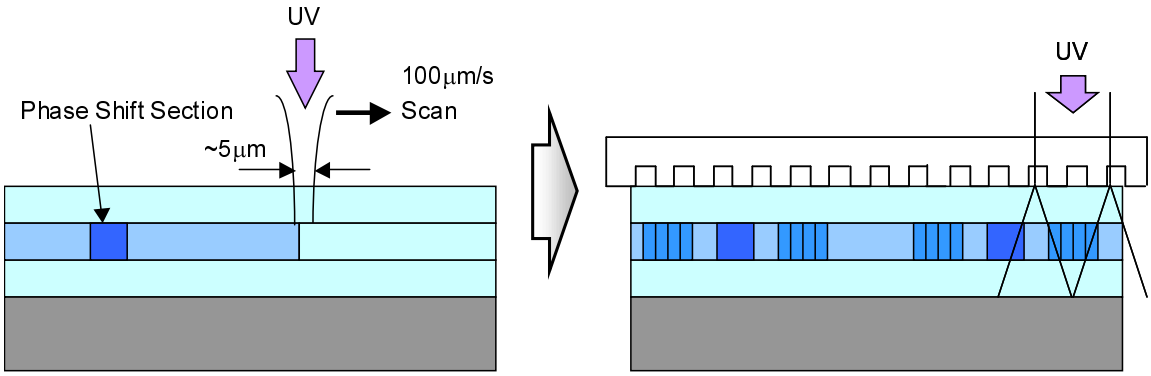

Fig. 2.24: Fabrication Process of Waveguide containing MPS Introduced Sampled Grating

where $\lambda, \Delta n_{\text{eff}}, \Delta L$ are the wavelength, the effective refractive index, the length of refractive index changed region, respectively.

As mentioned previously, the Bragg wavelength depends on effective refractive index (Eq. 2.3). Therefore, writing the weak and long Bragg grating into the waveguides, we can measure refractive index increase. We fabricated the weak and long Bragg gratings into the waveguides fabricated by scanning speed of 10, 20, 30, 40, 50, 60, 70, 80, 90, 100μm/s.

Figure 2.25 depicts the scanning speed dependence of effective refractive index increase regulated with 100μm/s value. ΔL is 500μm from design pattern in Fig. 2.23, and λ is 1.55 μm for communication wavelength. For a double densification, π phase shift is needed. Therefore, the required effective refractive index difference (Δn_{eff}) is 1.55×10^{-3} from Eq.2.7. From Fig. 2.25, 10μm/s is suitable for our design. The phase shift condition cannot perfectly match both in TE and TM mode because the refractive index increase has the polarization dependence.

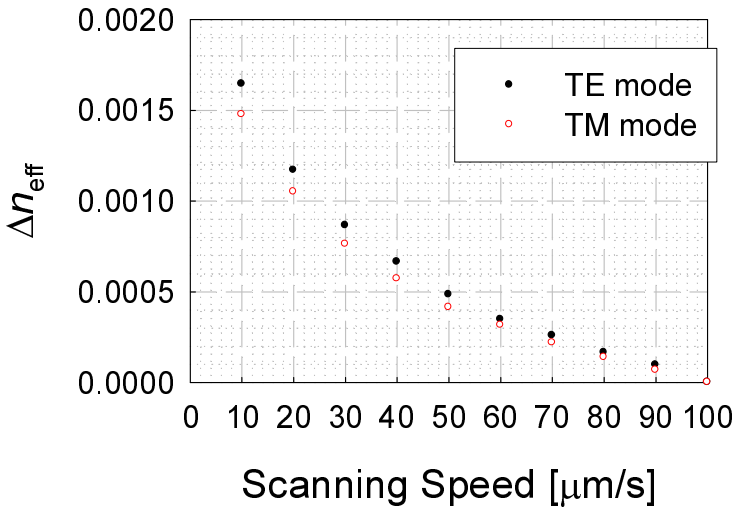

Fig. 2.25: Scanning speed dependence of effective refractive index increase regulated by the waveguide fabricated at the scanning speed of 100μm/s

Finally, we fabricated MPS introduced sampled gratings. Experimental setup has already explained in section 2.2.4 (Fig.2.6). We fabricated the waveguides with and without phase shift region. The phase shift sections were fabricated by 10μm/s scanning speed and uniform channel waveguide sections were fabricated by the 100μm/s scanning speed. After the waveguides fabrication, the lens was removed to make the beam parallel and phase mask was set just above the waveguides. The phase mask which has the 1068.52nm pitch was used. We set the length of individual Bragg gratings 300 μm by a slit.

Figure 2.26 shows the transmission spectrums of the 10mm-long waveguides containing sampled grating whose individual gratings length was 300 μm with and without phase shift region. The number of gratings was 9. Sampling period was 1mm which correspond to 100GHz channel spacing. We successfully densified the channel spacing of 100GHz to 50GHz by introducing MPS technique. Since it is difficult to observe small peaks in transmittance spectrum, we calculated the reflectivity spectrum from the transmittance data. The reflection spectrums in Fig. 2.27 are calculated from the transmission spectrum in Fig. 2.26. By introducing π phase shift between every two Bragg gratings, we successfully halved the 100GHz channel spacing to be 50GHz. However, we could

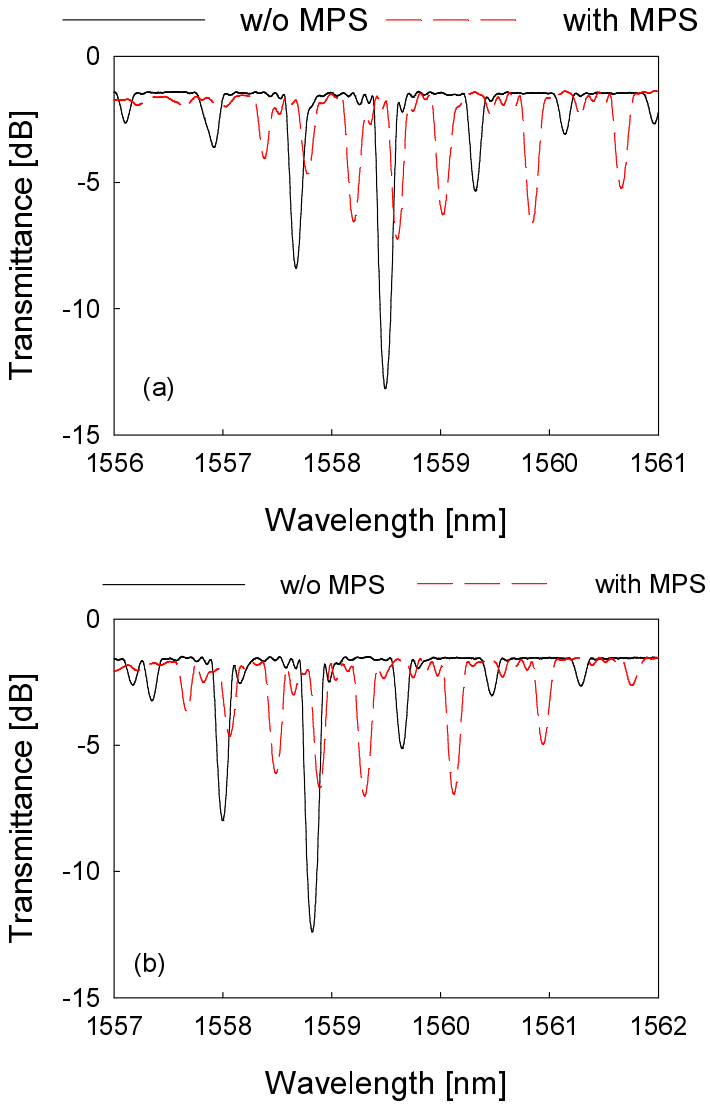

Fig. 2.26: Transmittance spectrum of waveguide containing MPS introduced sampled grating (a)TE mode (b)TM mode

not densify channel spacing at longer wavelength range. It is required to control more precise phase shift induction.

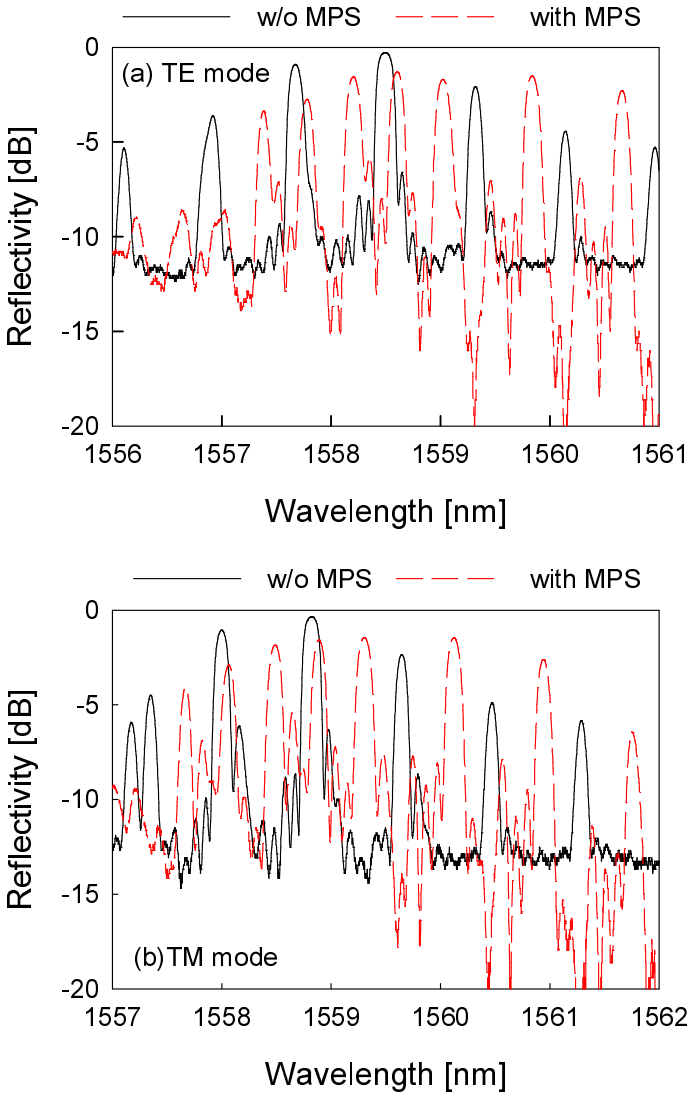

Fig. 2.27: Reflectivity spectrum of waveguide containing MPS introduced sampled grating (a)TE mode (b)TM mode

2.5 Summary of This Chapter

In this chapter, we investigated on the UV beam scanning technique and the functional device fabrication by the technique. Section 2.2 gave comparison between conventional process and UV beam scanning technique. We also presented the principle of the UV beam scanning technique, photosensitivity in Ge-doped silica-glass.

In section 2.3, we studied the structural characterization of silica-based optical channel waveguides fabricated by UV beam scanning technique. By using refracted near field method, we measured the cross sectional refractive index profiles of the waveguides which had been fabricated at the scanning speed of 1000, 500, 250, 100, 90, 80 ,70, 60, 50 ,40 , 30, 20, 10 μm/s. The maximum refractive index increase were saturated around 0.01 at the scanning speed of 100μm/s. The horizontal and vertical refractive index distributions were found to be Gaussian and uniform profile, respectively. We defined the waveguide width as the horizontal full width of 1/e maximum at the mid-plane of the Ge-doped layer. With slow scanning speed, saturation of refractive index increase occurs at the center of the UV beam spot, whereas it did not occur at the other area. Hence, we can control effective channel width with the scanning speed.

Section 2.4 focused on the fabrication of Bragg grating based devices by using only UV beam scanning technique. We fabricated optical channel waveguides containing sampled Bragg gratings, and introduced MPS technique to densify the channel spacing. First, we realized 10mm-long waveguide which contains sampled grating constructed by 9 Bragg gratings with 1mm sampling period, and achieved maximum reflectivity of 99%. By introducing MPS technique, 100GHz channel spacing was halved to be 50GHz.

Chapter 3 : Planar Waveguide Type Carbon Nanotube Photonic Devices

3.1 Introduction to This Chapter

Since CNTs were applied to a saturable absorber [22–24], applications of CNTs to photonics field have been intensively investigated. Up to now, the most of the studies about CNT photonic applications have focused on saturable absorption of CNTs. Saturable absorption, or optical induced transparency, of CNTs has been applied to passive mode-locker at several wavelength bands [23, 24, 47]. It has been reported that CNTs have strong third-order nonlinearity [48] and ultrafast recovery time shorter than 1ps [49–51]. These characteristics are attractive for future ultrafast photonic networks and can be used in ultrafast photonic devices, such as ultrafast all-optical switches and all-optical logic gates, etc.

CNTs were sprayed [23, 24] or directly synthesized onto quarts substrates and optical fiber ends [52], or embedded into polymer [53] to use as the photonic devices. However, these device structures are all bulky and not suitable for integration. If the waveguide-type CNT devices are realized, we can realize highly integrated CNT based devices. On the other hand, silica-based planar waveguides have small tunability, and CNTs are very attractive material to introduce tunability. In this chapter, we investigate a hybridization of silica-based planar waveguides and CNTs to combine their advantages and compensate their drawbacks with each other. We propose and demonstrate a planar waveguide-type CNT devices for future highly integrated CNT devices.

Section 3.2 introduces the basic properties of CNTs. The structure of CNTs, electronic properties, saturable absorption properties and optical nonlinearity of CNTs are explained.

Section 3.3 gives a first proposal and demonstration of a planar waveguide-type

CNT based device. By using UV-written silica-based waveguides, we fabricate planar waveguide-type saturable absorbers based on CNTs. We present a passively modelocked fiber ring laser which produce femtosecond pulses by using the saturable absorber.

In section 3.4, we investigate on all optical switching using a CNT loaded planar waveguide. We focus on all optical switching in nonlinear optical loop mirror configuration by using the waveguide as a optical nonlinear processing device.

3.2 Carbon Nanotubes

3.2.1 Basic Properties of Carbon Nanotubes

Figure 3.1 depicts the fourallotropes of carbon. Graphite and diamond have been well known allotropes of carbon. In 1985, the third allotrope of carbon, fullerene, was discovered by Kroto et al. [54], and carbon based nanomaterial research field emereged. CNTs are the forth new group of carbon materials which have nearly identical one-dimensional cylindrical structures, and their structures are assumed to be rolled sp^2-bonded graphene sheets. Graphene sheet is a sheet which carbon atoms are hexagonally bonding with each other. Since the discovery of CNTs by Iijima in 1991 [55], theoretical studies of CNTs have been intensively examined. The studies brought out the distinctive physical properties of CNTs, such as their electronic density of states (eDOS), and metallic and semiconducting distinction that depends only on their structure, chirality [56]. There are two types of CNTs, single walled nanotubes (SWNTs) have only single cylinder called, and multi walled nanotubes (MWNTs) have two or more cylinders. The CNTs which have optically interesting properties are SWNTs.

Experimental studies on CNTs became possible after the establishment of production methods in the late 1990s, such as laser-furnace [57], arc-discharge [58], and catalytic CVD methods with supported catalysts [59] and floated catalysts [60]. These methods are intended for use in the mass synthesis of CNTs in which the CNTs are obtained as soot adhered on the wall of the production chambers. Since the as-obtained soot contains amorphous carbons, multi-shelled graphites, fullerenes, and/or catalyst metal particles as

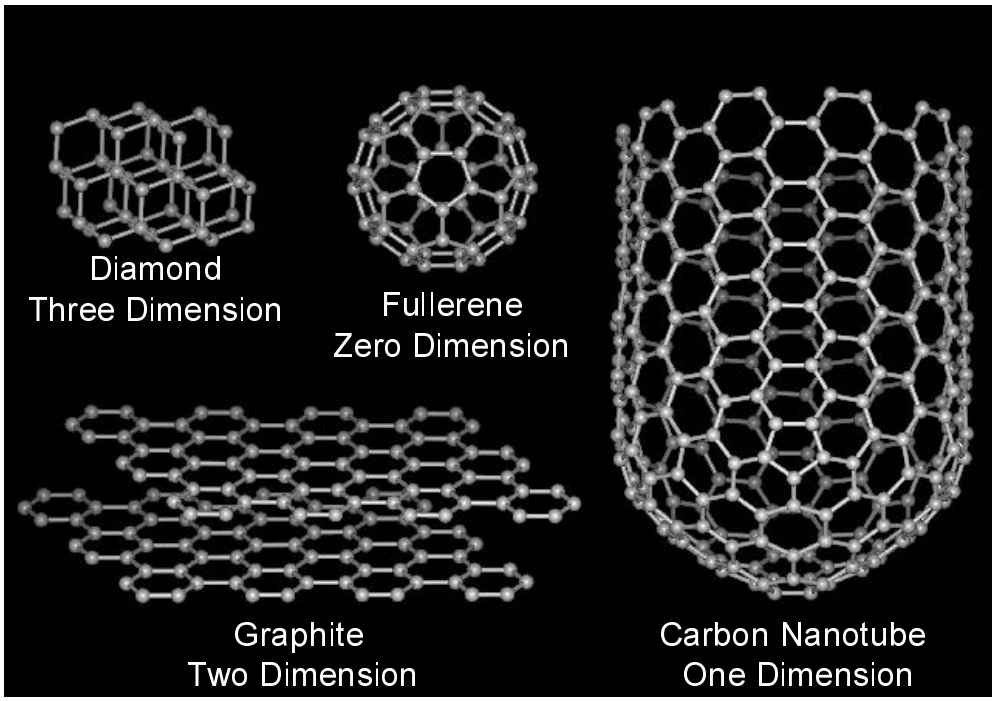

Fig. 3.1: Allotropes of carbon

impurities, a purification process [61–66] is generally required prior to its use. Although the CNTs produced by these methods usually necessitates such a purification process, these production methods are firmly established at present. In particular, the HiPco method [67] that utilizes the disproportionation reaction of CO gas is now regarded as a commercially feasible method for the mass production of CNTs. At the same time, the CVD method with a supported catalyst is currently being intensively studied as a promising technique. The alcohol CCVD method [68] is one of such technique and can produce high-quality CNTs that are almost free from the aforementioned impurities even in the as-synthesized state.

With the development of production methods of CNTs, experimental studies for specific applications have become active, and many innovative applications have been studied and proposed, such as one-dimensional (1D) quantum wire [69], field effect transistor (FET) [70, 71], cold cathodes for electron emitters [72, 73], probe tips for atomic force microscopes (AFM) [74, 75], and saturable absorbers for ultrashort pulse generation [22, 49, 50, 52]. In any application, the 1D geometry, nanoscale size, and the

physical/chemical properties of CNTs are of great importance.

CNTs have typically 0.6 $\sim$ 2 nm diameter and 1μm length which is nearly identical 1D structure. CNTs structures and their physical properties are determined by their diameter and chiral angle (rolling direction of graphene sheet). The structure of the graphene sheet is schematically presented as a hexagonal lattice as shown in Fig. 3.2. The shadowed rhombus indicates a unit cell of the graphene, which contains two non-equivalent C atoms. The distance between neighboring atoms a_{c-c} is 1.42 Å, and vectors $\boldsymbol{a}_1$ and $\boldsymbol{a}_2$ represent the unit vectors of the cell. The Brillouin zone of the graphene is denoted in Fig. 3.2 as a shadowed hexagon, and vectors $\boldsymbol{b}_1$ and $\boldsymbol{b}_2$ are the reciprocal vectors. These vectors are expressed as

$$\boldsymbol{a}_1 = \left(\frac{\sqrt{3}}{2}a, \frac{a}{2}\right), \quad \boldsymbol{a}_2 = \left(\frac{\sqrt{3}}{2}a, -\frac{a}{2}\right) \tag{3.1}$$

and

$$\boldsymbol{b}_1 = \left(\frac{2\pi}{\sqrt{3}a}, \frac{2\pi}{a}\right), \quad \boldsymbol{b}_2 = \left(\frac{2\pi}{\sqrt{3}a}, -\frac{2\pi}{a}\right) \tag{3.2}$$

based on the $x-y$ and k_x-k_y coordinates, respectively, as shown in Fig. 3.2. In these equations, the lattice constant of the 2D graphene is defined as $a \equiv |\boldsymbol{a}_1| = |\boldsymbol{a}_2| = 1.42$ Å$\times 3^{1/2} = 2.46$ Å. By convention, high symmetry points at the center, corner, and the midpoint of the neighboring corners of the Brillouin zone are expressed as Γ, M, and K points, respectively.

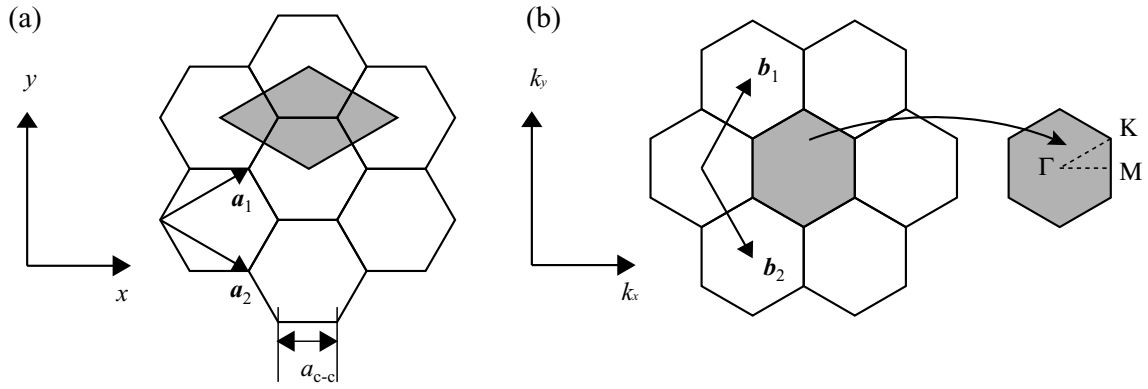

Fig. 3.2: Schematics of Unit Cell of 2D graphene sheet

The unit cell of a CNTs is enlarged when it is compared to that of the graphene due to the lower symmetry of CNTs. Figure 3.3 shows an unrolled hexagonal lattice of a CNT, in which the unit cell of a certain type of CNT is indicated as a shadowed area. The vectors $\boldsymbol{C}_h$ and T that connect two crystallographically equivalent sites in the circumferential and axial directions of CNTs, respectively, are also shown. These vectors are called the "chiral vector" and the translational vector, respectively, as further explained below.

The chiral vector $\boldsymbol{C}_h$ is expressed in terms of real-space unit vectors $\boldsymbol{a}_1$ and $\boldsymbol{a}_2$ and two integers n and m $(0 \leq m \leq n)$ as

$$\boldsymbol{C}_h = n\boldsymbol{a}_1 + m\boldsymbol{a}_2 \equiv (n, m) \tag{3.3}$$

The type of CNT is completely specified by the two integers (n, m) through the definition given in Eq. 3.3. Since the length of $\boldsymbol{C}_h$ indicates the circumferential length of the CNT,

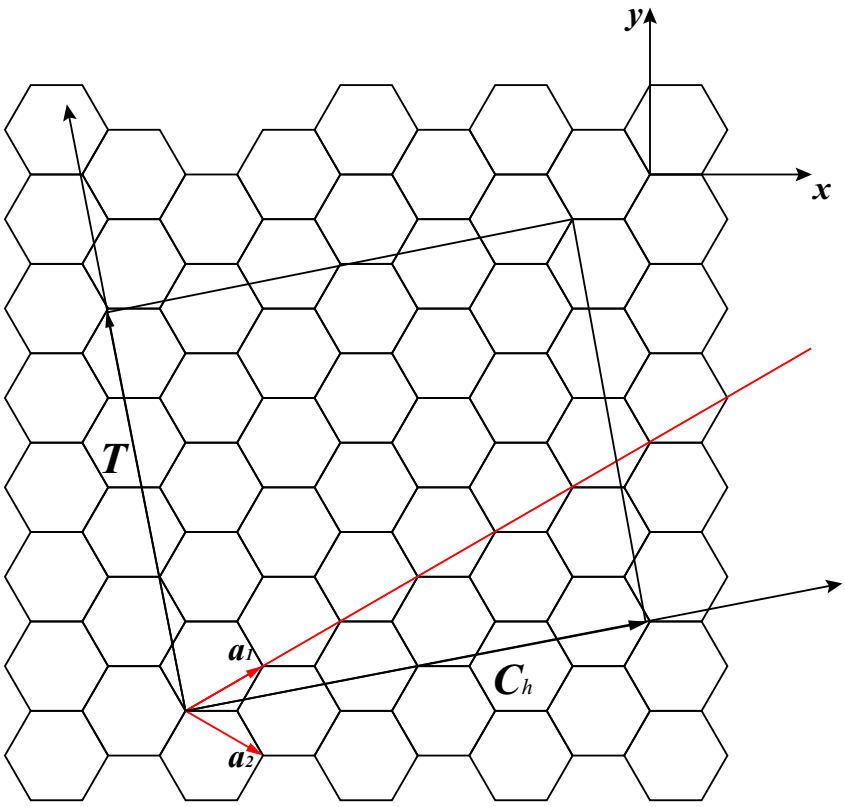

Fig. 3.3: Schematics of 2D graphene sheet

the diameter of the CNT, d_t, is expressed as

$$d_t = \frac{|\boldsymbol{C}_h|}{\pi} = \frac{\sqrt{\boldsymbol{C}_h \cdot \boldsymbol{C}_h}}{\pi} = \frac{a\sqrt{n^2 + m^2 + nm}}{\pi} \tag{3.4}$$

Here, $a \equiv |\boldsymbol{a}_1| = |\boldsymbol{a}_2| = 1.44$ Å$\times 3^{1/2} = 2.49$ Åis the lattice constant of the honeycomb lattice of the CNT. A slightly greater C-C bond length in CNTs compared to that in the graphene (1.42 Å) should be noted.

The angle formed by $\boldsymbol{C}_h$ and $\boldsymbol{a}_1$ is termed chiral vector θ, and its value is $0 \leq \theta \leq 30^\circ$ due to the hexagonal symmetry of the honeycomb lattice; specifically, it is expressed as

$$\cos\theta = \frac{\boldsymbol{C}_h \cdot \boldsymbol{a}_1}{|\boldsymbol{C}_h||\boldsymbol{a}_1|} = \frac{2n + m}{2\sqrt{n^2 + m^2 + nm}} \tag{3.5}$$

The translational vector T is defined as the unit vector of a 1D CNT, which is parallel to the CNT axis. From the relationship $\boldsymbol{C}_h \cdot T = 0$ (Fig. 3.3),

$$T = t_1\boldsymbol{a}_1 + t_2\boldsymbol{a}_2 \equiv (t_1, t_2), \quad t_1 = \frac{2m + n}{d_R}, \quad t_2 = -\frac{2n + m}{d_R} \tag{3.6}$$

where d_R is the greatest common divisor (gcd) of $(2m + n)$ and $(2n + m)$. Using the above defined d_R, the number of hexagons in the unit cell of a CNT N is expressed as

$$N = \frac{|\boldsymbol{C}_h \times T|}{|\boldsymbol{a}_1 \times \boldsymbol{a}_2|} = \frac{2(n^2 + m^2 + nm)}{d_R} \tag{3.7}$$

Therefore, there are $2N$ carbon atoms in the unit cell of a CNT. For example, $(n, m) = (4, 2)$ CNT shown in Fig. 3.3 has 28 hexagons in the unit cell.

Since the unit cell of a CNT is 2D and specified by the orthogonal lattice vectors $\boldsymbol{C}_h$ and T, as shown in Fig. 3.3, the reciprocal lattice vectors corresponding to the circumferential direction $\boldsymbol{K}_1$ and the axial direction $\boldsymbol{K}_2$ are defined such that the following relationships are satisfied:

$$\boldsymbol{C}_h \cdot \boldsymbol{K}_1 = \boldsymbol{T} \cdot \boldsymbol{K}_2 = 2\pi, \quad \boldsymbol{C}_h \cdot \boldsymbol{K}_2 = \boldsymbol{T} \cdot \boldsymbol{K}_1 = 0 \tag{3.8}$$

Solving these relations using Eqs. 3.6 and 3.7, $\boldsymbol{K}_1$ and $\boldsymbol{K}_2$ are expressed as

$$\boldsymbol{K}_1 = \frac{1}{N}(-t_2\boldsymbol{b}_1 + t_1\boldsymbol{b}_2) \tag{3.9}$$

$$\boldsymbol{K}_2 = \frac{1}{N}(m\boldsymbol{b}_1 - n\boldsymbol{b}_2) \tag{3.10}$$

The electronic structure of a CNT can be obtained from that of 2D graphite. When the energy dispersion relation of 2D graphite is expressed as $E_{g,2\mathrm{D}}$, N pairs of 1D energy dispersion relation $E_\mu(k)$ are written as

$$E_\mu(k) = E_{g,2\mathrm{D}}\left(k\frac{\boldsymbol{K}_2}{|\boldsymbol{K}_2|} + \mu\boldsymbol{K}_1\right), \quad (\mu = 0, \cdots, N-1, \text{and} -\frac{\pi}{|\mathrm{T}|} < \mathrm{k} < \frac{\pi}{|\mathrm{T}|}) \tag{3.11}$$

Here, k denotes the wave number along the CNT axis. If these energy dispersion curves are collected (or folded) into the first Brillouin zone of the 2D graphite by translating them using multiples of $\boldsymbol{K}_1$ and $\boldsymbol{K}_2$.

Such a quantized wave vector of CNTs causes a sharp divergence in their eDOS, termed "van Hove singularities," that is characteristic of 1D materials. Since it is obvious that the cutting line of this CNT-described by Eq.3.11-does not pass the K-point, in which the valence and conduction bands meet in the case of 2D graphite, the $(n, m) = (4, 2)$ CNT is semiconducting in which eDOS is absent at the Fermi level. On the other hand, the CNT is metallic in which eDOS exists at the Fermi level. In general, $\mathrm{mod}(n-m, 3) = 0$ CNTs are metallic and $\mathrm{mod}(n-m, 3) \neq 0$ CNTs are semiconducting. One of the most important characteristics of CNTs is that the difference of metallic/semiconducting transport properties is determined solely by the chirality. Figuire 3.4 shows the simulated eDOS of the two CNTs, (9,0) and (10,0). $\mathrm{mod}(n-m, 3) \neq 0$ for (10,0) for CNTs and $\mathrm{mod}(n-m) = 0$ for (9,0) CNTs, thereby (10,0) CNTs are semiconducting which do not have eDOS at Fermi level and (9,0) CNTs are metallic which posses eDOS at Fermi level as shown in Fig. 3.4.

Figure 3.5 shows the chiral mapping of (n, m) CNTs that are either metallic (open circles) or semiconducting (solid circles). Any chirality is specified either by two integers (n, m) or equivalently, a combination of diameter d and chiral angle θ, as schematized

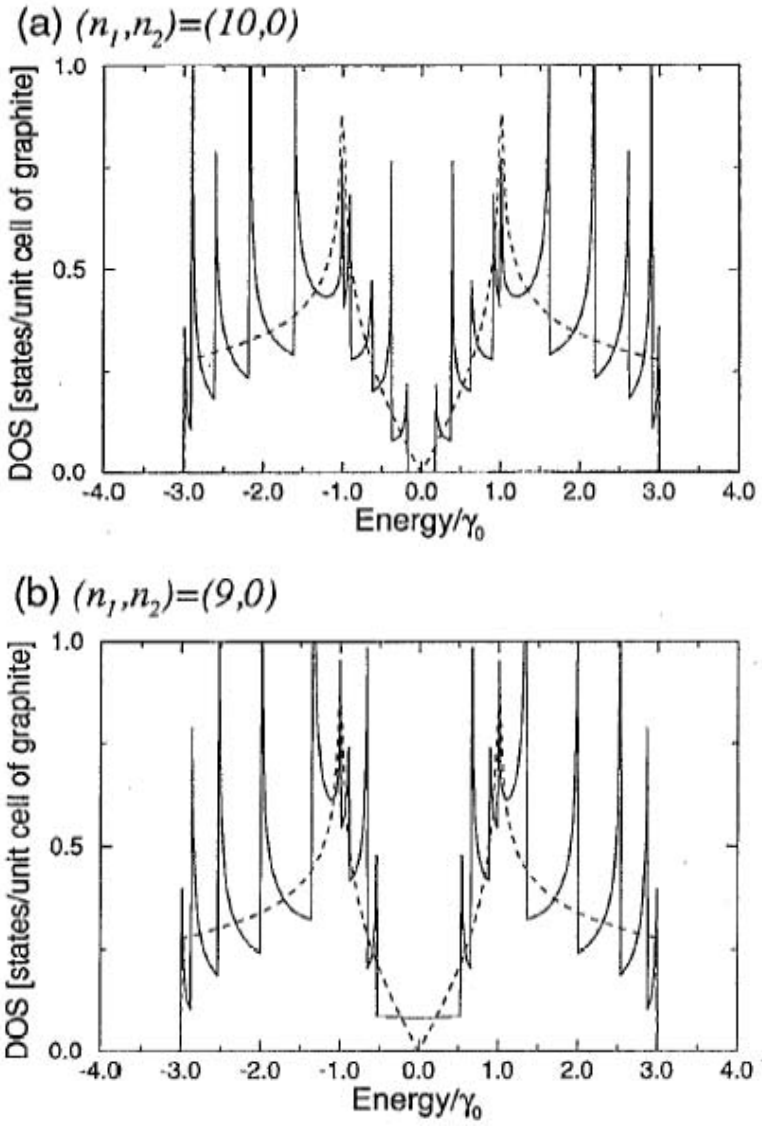

Fig. 3.4: Examples of eDOS (a) (10,0) semiconducting, (b) (9,0) metallic [56]

in this figure. Among these, the CNTs with $m = 0$(i.e., $\theta = 0°$) and $n = m$(i.e., $\theta = 30°$) chirality are termed "zig-zag" and "armchair" types, respectively.

As already mentioned, each semiconducting CNTs has a bandgap and absorbs the light which has the wavelength corresponding to the energy gap. Band gap is almost inversely proportional to the tube diameter. Figure 3.6 shows the diameter dependence of bandgap which often called "Kataura-plot" [76]. By selecting the CNTs diameter, absorption wavelength band is tunable. The tunability is of importance to realize various CNTs

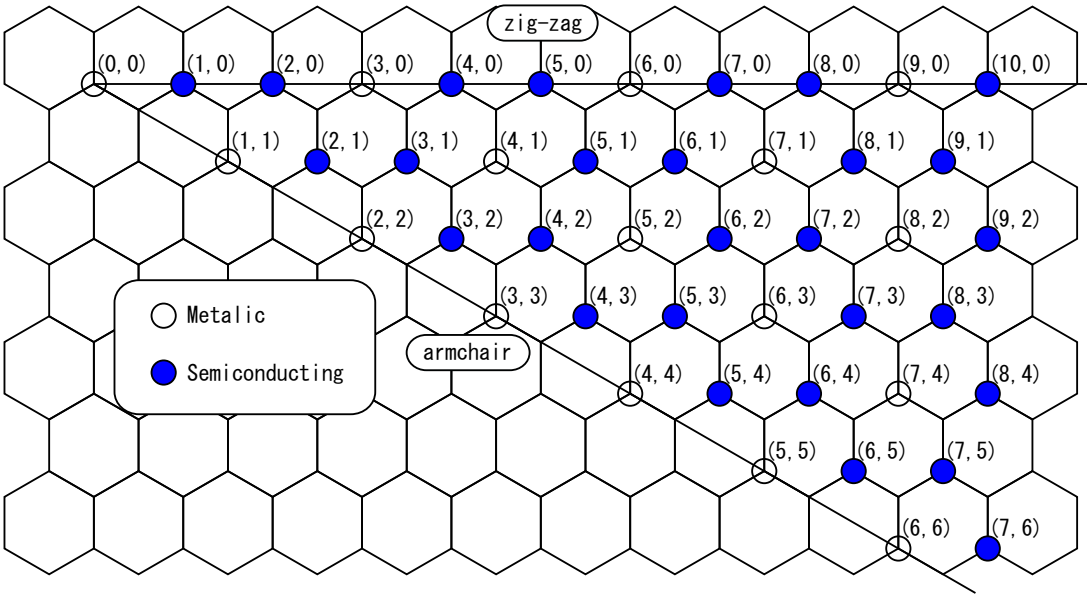

Fig. 3.5: Schematics of Chiral Mapping

based optical devices. Figure 3.7 is an example of CNTs absorption spectrum which weree sprayed onto quarts substrate and covers optical communication band 1.55μm.

The saturable absorption which will be explained in subsection 3.2.2 has been reported in several groups [22, 49]. The attractive CNTs properties not only saturable absorption but also the chemically, mechanically stability, easy fabrication, small footprint, ultrafast response time and ultrahigh optical nonlinearity which is described in subsection 3.2.3. Because of these characteristics, optical applications of CNTs ("CNTs photonics") have been intensively investigated. Figure 3.8 shows examples of CNT photonics applications. For non-telecom applications, passively mode-locked fiber laser which has low repetition rates ($\sim$MHz) can be used as optical processing and optical coherence tomography because the lasers has the high peak power pulse and broad optical spectrum. On the other hand, for telecom applications, we can realize CNT based nonlinear optical devices which work in ultrafast network systems. CNTs optical properties have been studied for a long time, however CNTs applications for optical devices is now cutting edge research field. CNTs photonics have a large potential in photonics applications.

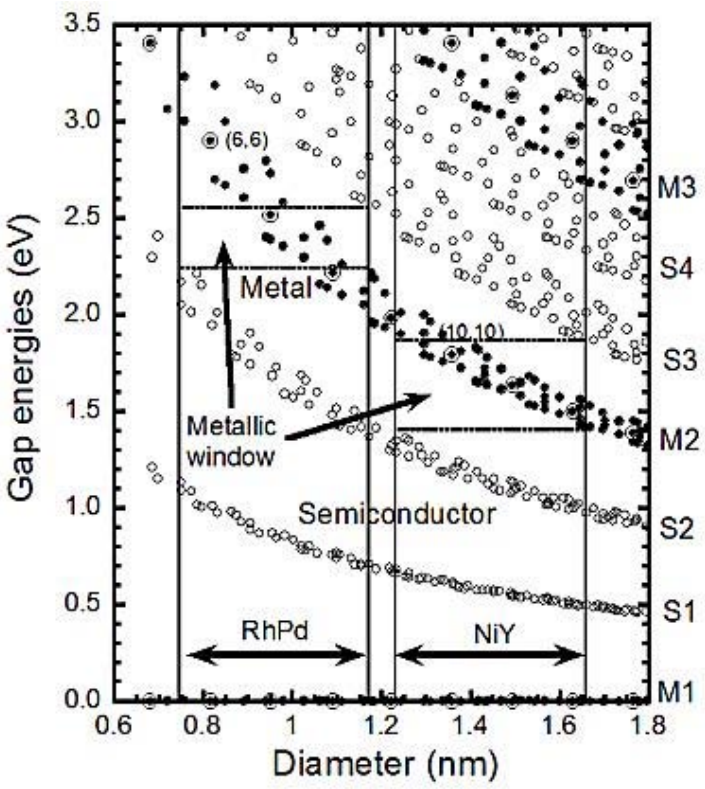

Fig. 3.6: Kataura Plot [76]

3.2.2 Saturable Absorption

Basic properties of CNTs are explained in previous subsection, and in this subsection especially the saturable absorption property of CNTs is introduced.

Semiconducting CNTs absorb the light whose energy is same as CNTs bandgap, and the bandgap is controllable by choosing appropriate CNTs diameter. The CNTs work as saturable absorbers in the absorption band. A saturable absorber is a material which change its absorbance depends on the power of incident light. Saturable absorbers absorb the light which has low intensity, whereas the attenuation decreases due to the saturation of absorption in case of high intensity light.

This phenomenon can be understood as eDOS occupation in conduction band of saturable absorber material (Fig. 3.9). If the low intensity light incidents, the electrons in valence band are excited up to conduction band, and all photons are absorbed. On the other hand, if the optical intensity is high, some photons are not absorbed because

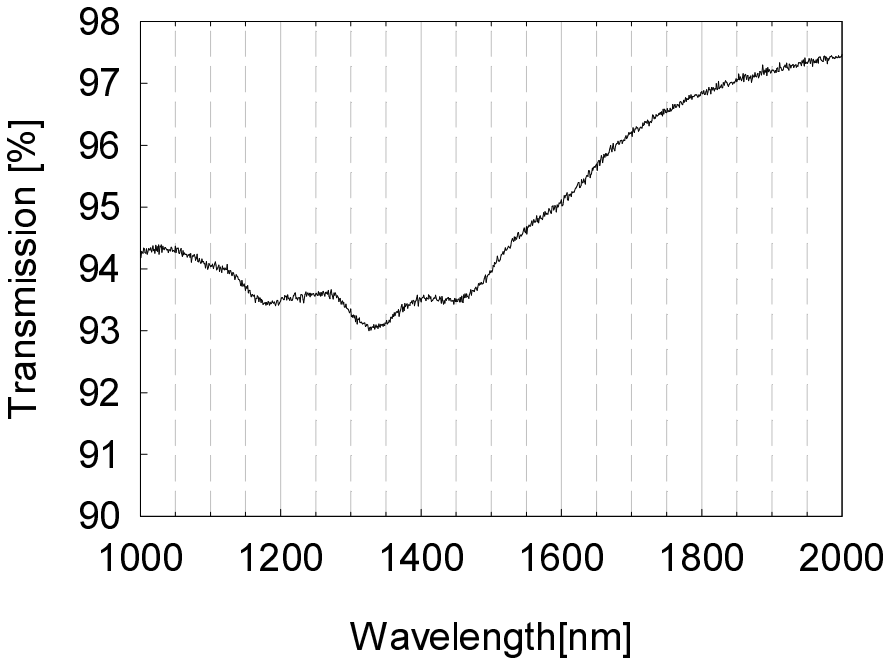

Fig. 3.7: Example of Absorption Spectrum of CNTs

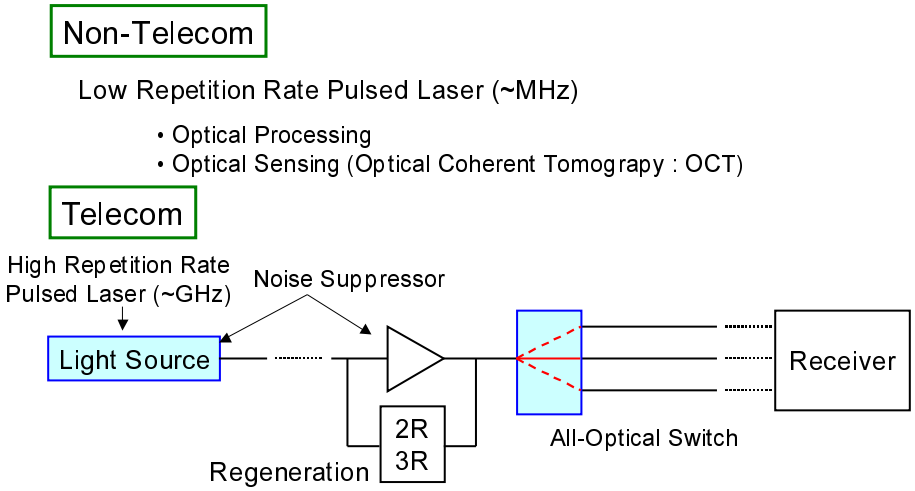

Fig. 3.8: CNTs photonics

the eDOS in conduction band is occupied with other electrons which excited by the light. Thus, the optical intensity dependent transparency, the saturable absorption reveals.

This kind of intensity dependent attenuation allows the high-intensity components

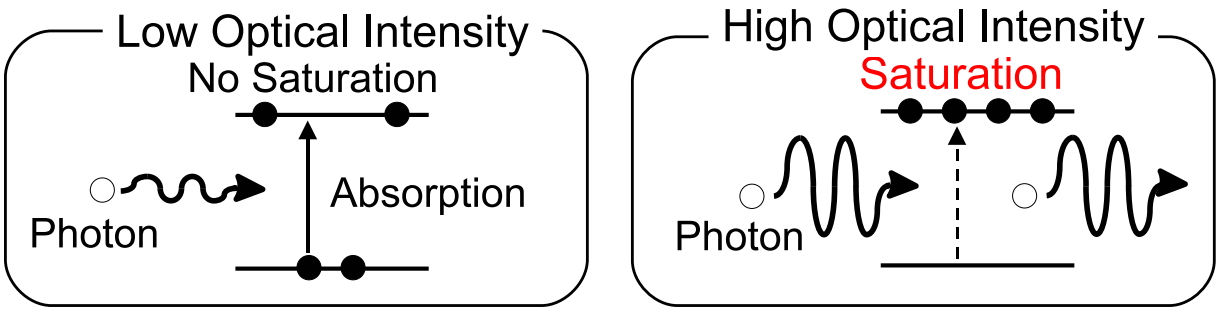

Fig. 3.9: Schematics of Saturable Absorption

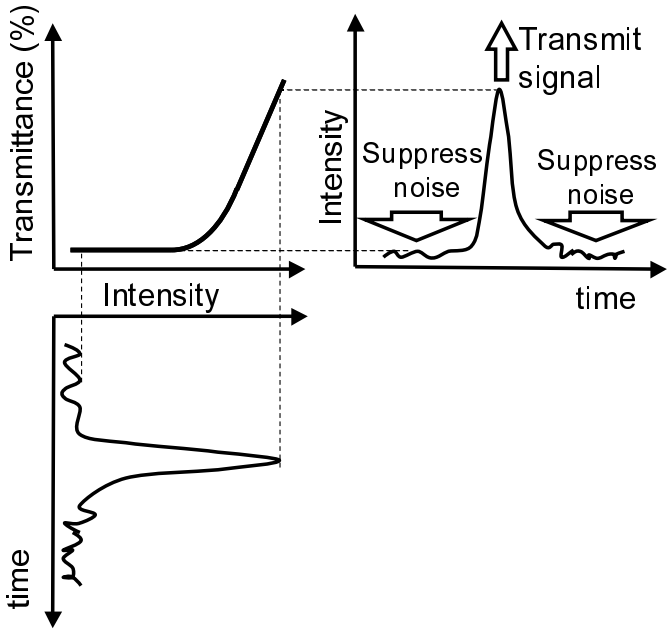

Fig. 3.10: Schematics of Noise Suppression by Saturable absorber

of an optical pulse to pass through the saturable absorber, while the lower intensity components of the pulse, such as the pulse wings, pedestals, and background CW radiation do not pass (Fig. 3.10). When a saturable absorber is inserted in a laser cavity, amplified spontaneous emission (ASE) noise of gain medium will be shaped to be a pulse train. Every round trip, light pass the saturable absorber as high intensity noise with low loss and low intensity noise with high loss, resulting in intensity contrast will be emphasized. Finally, light start to oscillate in pulsed state.

For the ultrashort pulse generation application, a saturable absorber with a fast

recovery time is required for stabilizing laser mode locking, while a slower recovery time could facilitate laser self-starting. Recovery time of CNTs have been reported to be less than 1ps, and CNTs are suitable material for ultrashort pulse generation. However, recovery time is not so fast of CNTs only consisted by semiconducting CNTs (30ps) [77]. The ultrafast response time of CNTs are based on bundle and entanglement of semiconducting and metallic CNTs because electrons which are excited by photons in semiconducting CNTs tunnel and couple to metallic CNTs, resulting in ultrafast recovery time of semiconducting CNTs. Up to now, selective fabrication technique of semiconducting and metallic CNTs have not been developed yet. As fabricated CNT samples consists of CNTs which has several different chirality. Therefore, the CNT samples inherently have ultrafast recovery time less than 1ps.

3.2.3 Optical Nonlinearity of Carbon Nanotubes

In subsection 3.2.2, light induced transparency, saturable absorption characteristics is explained. This section overviews the second attractive characteristics of CNTs for optical device applications, ultra high optical nonlinearity.

In general, high optical nonlinearity and recovery time are trade-off. CNTs ultrafast response time is due to the tunneling to the neighbouring CNTs as mentioned in subsection 3.2.2. The materials which have high optical nonlinearity posses following features.

- Nanostructure
- sp^2 bonding (π electrons)
- saturable absorption

CNTs have all the features listed above and have been expected as ideal materials for nonlinear optical processing.

For example, third order optical nonlinearity (n_2) of CNTs is reported as $n_2 = 2 \times 10^{-8}\mathrm{cm}^2/\mathrm{W}$ in reference [78]. In nonlinear optical processing research fields, nonlinear

coefficient (γ) is used to express nonlinearity of materials. The nonlinear coefficient is expressed as

$$\gamma = \frac{2\pi n_2}{\lambda_0 A_{\text{eff}}} \tag{3.12}$$

where λ_0 and A_{eff} are the wavelength of light and effective area. The nonlinear coefficient of CNTs calculated to be $\gamma = 1.0134 \times 10^8 \text{W}^{-1}\text{km}^{-1}$ from reference [78]. Here, we assumed $A_{\text{eff}} = 80\mu m^2$ which is typical value for singled mode optical fibers. The nonlinear coefficient in the order of $10^8 \text{W}^{-1}\text{km}^{-1}$ is quit high compared with commonly used devices. Fiber type devices and semiconductor type devices are often used types of optical nonlinear devices. High nonlinear coefficient and high speed response time are in trade-off relation. Typically, the optical fiber type has low nonlinear coefficient and high response time. On the other hand, semiconductor based devices has high nonlinear coefficient and low response time. CNTs posses much higher nonlinear coefficient and response speed because of their nanostructures and bundled conditions.

There are two relaxation process in bundled CNTs. One is a non-radiative relaxation such as multi-phonon emission through electron-phonon coupling [79]. Another is an excited electron tunneling to neighbouring CNTs. Since the CNTs whose electrons are excited and whose electrons are relaxed are different, this relaxation process is high speed shorter than 1ps, and both high speed recovery and high nonlinearity reveal in bundled CNTs. It indicates the device size and power consumption can be drastically reduced and highly integrated devices are potentially expected. The CNTs are used in section 3.4 as nonlinear processing materials.

3.3 Planar Waveguide-Type Saturable Absorber Based on Carbon Nanotubes

3.3.1 Introduction

After CNT optical devices were first demonstrated, three types of CNTs based device structures have been proposed. They are depicted in Fig. 3.11, transmission-type, reflection-type and fiber-type. However, these devices are all bulky and have difficulties in enhancing CNTs effect and integration. A solution to these problems is distributing the CNTs along the waveguide instead of using CNT thin layer.

In this section, we examine the CNT-based planar waveguide-type saturable absorber as a first-step to realize integrated all-optical waveguide devices based on CNTs. CNTs were sprayed onto over-cladding-less silica-based waveguides fabricated by UV beam scanning as described in chapter 2. The CNT sprayed waveguide perform as a saturable absorber with an interaction between evanescent wave of guided light and sprayed CNTs. For demonstration of the saturable absorber, we inserted the saturable absorber into the fiber ring laser cavity as a passive mode-locker.

3.3.2 Saturable Absorber Fabrication Process

Fabrication process of planar waveguide-type saturable absorbers based on CNTs is described in Fig.3.12. First, we fabricated over-cladding-less silica-based waveguides by

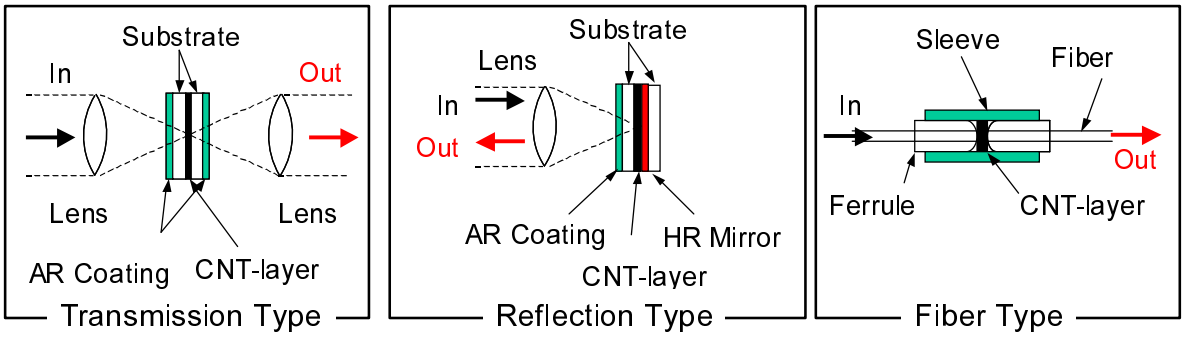

Fig. 3.11: Schematics of CNTs based devices

UV beam scanning using the experimental setup described in section 2.6. Then, we sprayed purified CNTs onto the waveguide to form the CNTs-layer. Detail fabrication process is explained in followings.

The substrates which had a silica-on-silicon two-layer structure fabricated by the FHD technique were prepared. We used over-cladding-less two layer structure for exudation of evanescent field out to air. The heights of the under-cladding layer and the Ge-doped layer were 40, 6μm, respectively. The refractive index difference between Ge-doped layer and under cladding layer was 0.75%. To enhance the photosensitivity, the substrates had been loaded with hydrogen at 130 atm for 1 week. UV beam from a frequency doubled argon ion laser which has the power of 90mW was focused so that the spot diameter became around 5μm at the substrate fixed on a two-dimensional translation stage. Waveguides were fabricated by translating the stage under the focused spot in 60μm/s. After UV scanning, the substrates were annealed at 80°C for 24 hours to stabilize the UV-induced refractive index change.

We sprayed purified CNTs onto the waveguides. The utilized CNTs sample is synthesized by the HiPco method [67] that uses the disproportionation reaction of CO (Carbon Mono-oxide) gas.

The purification process which is used in this thesis described in followings. First, CNTs were immersed into the solution, N,N-dimethylformamide (DMF), and CNTs were separated and dispersed by sonication bath. DMF is a solution which is commonly used for dispersing CNTs. CNTs have light weight and big aspect ratio, therefore CNTs easily gather each other and form large bundles. DMF has the suitable properties

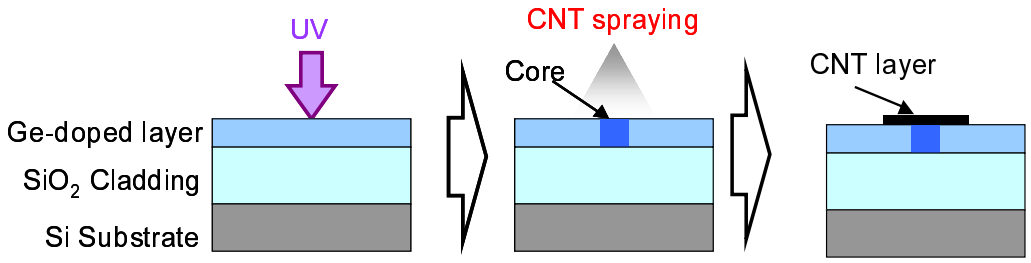

Fig. 3.12: Schematics of planar waveguide type CNTs based devices fabrication process

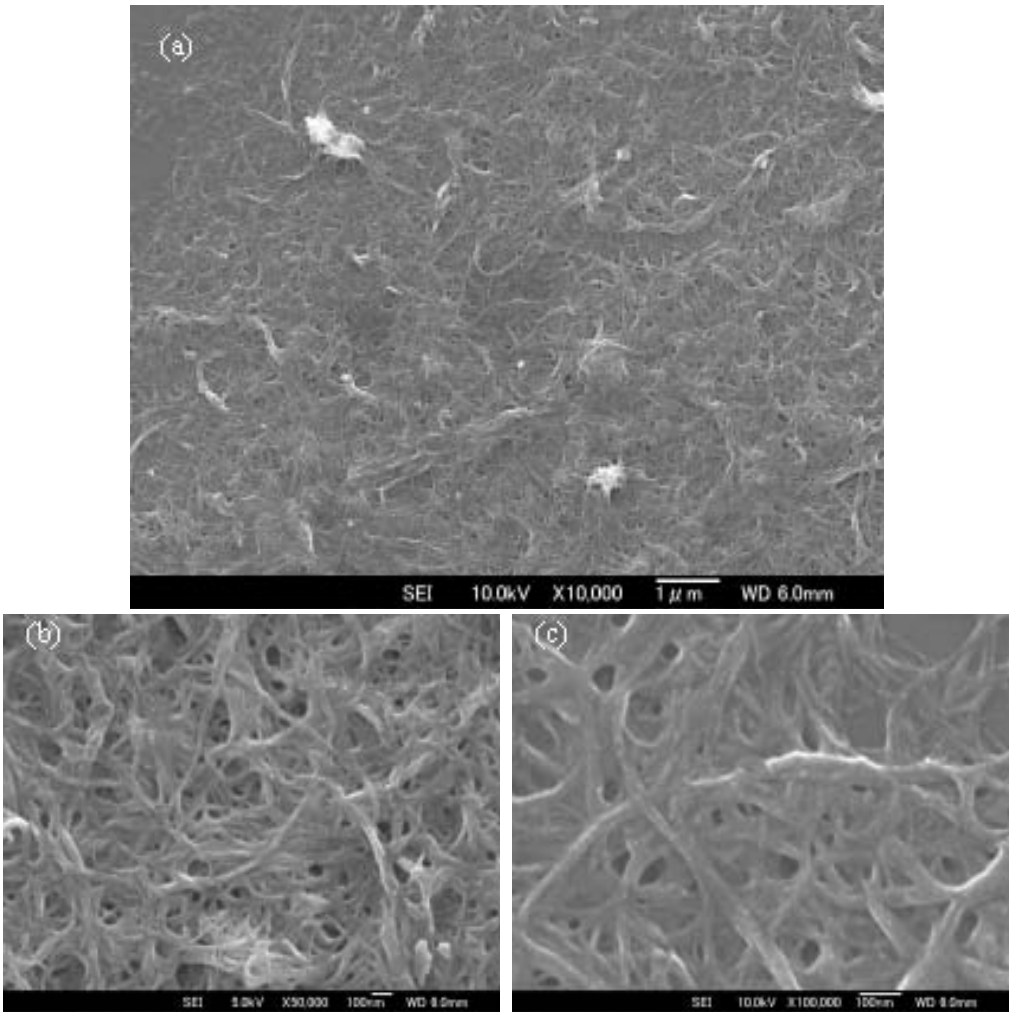

Fig. 3.13: FE-SEM image of sprayed CNTs (a)10,000 magnitude (b) 50,000 magnitude (c)100,000 magnitude

to prevent the bundling. The sonicated solution was centrifuged at 5000G for 5 minutes, and supernatant was decanted for use. By the centrifugation and decanting process, impurities such as amorphous carbons, catalysts, strongly bundled CNTs were eliminated. We sprayed the solution onto the over-cladding-less waveguides, and dried up DMF by heating them. By these succeeding process, CNTs layer was coated on top of the over-cladding-less waveguides. For instance, we represent the example of a field emission scanning electron microscopy (FE-SEM) image of sprayed CNTs onto glass substrate in Fig. 3.13. CNTs were randomly deposited onto the substrate surface and bundled with each other. Density of CNTs is not so high as shown in the figure. It is

difficult to deposit uniform and thick CNT layer because spray method sputter the DMF granules and desipate many CNTs.

We prepared three CNTs-sprayed waveguides samples, sample A, B and C. Sample A and B were 10mm-long and 5mm-long, respectively and had CNTs-layer from end to end. Sample C was 5mm-long and had two parallel waveguides whose length of CNTs-layer was different. The structure of sample C will be described later in detail.

3.3.3 Saturable Absorption Characteristics

We prepared three samples in previous subsection. We examine the basic properties of the samples, especially properties corresponding to the absorption in this subsection. The properties of samples were measured by butt coupling with SMF without index matching oil.

Figure 3.14 depicts the transmission spectrum of sample A for maximum loss polarization and minimum loss polarization. Absorption band of sample A covers broad wavelength range from 1400nm to 1700nm, including around 1550nm communication band. Since the CNT layer was not uniform and caused scattering, insertion loss of

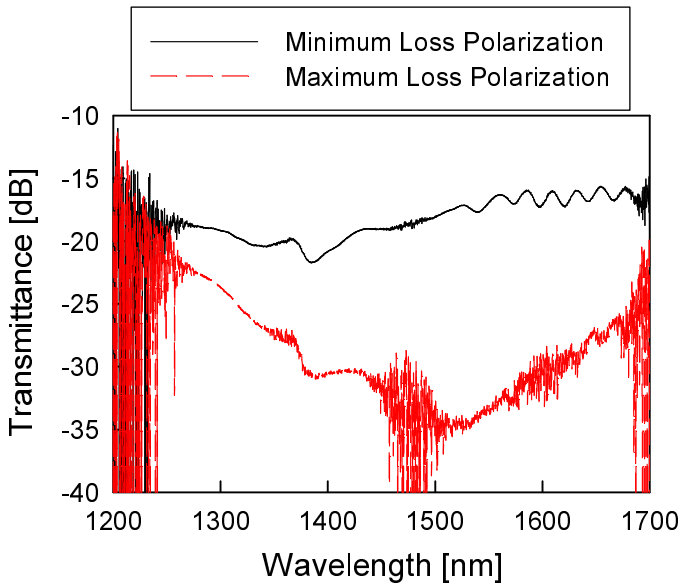

Fig. 3.14: Transmittance spectrum of sample A

sample A was high. CNTs have high polarization dependence of absorption due to their asymmetric structure [80, 81]. We explain the reason of high polarization dependence of the device later in detail.

To measure saturable absorption, we used nonlinear polarization rotation passively mode-locked pulsed laser [82, 83] which has the center wavelength of 1562nm, the pulse width of 1.05ps and repetition rate of 4.2MHz. We amplified the output light by an EDFA and controlled its polarization state by a polarization controller(PC). The light was butt-coupled into a sample, and transmitted power was measured by an optical power meter. By changing the EDFA gain, we measured the saturable absorption characteristics of three samples. The saturable absorption characteristics of sample A in maximum loss polarization is illustrated in Fig. 3.15. From Figs. 3.14 and 3.15, we confirmed sprayed-CNTs and evanescent wave interacted with each other, and these samples worked as saturable absorber. Comparing with sample A, sample B had smaller insertion loss and polarization dependence. Figure 3.16 depicts the saturable absorption characteristics of sample B for two polarization, maximum loss polarization and minimum loss polarization. In minimum loss polarization, there is no obvious saturable absorption characteristic. On the other hand, in maximum loss polarization, we observed saturable absorption characteristic.

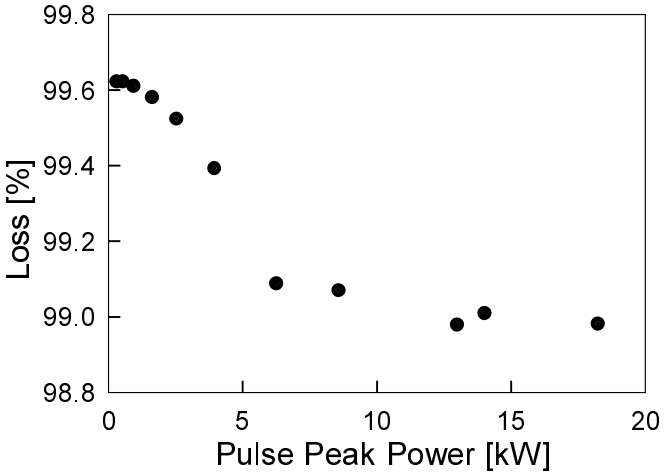

Fig. 3.15: Saturable absorption characteristics of sample A

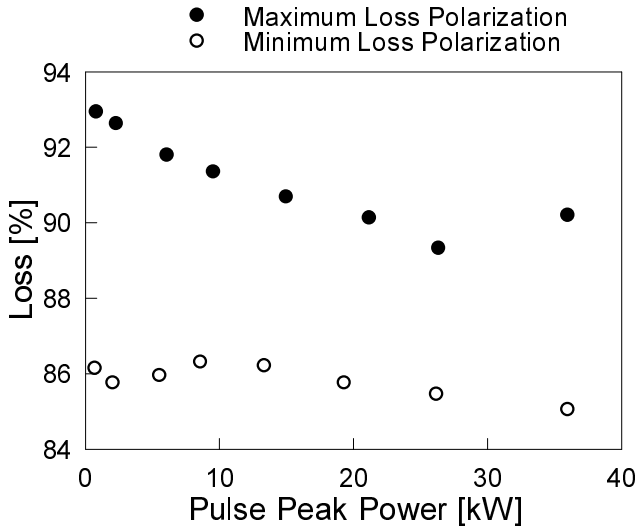

Fig. 3.16: Saturable absorption characteristics of sample B

CNTs absorption is highly polarization dependent because of their asymmetric structure. It is theoretically [84] and experimentally [80,81] confirmed that absorbance is maximum when electrical field and CNT axis vector are parallel, and is minimum when electrical field and CNT axis vector are perpendicular. Considering these results, we can understand the polarization dependence of samples as followings. The axis vectors of CNTs sprayed on top surface of the waveguide are in random direction as shown in Fig. 3.13. The axis vector components are all in XZ-plane and are not in Y-axis direction (Fig. 3.17). CNTs axis vector are perpendicular for TM mode which electrical field are mainly in Y-axis. For TE mode, CNTs axis vector components which are in X direction contribute to absorption. Hence, TE mode is maximum loss, or absorption, polarization state and TM mode is minimum loss, or absorption, polarization state.

Controlling CNTs effect is one of the important factors for realizing integrated optical circuits. There are two ways to control CNTs effect, controlling CNT-layer thickness and CNT sprayed region length. We can not compare sample A and B for CNTs effect with different length because two samples had too high loss and total waveguide lengths were different with each other. Therefore, we prepared 5mm-long two waveguides, which have different CNTs-sprayed region length with each other, on a single substrate, sample C. One waveguide had 0.5mm-long of CNT-sprayed region length, and the other had

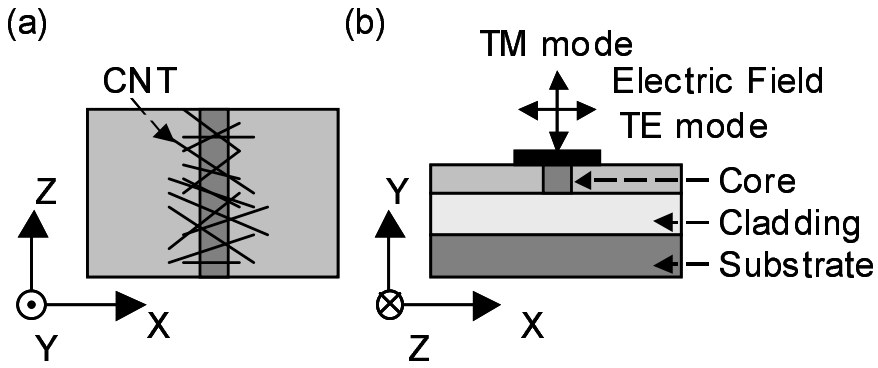

Fig. 3.17: Schematics of the structures of the samples (a) side view (b) top view

2.0mm-long. Figure 3.18 shows the saturable absorption characteristic for maximum loss polarization. Data points are normalized with lowest input power data. The waveguide which had longer CNT-sprayed region length has the deeper saturable absorption depth. We confirmed CNTs effect can be controlled by changing CNTs sprayed region length.

3.3.4 Application to Passively Mode-Locked Fiber Laser

In previous subsection, saturable absorption characteristics of three samples were confirmed. In this subsection, we applied the saturable absorber in a fiber laser cavity,

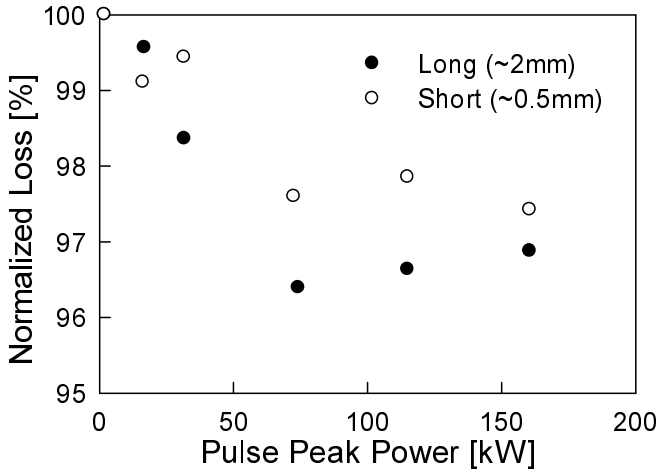

Fig. 3.18: Saturable absorption characteristics of sample C in maximum loss polarization

and the demonstrate the system application of the planar waveguide-type CNTs device.

The schematic of the mode-locked fiber ring laser is shown in Fig. 3.19. Since the samples had the high insertion loss, high power EDFA was used as the laser gain medium. An isolator was inserted to prevent back reflection in the cavity, especially at two end facets of a sample. We controlled the polarization state inside the ring cavity by a PC to match the best polarization state for the sample which had the polarization dependence. The 20m-long SMF was inserted to control the total dispersion in the ring cavity to be nearly zero. We amplified the light produced from 3dB coupler by an EDFA enough to detect autocorrelation traces. One of the CNTs-sprayed silica-based over-cladding less waveguides was inserted for passive mode-locker. We used the same samples in subsection 3.3.3.

First, we inserted the 5mm-long sample B. By controlling the polarization state, the pulse oscillation was realized. Optical spectrum, autocorrelation trace of the laser output are shown in Fig.3.20(a),(b), respectively. The 3dB spectral width is 2.2 nm and measured SHG autocorrelation trace had the full-width half-maximum (FWHM) width of 1.1 ps. When transform limited sech^2 pulse waveform is assumed, pulse width is calculated to be 709 fs. To realize much shorter pulse, we utilized 10 mm long sample which has higher CNTs effect than 5 mm long sample.

Figure 3.21 shows the pulsed laser output characteristics using 10 mm long

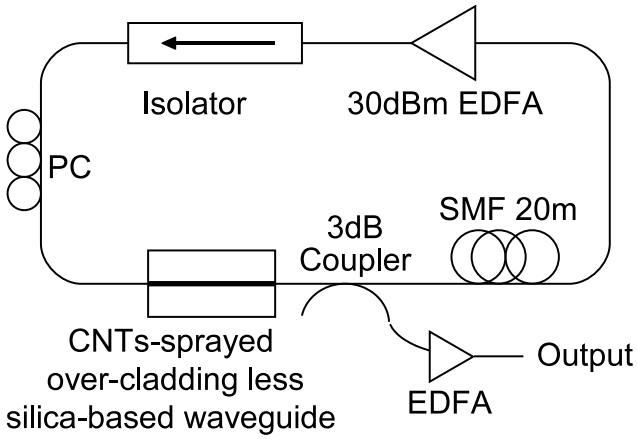

Fig. 3.19: Experimental setup for passively mode-locked laser.

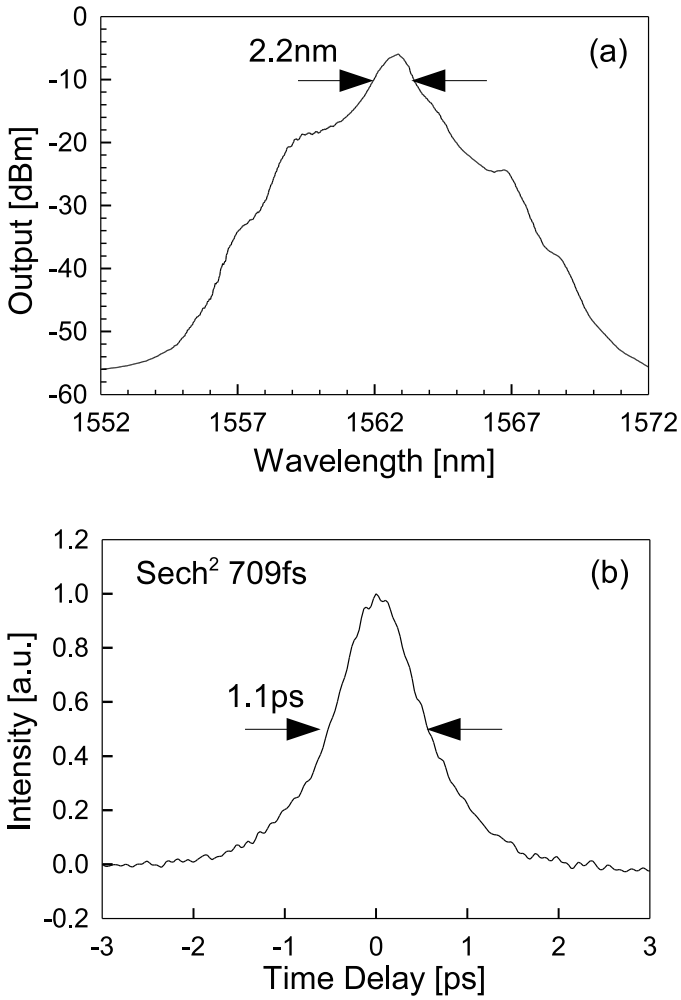

Fig. 3.20: Passively mode-locked laser output with sample B (a) Optical spectrum (b) Autocorrelation trace

sample. The laser output had the 8nm spectral width, and 290fs of FWHM of SHG autocorrelation trace (187 fs transform limited pulse). Repetition rate was measured to be 1.55 MHz. Background noise which is shown in Fig. 3.21(b) and (c) was originated from EDFA ASE noise which was located outside the laser cavity. We had confirmed pulsed oscillation did not occur by removing the samples or sprayed CNTs even if the high gain EDFA was used.

The pulsed oscillation may not be only from the saturable absorption. The combination of saturable absorption effect and nonlinear polarization rotation effect

may be the principle of this pulsed output, because the samples have PDLs. 10mm-long sample A had 15dB PDL and 5mm-long sample B had 3dB PDL. We used high power EDFA for gain medium, therefore polarization rotation effect may be occurred in the cavity. The two effect formed the pulse simultaneously at the position where the sample was inserted. These effects allow us to easily achieve the pulsed output. However, the laser stability decreased because the whole system became polarization sensitive.

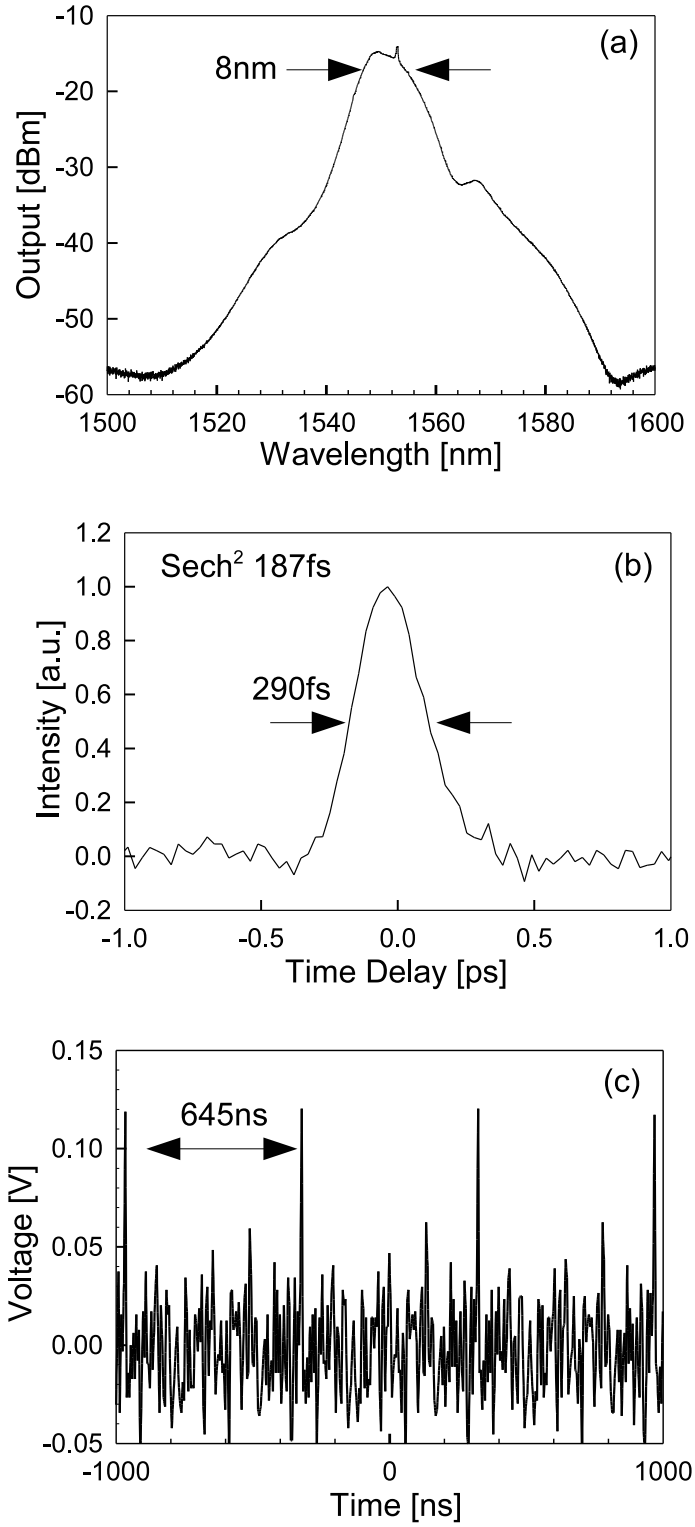

Fig. 3.21: Passively mode-locked laser output with sample A (a) Optical spectrum (b) Autocorrelation trace (c)Time Trace

3.4 All Optical Switching Using Carbon Nanotube Loaded Planar Waveguide

3.4.1 Introduction

We realized the CNTs based planar waveguide type devices which have potential for high integration in previous section 3.3. The samples revealed saturable absorption and were used for passive mode-locker. CNTs attractive characteristics, saturable absorption and ultrafast recovery time, were used. Moreover, CNTs have another attractive characteristic, high optical nonlinearity. This section is motivated to realize all optical switching using optical nonlinearity of CNTs.

There are a lot of papers that reports third order nonlinearity of CNTs theoretically [78] and experimentally [79]. However, the actual device or system application have not been yet realized for all optical switching. Motivation of this section is to realize actual system application of CNTs device for all optical switching. Although our final goal is to realize integrated CNTs based all optical switches, we employed nonlinear optical loop mirror configuration because of the device simplicity.

3.4.2 Nonlinear Optical Loop Mirror

In this section, optical nonlinearity of CNTs are utilized for all-optical switching. Before presenting the results, this subsection explains basics of optical nonlinearity and nonlinear optical loop mirror (NOLM).

NOLM is first proposed by Doran et. al in 1988 [85]. NOLM operates by nonlinear phase modulation through optical nonlinearity. Nonlinear optical phase modulation can be induced by self phase modulation (SPM) and cross phase modulation (XPM).

Optical nonlinearity is due to optical intensity dependent nonlinear response of dielectric materials. When the optical intensity of propagating light in a dielectric material is low, stimulated polarization is proportional to optical intensity. Contrary, when the optical intensity is high, stimulated polarization $\boldsymbol{P}$ reveals nonlinear response

to $\boldsymbol{E}$,

$$\boldsymbol{P} = \varepsilon_0(\chi^{(1)} \cdot \boldsymbol{E} + \chi^{(2)} \cdot \boldsymbol{EE} + \chi^{(3)} \cdot \boldsymbol{EEE} + \cdots) \tag{3.13}$$

$\boldsymbol{P}$ is mainly related to linear susceptibility $\chi^{(1)}$, and effects of refractive index and absorbance are included in this value.

$\chi^{(2)}$ reveals in materials which are not symmetric in molecular size. In materials which have the second order nonlinear susceptibility $\chi^{(2)}$, we can induce second order nonlinear effects, such as second harmonic generation (SHG), sum frequency generation (SFG), difference frequency generation (DFG), etc. There are some theoretical and experimental reports of CNTs second order nonlinearity [86, 87].

SPM is based on third order nonlinearity, and efficiency of SPM induction depends on third order nonlinear susceptibility. Third order nonlinearity can be understood by nonlinear response to electric field intensity of the refractive index, and it is expressed as,

$$n(\omega, |E|^2) = n(\omega) + n_2|E|^2 \tag{3.14}$$

where n_2 is expressed by $\chi^{(3)}$ as,

$$n_2 = \frac{3}{8n}\mathrm{Re}(\chi^{(3)}) \tag{3.15}$$

SPM is a phenomenon where a phase of a light is modulated by the intensity of the light. Phase shift during propagating in a material is expressed by

$$\phi = nk_0L = (n + n_2|E|^2)k_0L \tag{3.16}$$

where L is propagation length and $k_0 = 2\pi/\lambda$ is the wavenumber. Therefore, phase shift which is contributed by SPM is expressed as

$$\phi_{\mathrm{SPM}} = n_2k_0L|E|^2 = \gamma PL \tag{3.17}$$

where $\gamma = n_2k_0$ is nonlinear coefficient of the material which often used expression to compare optical nonlinearity of the material in optical communications fields.

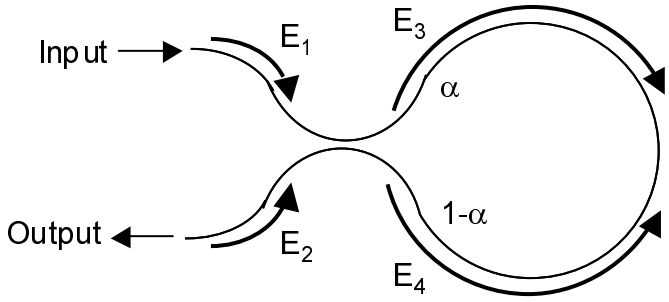

Fig. 3.22: Basic nonlinear optical loop mirror configuration

Figure 3.22 shows the simplest NOLM configuration. A input light is split into two counter-propagating lights, which return to recombine at the coupler. The optical path length is precisely the same for both propagating lights, since they follow the same path but in opposite directions. Nonlinear effect of propagation will no longer be identical for the two paths if $\alpha \neq 1/2$, since the phase velocity is intensity dependent. The device responds to differences in phases between two overlapping fields and is thus phase sensitive, but there is no need for interferometric alignment of the optical paths.

The phase shift induced by a field E propagating a distance L under the influence of SPM is given by

$$\phi = \frac{2\pi n_2 |E|^2 L}{\lambda} \tag{3.18}$$

where n_2 is nonlinear (Kerr) coefficient.

$$\begin{aligned} E_3 &= \alpha^{1/2} E_1 + i(1-\alpha)^{1/2} E_2 \\ E_4 &= i(1-\alpha)^{1/2} E_1 + \alpha^{1/2} E_2 \end{aligned} \tag{3.19}$$

The input light incident from port 1, E_{in}. After propagating around the loop length L, the light fields E_3 and E_4 is given by

$$\begin{aligned} E_3 &= \alpha^{1/2} E_{\mathrm{IN}} \exp(i\alpha |E_{\mathrm{IN}}|^2 2\pi n_2 L/\lambda) \\ E_4 &= i(1-\alpha)^{1/2} E_{\mathrm{IN}} \exp[\mathrm{i}(1-\alpha)|\mathrm{E_{IN}}|^2 2\pi \mathrm{n_2}/\lambda] \end{aligned} \tag{3.20}$$

To calculate the outputs E_{01} and E_{02}, we make the transformations $E_3 = E_4^*$ and $E_4 = E_3^*$ and invert Eqs. 3.19 to obtain the following for the output at port 2.

$$|E_{02}|^2 = |E_{\mathrm{IN}}|^2\{1 - 2\alpha(1-\alpha)[1 + \cos(1-2\alpha)|E_{\mathrm{IN}}|^2 2\pi n_2 L/\lambda]\} \tag{3.21}$$

This equation shows that for any value of $\alpha = 1/2$, 100% of the power emerges from port 2 whenever

$$|E|^2 2\pi n_2 L/\lambda = m\frac{\pi}{1-2\alpha} \tag{3.22}$$

for m odd. The minimum power occurs for m even and is given by the linear output power, or

$$|E_{02}|^2 = |E_{\mathrm{IN}}|^2[1 - 4\alpha(1-\alpha)] \tag{3.23}$$

The output switches from the low-power value to 100% every time the power increases by $\lambda/[2(1-2\alpha)n_2 L]$. The best switching ratio (i.e., the contrast between the linear off and the higher-intensity on) occurs for a closest to 0.5, but the switching energy increases correspondingly.

In this thesis, we utilized CNTs as a nonlinear optical materials to realize short loop ring.

3.4.3 Experimental Results and Discussions

We constructed NOLM configuration based all optical switch using CNT loaded silica-based waveguide as shown in Fig. 3.23. The sample which was used in this setup is the same sample which denoted as "sample A" in section 3.3. A light from laser diode at 1560nm was amplified with a 30dBm EDFA, and has been divided into two lights by 95:5 coupler. The two lights whose polarization states were controlled by two PCs counter-propagated through the sample. The sample was at slightly shifted from the center of the fiber loop. Since the length of fiber loop was ∼10m and nonlinearity of SMF is small, SPM effect was negligible in fiber loop and almost all SPM induced phase shift occurred in the sample. The optical power from through port and reflected port were measured with two power meters.

The splitting ratio contrast of NOLM is expressed as $1-4\alpha(1-\alpha)$(3.23). The contrast is 19% for 95:5 couplers. Switching characteristic is shown in Fig. 3.24. We realized the splitting ratio contrast of ∼19% by the configuration.

Phase shift by SPM is given by $\phi = \gamma PL$ (3.17). When we ignore the loss of the sample and SPM in pigtailed fiber of coupler and PCs, and phase shifts were purely from optical nonlinearity in the sample, γ of the sample is estimated to be the magnitude of $10^6 \mathrm{W}^{-1}\mathrm{km}^{-1}$.

As explained in subsection 3.2.3, simulated optical nonlinearity of CNTs is around the

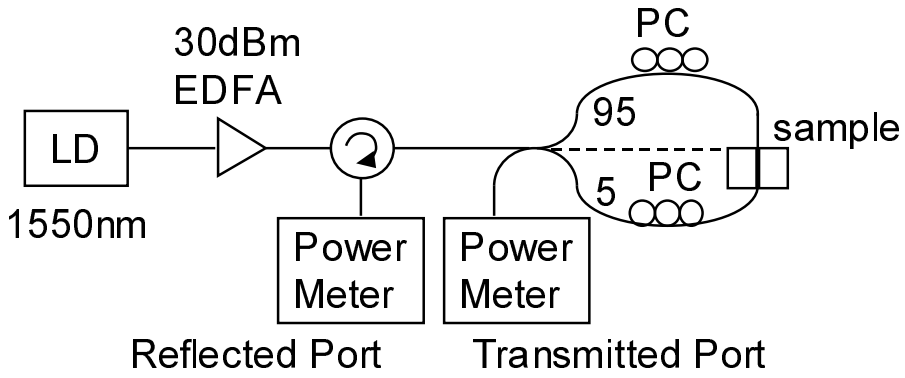

Fig. 3.23: Nonlinear optical loop mirror configuration

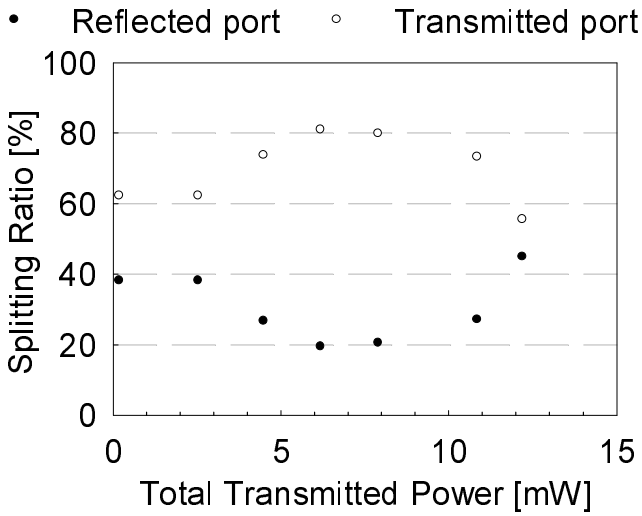

Fig. 3.24: Switching characteristics

order of $10^8 W^{-1}km^{-1}$. The estimated optical nonlinear coefficient of the sample was two magnitude smaller than that of simulated value, $\sim 10^6 W^{-1}km^{-1}$. The difference of this two values might be due to the sample structure. The CNT loaded waveguide used interaction between CNT-layer on top surface of over-cladding-less waveguide and evanescent component to work as CNT based nonlinear device. Since the evanescent wave component is small, optical power is not efficiently utilized. Therefore, nonlinear coefficient of the sample is much smaller than the simulated value.

However, considering the results in the previous section, the estimated value is too high. We used the same 10mm-long CNT-loaded waveguide sample as previous section (Section 3.3). In the subsection 3.3.4, we realized a passively modelocked fiber laser which produce femtosecond pulse trains. When the enormously high nonlinear device is inserted inside the laser cavity, nonlinear phenomenon (mainly SPM) occurrs at the device and broad spectrum will be produced. The spectrum width in Fig. 3.21(a) is normal for femtosecond-pulse lasers. Therefore, the estimation, especially the assumptions, might not be correct. We assumed the phase shifts occured purely at the sample by optical nonlinearity. However, considering the results mentioned above, we cannot assume the phase shifts of two counter propagating lights were occured purely by optical nonlinearity, SPM. They might be induced by the combination of the SPM and the other effect, the thermal effect, and also we have to take into account the effects of polarizations.

3.5 Summary of This Chapter

In this chapter, we investigated the combination of CNTs and planar waveguides fabricated by UV beam scanning. In section 3.2, basic properties, especially the optical properties, of CNTs were explained. The CNTs properties are determined solely by their chirality. Once chirality is determined, all CNTs properties can be calculated. There are two types of CNTs, semiconducting and metallic CNTs, and semiconducting CNTs absorb the light which has the same energy as bandgap. The absorption wavelength is almost inversely proportional to the CNTs diameters. For optical device applications, the absorption characteristics have been mainly focused. CNTs reveal the saturable absorption characteristics for the absorption band. CNTs have another attractive characteristics for optical device application, high optical nonlinearity. Their high optical nonlinearity can shorten the nonlinear optical processing devices.

In section 3.3, we proposed and demonstrated planar waveguide type saturable absorber based on CNTs. For future highly integrated CNT devices, planar waveguide type CNTs device is required. Since this is the first step of planar CNTs device, we demonstrated saturable absorber which had been already realized function by CNTs. To realize the planar waveguide type device, interaction between CNTs and evanescent wave component was employed. By spraying purified CNTs onto the over-cladding-less silica-based planar waveguide which was fabricated by UV beam scanning, we fabricated the waveguide-type saturable absorber samples. The samples had large polarization dependence because of their device structures. We constructed passively mode-locked fiber laser by inserting the sample as a passive mode-locker, and obtained the pulse train which had 187fs temporal width and 1.55MHz repetition rate.

Section 3.4 focused on all optical switching using CNTs. High optical nonlinearity of CNTs was used to shorten the optical nonlinear processing device length. We introduced 10mm-long CNTs loaded over cladding less planar waveguide as a nonlinear device in NOLM configuration. By using 95:5 coupler, splitting ratio contrast of about 20% was realized, and this result well matches with theory. The nonlinear coefficient (γ) of the device was estimated to be in the order of $10^6 \mathrm{W}^{-1}\mathrm{km}^{-1}$ which is two magnitude smaller

than the simulated value. However, considering the results in section 3.3 the estimated value was too high. The phase shifts might be induced by thermal effects in addition to SPM, and also we have to take into account the effects of polarizations.

Chapter 4 : Optical Tweezers for Carbon Nanotubes Deposition

4.1 Introduction to This Chapter

In previous chapter, we investigated optical applications of CNTs to introduce their distinctive features into photonics. We used spray method to deposit CNTs. However, deposited CNT layer had low uniformity and density, and efficiency of CNT use was low. Thus, handling of the CNTs is one of the largest problems for device applications. Several methods have been reported to fabricate optical devices, such as spray method [23, 24], direct synthesis method [52], and polymer embedding method [53]. These methods require complicated process and dissipate excessive amount of CNTs. Therefore, an easy and cost effective handling technique of CNTs is required. In this chapter, we propose and demonstrate an novel method to area selectively deposit CNTs onto desired position by optical tweezers.

Section 4.2 introduces the principle of optical tweezers. Optical tweezer is a technique where we can manipulate micro-, nano-objects three dimensional by focused beam.

In section 4.3, for the first time, we propose and demonstrate CNT deposition by optical tweezers with simple setup. We deposit CNTs area selectively onto core regions of optical fiber end facets using optical tweezers. This technique requires a very simple setup and consumes only a small amount of CNTs. We confirm presence of CNTs at the selected region by microscopic Raman spectroscopy. As an optical device application, we insert the CNT deposited fiber into the fiber ring laser cavity as a saturable absorber, and made a passive mode-locked fiber laser.

For precise control of CNTs deposition by optical tweezers, we require the method to obtain information of CNT layer condition during the deposition. We adopt optical reflectometry for in-situ monitoring of CNTs deposition by optical tweezers in section

4.4.

In section 4.5, we investigate fabrication of CNT super-structure, sphere shape, by optical tweezers without chemical functionalization of CNTs. CNT spheres are quite stable in the solution, and can be physically manipulated. We can deposit CNTs easily at desired position by this technique.

4.2 Principle of Optical Tweezers

Optical trapping of a micro-sized object was first proposed by Ashkin [88] and succeedingly optical tweezers using single beam was demonstrated [89]. Recent applications are not only manipulating dielectric particles but also biological and medical applications [90, 91], micro-machines [92, 93], etc. The benefits of optical tweezers compared with physical manipulation are followings [94].

- Trapping and manipulation of objects without physical contact and corrosion
- Easy release of objects by eliminating the light
- Simultaneous manipulation of multi-objects without interference [95]

There are several explanations to understand principle of optical tweezers. Here, we explain principle of optical tweezers by ray optics. Lights, or photons have momentum. A radiation force emerges for a counteraction of reflection, refraction, emission and absorption of light due to conservation of momentum. Although the radiation force emerge elsewhere, the force is negligible in common case.

Since the radiation force is the counteraction due to the conservation of momentum, the force vector direction seems to "push" an object. By focusing the light, the total direction of the force results in "pulling" the object at the focus point. Figure 4.1 shows the optical path of the light which is irradiated to the Mie object, whose size is similar to the wavelength of the light (Mie object). The object has the higher refractive index than the surrounding materials. In Fig. 4.1(a), two rays (A) are refracted twice by the object and changed their direction to be A'.

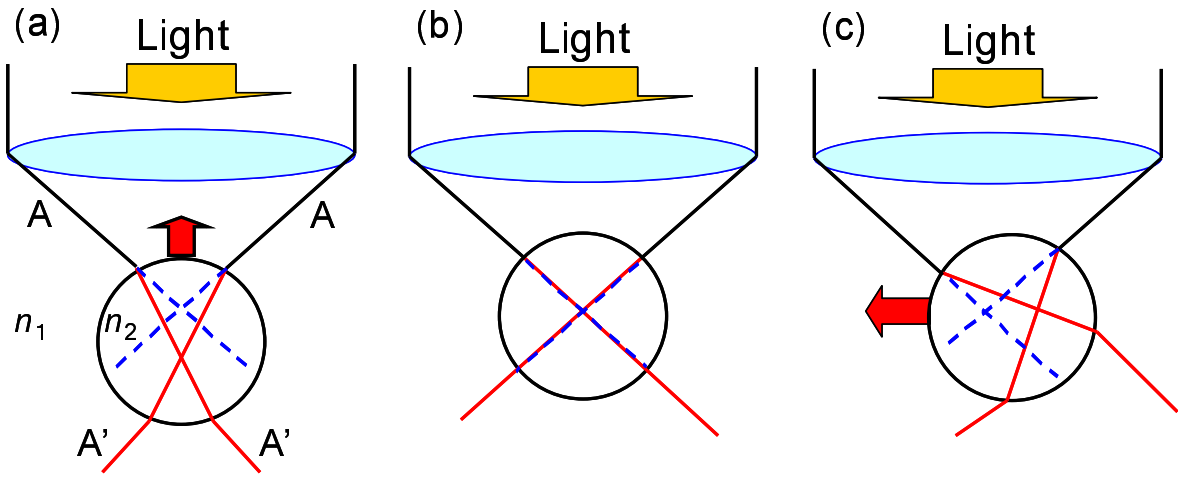

Fig. 4.1: Principle of optical tweezers (a)trapping principle (b)trapped at focused point (c) the reductive force

By integrating the optical path of all direction, the radiation force results in trapping the object toward focusing point. On the other hand, the lights have the component which reflected by the object and they emerge the pushing force to the object. Finally, the object trapped at slightly shifted point from the focusing point(Fig.4.1(b)). Even if the object moved from the trapping point by external disturbance such as thermal fluctuation, the reductive force make the object back toward the trapping point(Fig. 4.1(c)).

In above, the sizes of objects are considered as similar to or longer than the wavelength of light. Rayleigh objects whose sizes are smaller than the wavelength of light can be trapped by another principle, Lorentz force. A Rayleigh object is assumed as a single electric dipole moment in a nano-particle. The Lorentz force is formed by two forces which have different direction. One is divergence force whose direction is same with the direction of optical intensity divergence. The other is scattering force whose direction is same as the direction of optical path. Divergence force become larger than the scattering force by focusing the light with high NA lens. Thus, the Rayleigh object can be trapped at the focusing point by Lorentz force.

Generally, the objects should be transparent at the wavelength of the light and should have the higher refractive index than that of surrounding materials. The large metallic

objects are affected by large scattering force on surface of the objects and can not be trapped. When the sizes are small, scattering force becomes small and the objects can be trapped.

4.3 Area Selective Deposition of Carbon Nanotubes by Optical Tweezers for Optical Devices

4.3.1 Introduction

There is a problem in handling CNTs because CNTs tend to entangle each other and they are difficult to be dispersed in common solvents. In optical device applications, CNTs are conventionally used by spraying, directly synthesizing onto a device, or embedding into a polymer material. These processes are mostly complicated, large-scale setups are required and CNTs are not efficiently used in these methods. Incidentally, there are several methods of CNT manipulation, such as using an atomic force microscopy (AFM) tip [96], an electric field [97], a magnetic field [98], etc. Although these methods can control CNTs positions, they also needs large scale equipments. also needs large scale equipments.

In this section, we propose and demonstrate a novel technique to solve the problems of conventional techniques. Recently, three dimensional manipulation of bundled CNTs were demonstrated [99–102]. Since CNTs has high refractive index [103], focused beam trapped bundled CNTs and three dimensionally manipulated them. We employ optical tweezers to deposit CNTs selectively onto only a core region of an optical fiber end. Existence of CNTs only in selected area is confirmed by microscopic Raman spectroscopy and FE-SEM. To ensure the deposited CNTs can be utilized for optical application, a CNT deposited fiber is inserted as a saturable absorber in a fiber laser cavity. This technique will drastically improve the efficiency of CNT usage and the fabrication costs of CNT-based photonic devices.

4.3.2 Raman Spectroscopy of Carbon Nanotubes

We explain here Raman spectroscopy of CNTs. Detailed interpretations of the Raman spectrum of CNTs were reported in elsewhere [104, 105], and basics are explained here. CNTs are synthesized by various techniques, there is no technique where they can selectively synthesize CNTs which have all same chirality. Therefore, as synthesized CNT

samples are consists of several kinds of CNTs. Generally, CVD method produce broad diameter range of CNTs and laser ablation and arc discharge method give small diameter distribution. Since the samples are mixture of several kinds of CNTs, it is difficult to precisely interpret the samples. In spite of the difficulty, we have to measure CNTs for future applications of CNTs in some method, and we often use Raman spectroscopy to obtain properties of CNTs.

Figure 4.2 shows an example of Raman spectrum of CNTs sprayed onto silica-glass substrate. In the figure, the Raman spectrum of silica-glass substrate is included. Raman peaks at 500cm^{-1} and small peaks buried in other peaks at 1450 and 1500cm^{-1} are due to silica-glass substrate.

There are three main peaks in Raman spectrum of CNTs. One is the peak correspond to radial breathing mode (RBM) which appears in low wavenumber range around 200cm^{-1}. This is the most unique peak of CNTs. Its Raman shift is correspond to diameter vibration of CNTs, and the vibration frequency almost inversely proportional to the diameter (D). Generally, D[nm] $= 248/\omega_{\mathrm{R}}$cm^{-1} is reasonable value to estimate the diameter from the spectra.

Second is the G-band which appears at 1593cm^{-1} and lower wavenumber range which

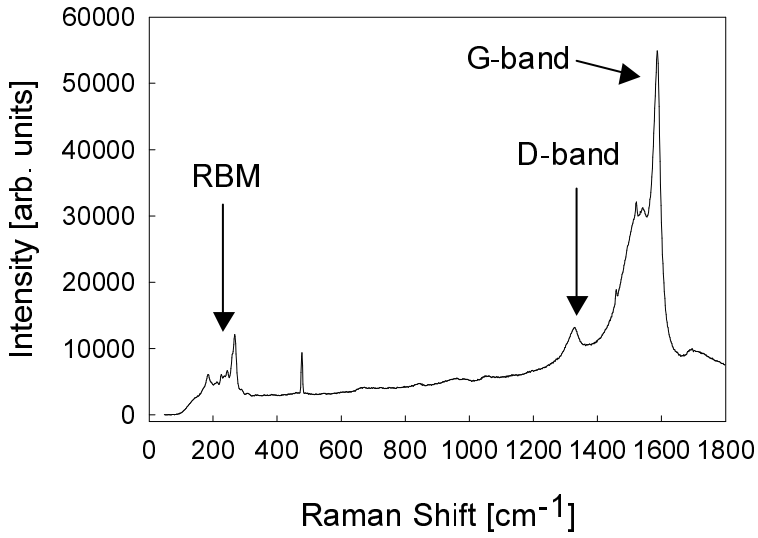

Fig. 4.2: Example of Raman Spectrum

is consisted of several peaks. G-band appears in 1584cm^{-1} for graphites, 1593cm^{-1} for CNTs and 1600cm^{-1} for amorphous carbons.

Third is the D-band which appears at 1350cm^{-1}. This peak appears when there are defects in carbon materials, such as graphites and CNTs. Therefore, we usually estimate the crystallinity of the carbon materials.

Raman spectra of CNTs are useful for analyzing CNTs, such as diameter distribution [104], temperature [106, 107], purity [108], etc. In this thesis, we perform microscopic Raman spectroscopy and confirm the existence of CNTs.

4.3.3 Experimental Results and Discussions

Figure 4.3 shows the concept of this study. Optical intensity divergence is the most important for optical tweezers. Generally, a focused spot of a light traps a dielectric objects and it is usually formed through objective lens or fiber lens. Strong confinement of light in optical fibers can produce the optical intensity divergence at the cleaved end. The light spread out from the cleaved end of an optical fiber has a light intensity profile very similar to that in the focused spot as shown in Fig. 4.3. In this case, the trapping point is at the end facet of optical fiber core region. When the light which

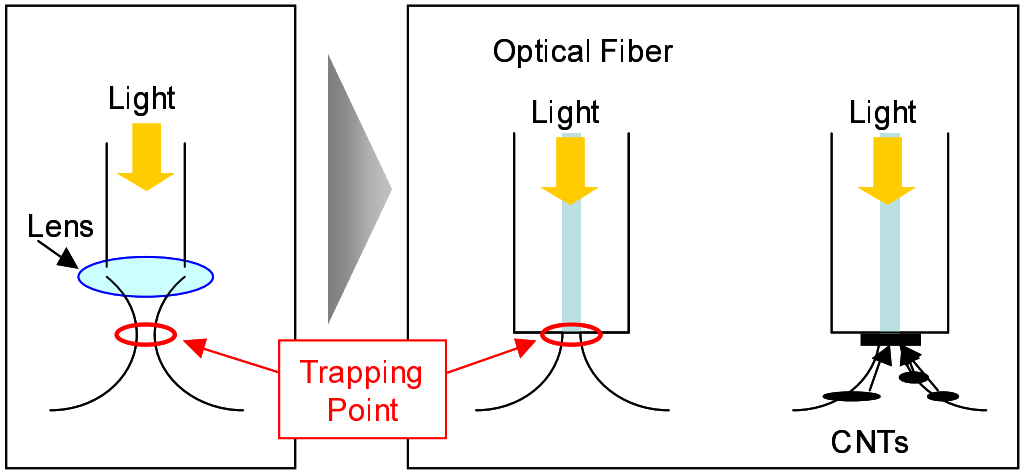

Fig. 4.3: Concept of area selective deposition to fiber end facets

has appropriately controlled intensity is injected through a fiber into CNTs dispersed solution, CNT particles are expected to be trapped by optical tweezers, and deposited onto the end facet of the optical fiber.

Our experimental setup is very simple as shown in Fig. 4.4. It is composed of just two equipments, a laser diode and an EDFA. We prepared the CNTs dispersed DMF solution by the purification procedure which was mentioned in chapter 3.

Light produced from a laser diode which has the wavelength of 1560nm and the optical power of ∼10dBm is amplified by a high-power EDFA. The light is incident into CNT dispersed DMF solution through a perpendicularly cleaved fiber end facet. The divergence of optical intensity traps the CNTs by optical tweezer effect and deposits them onto the fiber end. We observed CNTs deposition conditions on the fiber end facets using a microscope for several different optical powers. Microscopic Raman spectroscopy was used to confirm existence of CNTs at the selective area. To find the dependence of numerical aperture(NA) of optical fiber, we used two types of optical fibers having different NAs, SMF and dispersion shifted fiber(DSF).

In Fig. 4.5, microscopic images and Raman spectra of CNTs deposited fiber ends of standard SMFs are shown. Fig. 4.5(a),(b),(c) correspond to incident optical power of 20dBm, 21.5dBm and 22.0dBm, respectively. Red circles in Fig. 4.5(a1), (b1), (c1) indicate core are of SMF, and corresponding Raman spectra are shown with red curves in Fig. 4.5(a2), (b2), (c2). Blue circles are the areas where CNTs are deposited outside of the core, and corresponding Raman spectra are shown with blue broken curves.

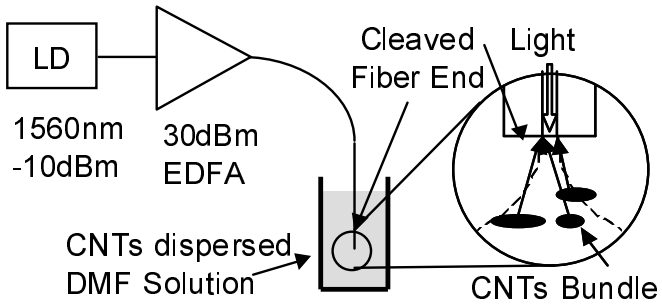

Fig. 4.4: Schematics of experimental setup for CNTs deposition by optical tweezers to a fiber end

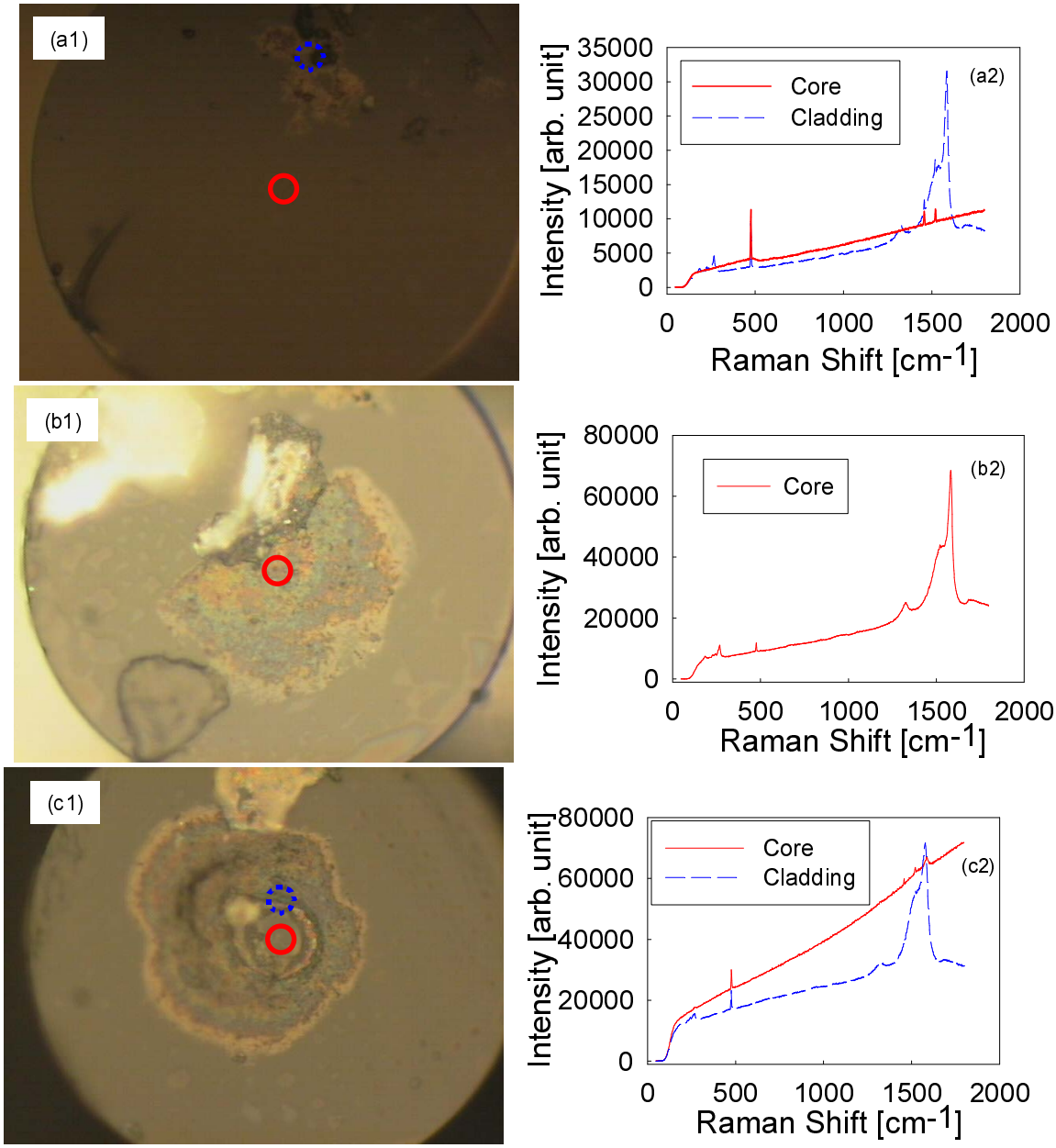

Fig. 4.5: Microscope image and Raman spectra of deposited CNTs onto fiber ends by optical tweezers (a)20.0dBm (b)21.5dBm (c)22.0dBm

Most typical Raman spectrum of CNTs is the peak around 250cm^{-1} which is due to RBM which explained in subsection 4.3.2. We confirmed the presence of CNTs by the peak. Optical power of 20.0 dBm was not enough to trap the CNTs, whereas Fig. 4.54(a) shows the existence of CNTs which might happen to be attached to the cladding region of the fiber end. In Fig.4.5(b), CNTs were area-selectively deposited onto the fiber end only around the core region, and Raman spectrum shows the existence of CNTs. By increasing the optical power up to 22.0 dBm, CNTs were not deposited onto core region but deposited around the core-cladding boundary. It is probably because the radiation force by photon at the core center was too strong to gather CNTs. The radiation force at the cladding region was weaker than the core region, and CNTs were deposited onto outside from the core-cladding boundary.

To ensure the area selective deposition of CNTs onto fiber end, FE-SEM image was taken by JEOL JSM-7000F. Figure 4.6 shows the FE-SEM image of fiber end onto which CNTs were deposited onto the fiber end by optical intensity of 22.0dBm so that CNTs deposited onto outside core-cladding. Figure 4.6(a) shows the area selective deposition of CNTs just around the fiber core. CNTs do not exist on the core in the magnified image (Fig. 4.6(b)). From Fig. 4.6(c), the clear boundary which separate the two areas with and without CNTs.

Thus, we successfully deposited CNTs onto the core region of the fiber end facet. However, we find that we had to control the optical power precisely. Margin of optical power to deposit CNTs onto the core region was very narrow, about $\pm$ 1dB around 21.5dBm. It is because the NA of SMF is so small that the trapping point was not confined. When we use fibers with high NA, the margin will be wider and required optical power will be small.

To widen the margin of optical power, we used DSF which has higher NA than SMF. We deposited the CNTs onto the DSF end facet with optical intensity of 19.0dBm. Fig.4.7 shows the microscope image of the fiber end facet and its Raman spectrum at the core center. Strong confinement of a light reduced the required optical power for CNT deposition by 2.5dB, and widened the margin to be $\pm$ 2dB.

We used bare fibers in previous experiments. To reduce the alignment cost after

CNT deposition, we deposited CNTs onto a fiber ferrule end as shown in Fig. 4.8. We deposited CNTs onto an end facet of standard SMF with fiber ferrule by optical intensity of 21.5dBm, as same experimental condition as the fiber which is shown in Fig.4.5(b). Raman spectra shows that CNTs were area selectively deposited onto only the core region. The fiber can be used as an alignment-free CNT device.

As an optical application of the CNT deposited fiber by optical tweezers, we demonstrate a passively mode-locked fiber laser which employs the fiber as a saturable absorber. The experimental setup is shown in Fig.4.9. An EDFA was used as the laser gain medium and an isolator was inserted to prevent back reflection in the cavity to ensure the one-directional lasing. We controlled the polarization state by a PC. The total dispersion in the laser cavity was adjusted to be nearly zero by inserting a 20m-long SMF. The output light came out from a 3dB coupler. CNT-deposited fiber ferrule was inserted as an alignment-free passive mode-locker. Insertion loss of the fiber was about 4.2dB. We measured the optical spectrum by an optical spectrum analyzer and the autocorrelation trace by a SHG autocorrelator. Resolutions of OSA and SHG autocorrelator were 0.1nm and 50fs, respectively.

By controlling the polarization state inside the laser cavity, pulsed output is successfully realized. Figure 4.10 shows the properties of optical output of passively mode-locked fiber ring laser using CNTs deposited fiber by optical tweezers. The 3 dB spectral width is 3.2nm and measured SHG autocorrelation trace had the FWHM width of 630fs. When transform limited sech^2 pulse waveform is assumed, pulse width is calculated to be 400fs.

CNTs were successfully deposited onto fiber end by optical tweezers and the fiber could be used as nonlinear optical device, saturable absorber. This technique allows us to solve the some problems of handling CNTs such as area selective deposition and efficient use of CNTs. CNT deposition by optical tweezers is useful technique especially for optical device fabrication because CNTs were gathered to an optical path by the light which propagates along the optical path. In next section, we propose a technique to realize accurate control of CNT deposition by optical tweezers.

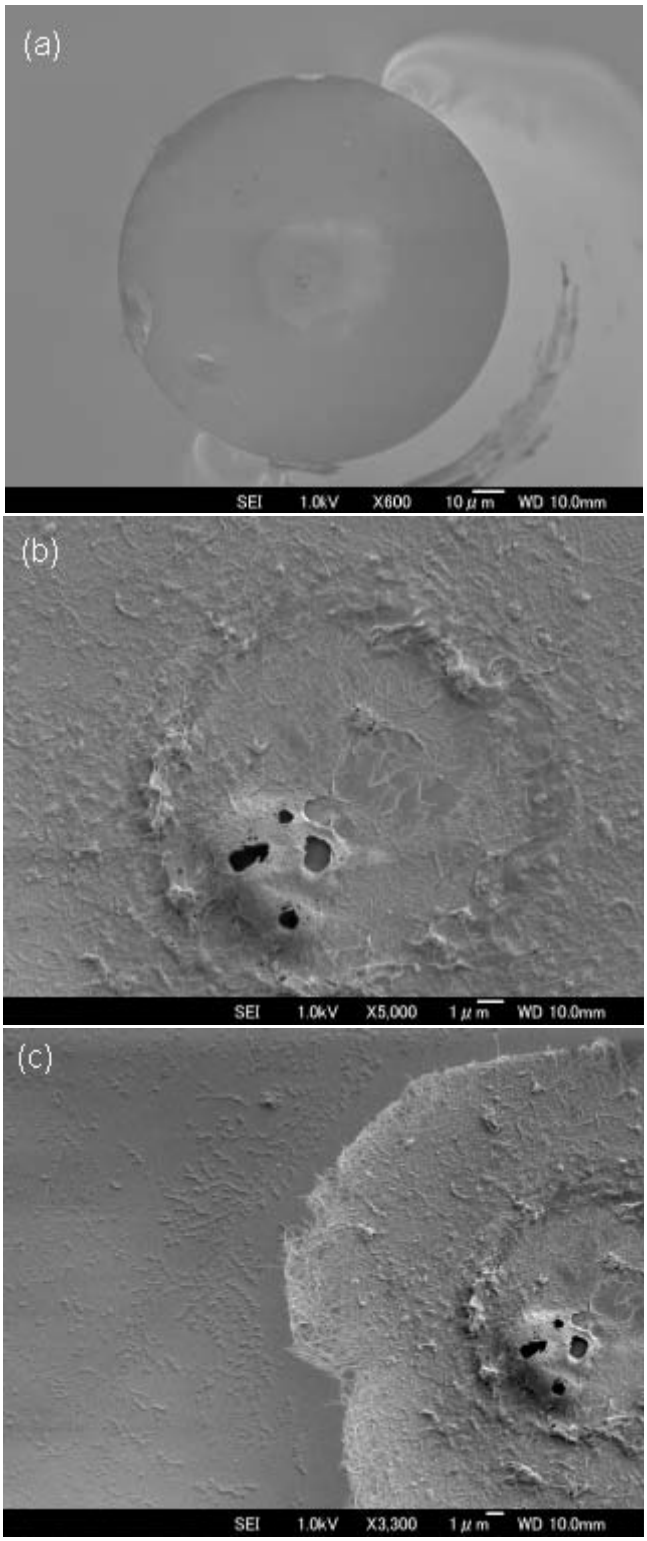

Fig. 4.6: FE-SEM image of SMF end onto which CNTs were deposited core-cladding boundary (a) Whole Fiber End Image (b) Magnified around Core (c) Magnified around Core-Cladding Boundary

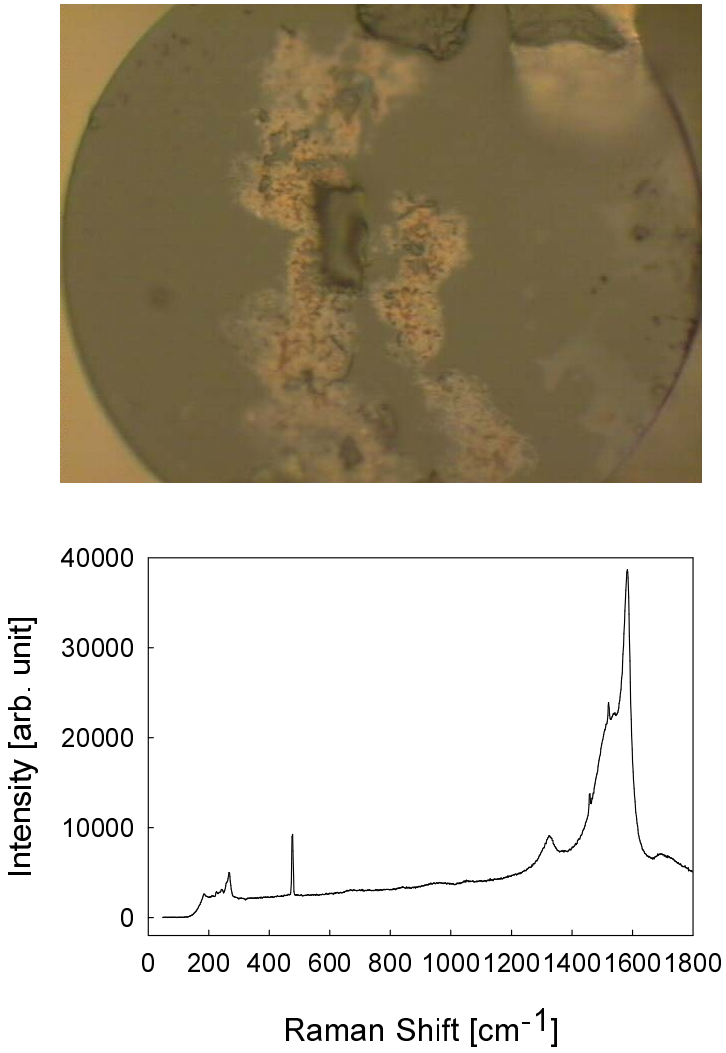

Fig. 4.7: Microscope image and Raman spectra of deposited CNTs onto fiber ends by optical tweezers using a DSF fiber by 19.0dBm

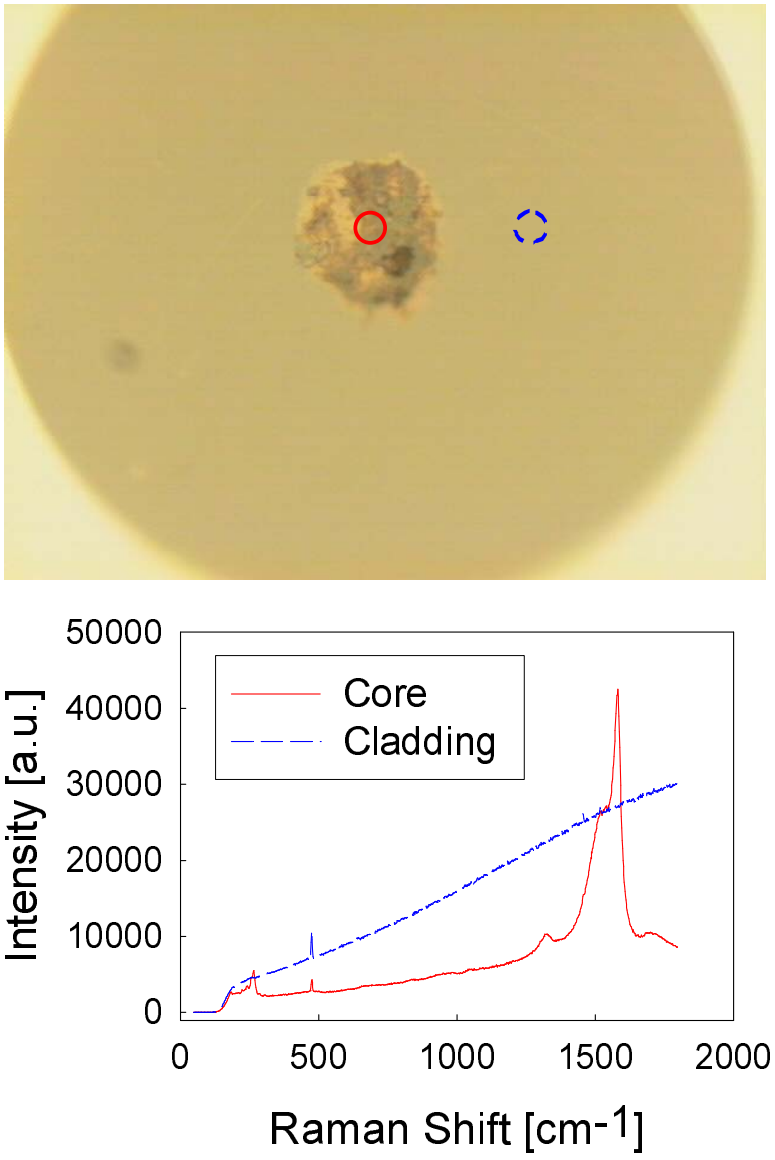

Fig. 4.8: Microscope image and Raman spectra of deposited CNTs onto SMF end with ferrule by optical tweezers

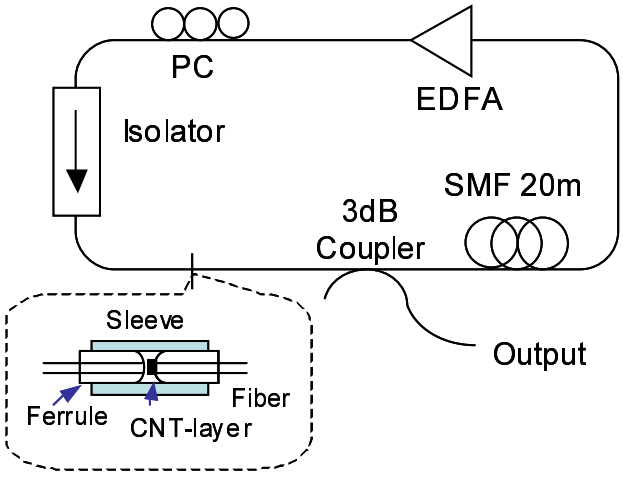

Fig. 4.9: Experimental setup for passively mode-locked fiber laser using CNTs deposited fiber by optical tweezers

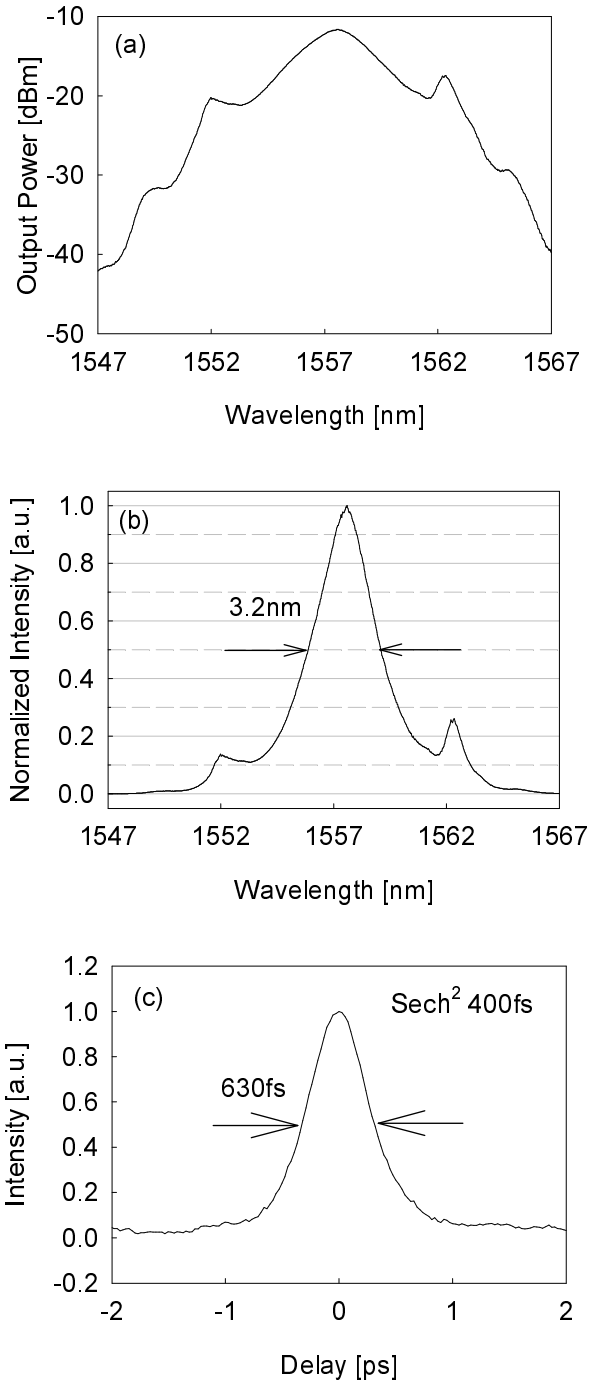

Fig. 4.10: Passively mode-locked fiber laser output (a) Optical Spectrum (Logarithm, 0.1nm Resolution) (b) Optical Spectrum (Linear, 0.1nm Resolution (c) Autocorrelation Trace

4.4 Optical Reflectometry for In-situ Monitoring of Carbon Nanotubes Deposition

4.4.1 Introduction

In previous section, we employed optical tweezers for CNTs deposition, and demonstrated area selective deposition of CNTs to fiber ends. However, it is difficult to monitor and control the condition of CNT layer which is deposited by the technique. Since we deposit CNTs which happen to float in front of fiber end, we cannot determine starting time of deposition. For precise control of CNT layer conditions, such as thickness and uniformity, a technique to monitor CNT deposited layer condition during the deposition is required.

Optical sensing is the one of the most important method to measure the properties of an object during the fabrication process. There are many kinds of optical sensing, optical reflectometry, optical spectroscopy, Raman spectroscopy, optical tomography, etc. Non-contacting and non-corrosive sensing can be made by optical sensing and its suitable for monitoring device fabrication processes, such as semiconductor devices and also CNTs [109]. In this section, we propose and demonstrate an optical reflectometry for in-situ monitoring of CNT deposition by optical tweezers.

4.4.2 Experimental Results and Discussions

Optical reflectometry is a technique to measure the reflection from the object. Reflectivity data gives us the information of the object. By measuring the time trace of reflectivity from the fiber end which is dipped into the solution, CNT attachment starting can be detected because of scattering and reflection once CNTs attached. Attachment of small entanglement of CNTs causes scattering, and when large number of CNT entanglements are attached and form a layer is occurred at the boundary Fresnel reflection. Fortunately, the refractive indexes of silica-glass which is material of optical fiber and DMF are approximately 1.46 and 1.42, respectively, and the Fresnel reflection at the boundary of optical fiber and DMF is suppressed to be low. In simulation, the refractive indexes of CNTs is around 3.0 [103], and the large refractive index difference

between optical fibers and CNTs causes high reflection. Therefore, attachment of CNTs can be detected by measuring time trace of reflectivity.

Figure 4.11 shows the schematics of experimental setup. The light from a laser diode is used for both optical tweezers and optical reflectometry. The light at the wavelength of 1560nm was amplified by a high-power EDFA, and 10% was split and attenuated by 20dB to monitor the input power. 90% of light was incident from the cleaved fiber end into DMF solution, where purified CNTs were dispersed. The Fiber end serves as the focused spot for optical tweezers, and CNTs bundles were deposited onto the fiber end as shown in Fig. 4.11. The power of reflected light from the fiber end was measured by another power meter through a circulator. Input and reflected powers were measured at every 500ms. After the deposition, DMF was dried up, and FE-SEM image of the fiber end was taken. We deposited thick and thin CNT layer onto fiber ends by simply changing the deposition time.

Figures 4.12 and 4.13 show the in-situ reflectometry data series and FE-SEM images of low- and high-density deposition, respectively. The EDFA was off at first, and once it was turned on, the gain was kept constant. Reflectivity was small around -40dB before CNT deposition. When CNTs are deposited onto the fiber end, reflectivity is expected to drastically increase. It takes a short period of time (10-100s) to start deposition and the period is not definite because CNTs are not dispersed uniformly in the solution. When a CNTs bundle happens to come close to the core of fiber end, the bundle is

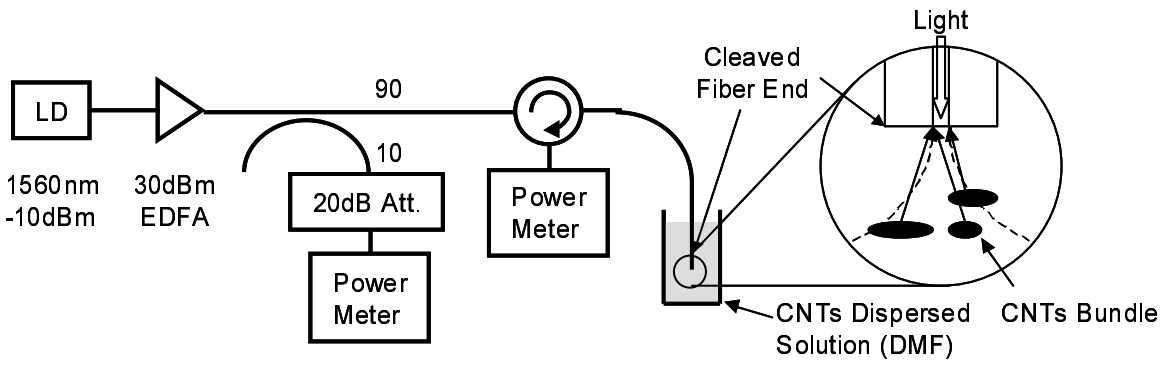

Fig. 4.11: Schematics of Reflectometry for monitoring CNTs

trapped and deposited. Once a single CNT bundle is deposited, it becomes a seed of deposition, and it entangles the other bundles to start the deposition process. Figures 4.12(a) and 4.13(a) clearly indicate the drastic increase of reflectivity due to the CNT deposition as expected. The deposited CNTs do not form uniform layer at first, and the reflectivity fluctuated due to the non-uniformity and the flow of DMF. For low-density deposition, the EDFA was turned off at 8 seconds after the start of deposition (Fig. 4.12(a)). For high-density deposition, the EDFA remained on for about 4 minutes. During the deposition, fluctuation of reflectivity becomes smaller(Fig. 4.13(a)). It indicates that the CNTs-layer becomes more uniform as the layer becomes thicker. The above observations through the reflectometry were supported by the FE-SEM images, where a thin CNT layer was clearly observed only at the core region in Fig. 4.12(b)(c), whereas the deposited layer is very thick in Fig. 4.13(b)(c). From the magnified image (Fig. 4.12(c) and 4.13(c)), area selective deposition was confirmed. Circular like area deposition is realized by optical tweezers and their diameter was around 15μm.

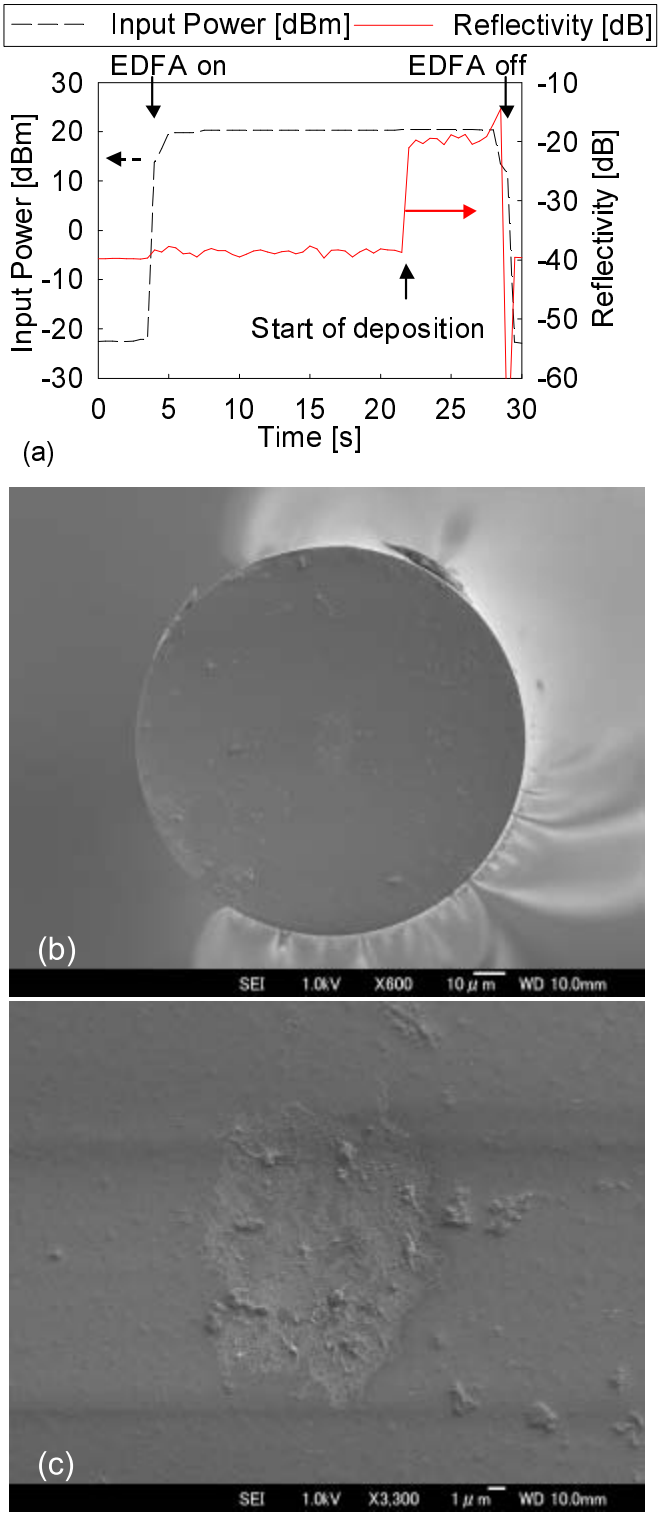

Fig. 4.12: Thin CNT layer deposition by optical tweezers with monitoring (a) In-situ reflectometry (b) FE-SEM image of fiber end (Low Magnitude) (c) FE-SEM image of fiber end (High Magnitude)

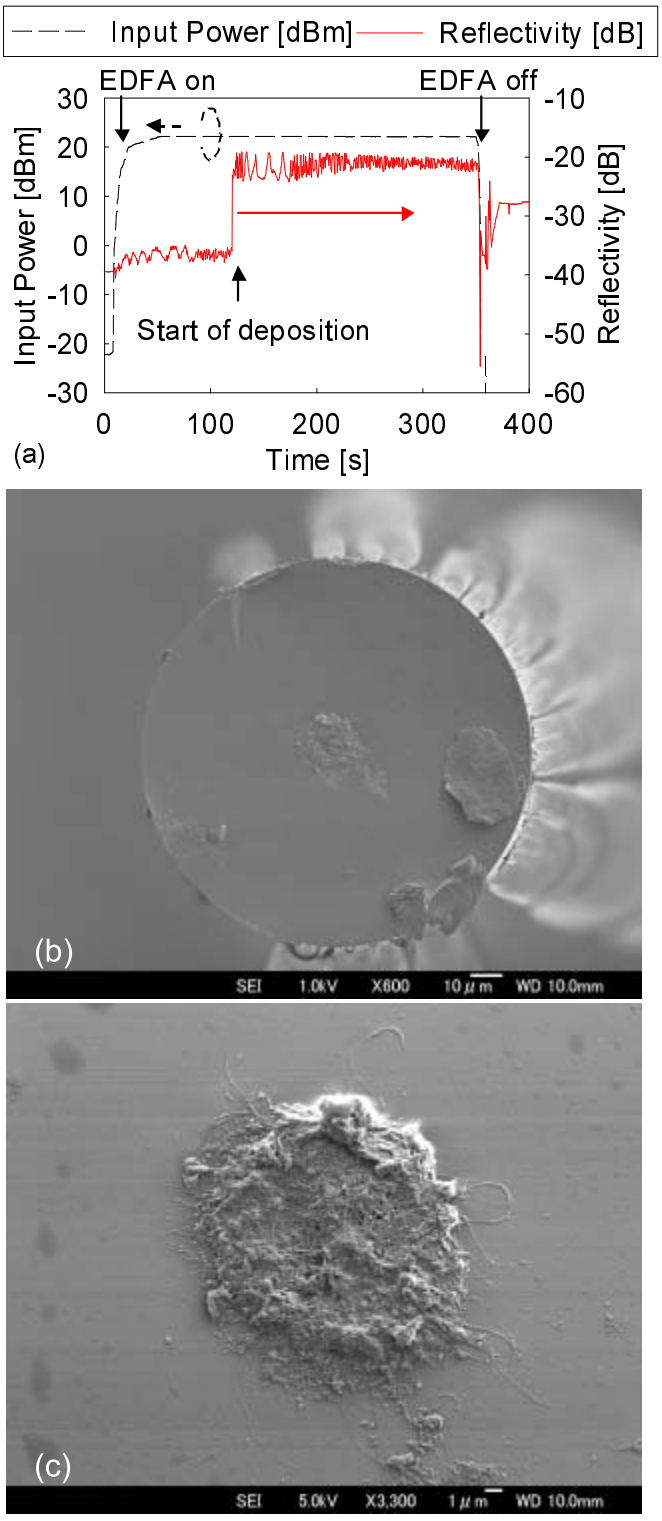

Fig. 4.13: Thick CNT layer deposition by optical tweezers with monitoring (a) In-situ reflectometry (b) FE-SEM image of fiber end (Low Magnitude) (c) FE-SEM image of fiber end (High Magnitude)

4.5 Fabrication of Carbon Nanotube Sphere

4.5.1 Introduction

Easy handling of CNTs the main topic in this chapter. Even if the CNTs are deposited onto fiber ends by optical tweezers, it is not enough cost effective for industry use compared with other materials which can be handled with macroscopic manipulation. Super-structures of CNTs have many applications, such as hydrogen storage materials [110, 111]. Constructing the super structures made of CNTs which we can manipulate physically is one of the important tasks. Up to now, CNT based super structures have been demonstrated in ring-shape, star-shape and sphere shaped cage [112–114], etc. Difficulty in formation of super structures made of CNTs is their large van del Waals force interaction with each other. The force makes it difficult to disperse CNTs into common solvents because of spontaneous aggregation and fabrication of super-structurer has many problems. Conventional techniques to fabricate the super-structures utilize templates of super-structures and chemical functionalization of CNTs. In this section, we investigate fabrication of sphere shaped super-structures made of CNTs by optical tweezers without chemical functionalizations.

4.5.2 Experimental Results and Discussions

The experimental setup which is used in this section is illustrated in Fig. 4.14. There is no special difference between experimental setups which were used in this section and those in previous setups (Fig. 4.4, Fig. 4.11). The differences between previous sections are microscope which is used for observing fiber end. In previous sections, fiber end was dipped into DMF solution and fiber end was faced downward. In this section, we fixed a fiber end on a slide glass, and dropped DMF solution droplets. Another difference of experimental condition is a condition of CNT solution. The sizes of entangled CNTs in DMF solution were smaller than previous sections. Since CNT entanglement size is small, higher optical intensity is required compared with previous sections. It had been already confirmed that formation of sphere cannot be observed only with DMF without

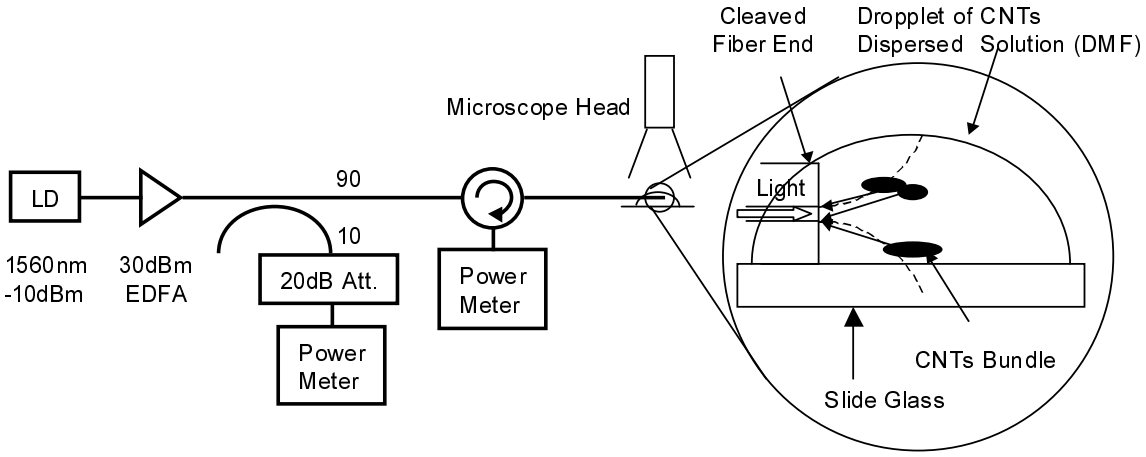

Fig. 4.14: Experimental Setup for Formation of CNT Sphere

CNTs.

Figure 4.15 shows a fiber end and a CNT sphere which was fabricated by the light at the wavelength of 1560nm which had 25.0dBm intensity. The diameter of optical fiber is 125μm, and the diameter of CNT sphere was estimated to be around 20μm. The diameter of CNT sphere could be controlled by changing injected optical intensity and time period. Figure 4.16 shows a growing process of a CNT sphere along time. The injected optical intensity was constant at 28.0dBm. First, a small sphere was formed (Fig. 4.16(a)), and it became larger and larger and finally its diameter reached around 100μm(Fig.4.16(b)$\sim$(h)).

Large sphere could be formed by high optical intensity and injecting a light for a long time. However, by high optical intensity, optical radiation force was too large and broke the sphere. The reflection and refraction of light by large CNT sphere prevent stable sphere growing. We fabricated large CNT sphere by precise control of optical intensity as shown in Fig. 4.17. Its diameter exceeded the diameter of an optical fiber and reaches 200μm. Increasing rate of optical intensity was controlled with monitoring the sphere stability with microscope, and final injected optical intensity was 29dBm. By high increasing rate of optical intensity, the formed sphere was relatively unstable.

Only from the Figs. 4.15, 4.16 and 4.17, sphere shape could not be confirmed. Figure 4.18 shows the succeeding images of rotating an optical fiber with a CNT sphere. We

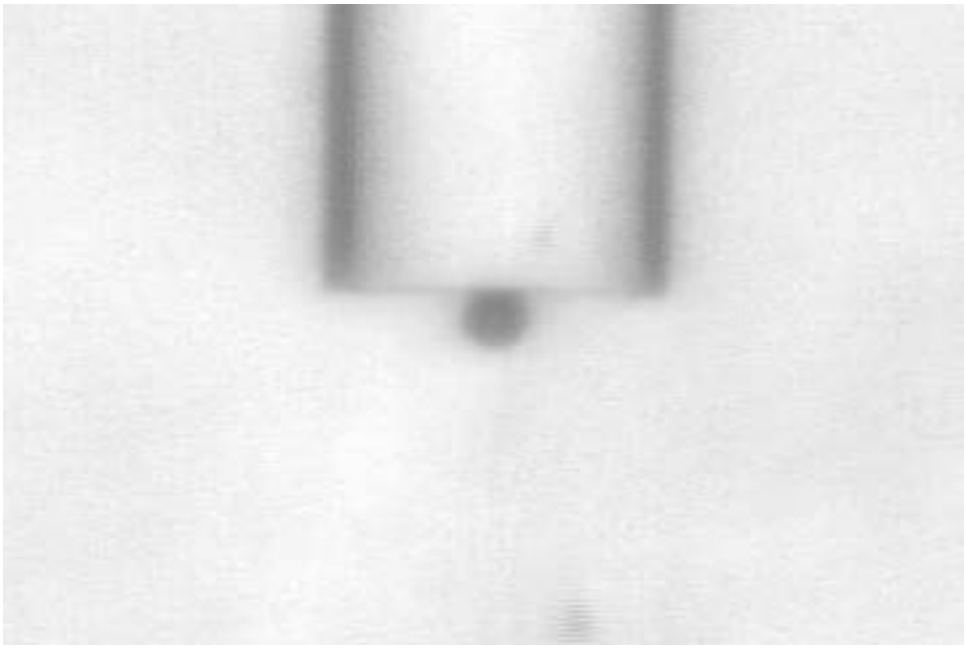

Fig. 4.15: Formation of CNT sphere

confirmed the super-structures have the sphere shape structures.

Small spheres whose diameters were smaller than 15μm were relatively unstable. On the other hand, large spheres which have larger diameter than 15μm are quite stable. Those stable spheres can be manipulated macroscopically (Fig. 4.19). A sphere formed on the fiber end was detached from the fiber with another fiber, and attached to the side of another fiber. The adsorption force was quite strong and the sphere did not detached spontaneously. The spheres had the elasticity and even if a sphere is compressed, the shape became sphere shape by releasing force for compression (Fig. 4.20).

The spheres which had low stability collapsed gradually as shown in Fig. 4.21. The initial diameter of the sphere was about 50μm. The sphere shown in Fig. 4.21 had been gradually collapsed and became smaller.

Although the spheres were stable in DMF, we could not take out CNT sphere from DMF solution in sphere shape. It was difficult to maintain the shape when the object pass through the liquid and air boundary and collapsed at the boundary. We could not measure what the spheres were consisted of, because it was difficult to take Raman spectrum or SEM image since the objects were in liquid. To confirm that CNTs were

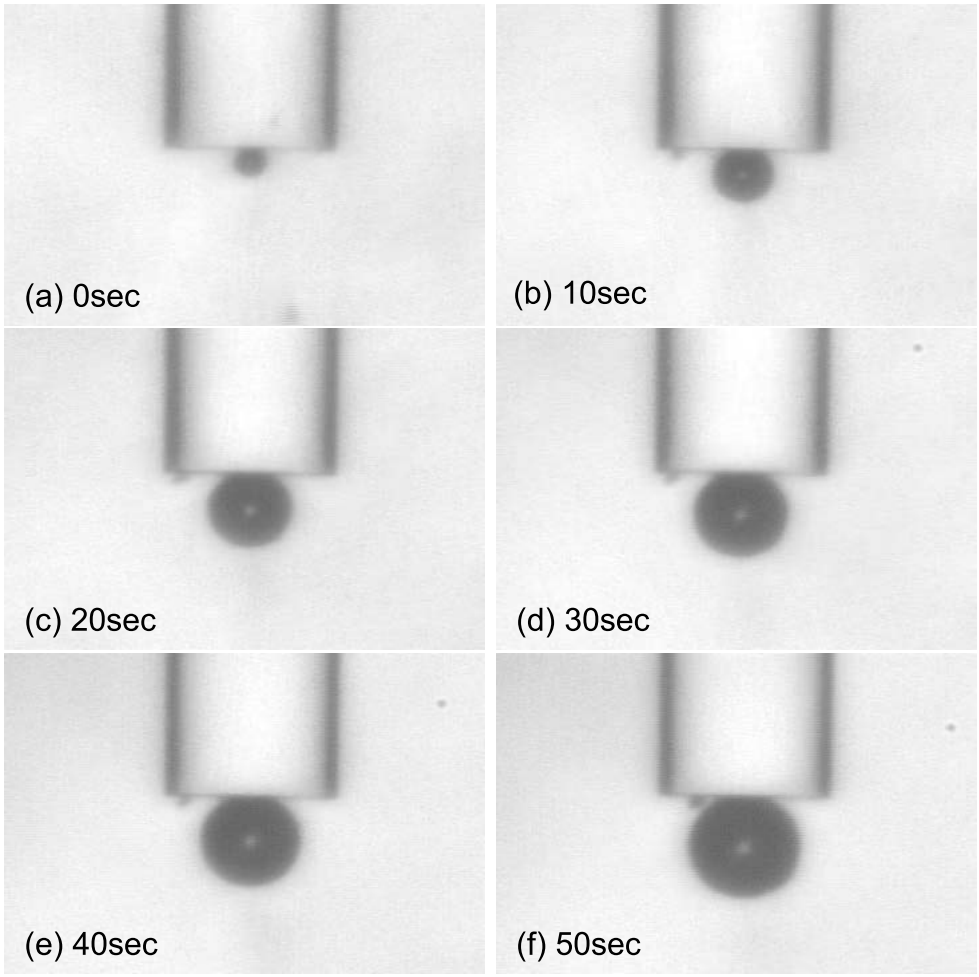

Fig. 4.16: Growing of CNT sphere (a)0sec (b)10sec (c)20sec (d)30sec (e)40sec (f)50sec

included inside the spheres, we inserted a CNT sphere into fiber ring laser cavity as saturable absorber. Passive mode-locking would not occur, if CNTs were not included in the sphere.

Figure 4.23 shows the experimental setup for passively mode-locked fiber ring laser using CNT sphere. A small CNT sphere was inserted into fiber ring laser cavity between the gap of two fiber ends. The gap was around 5μm, and was immersed in a CNT dispersed DMF droplet. An EDFA was used as a laser gain medium and an isolator was inserted to prevent back reflection in the cavity. We controlled the polarization state inside the ring cavity by a PC. The SMF was used to control the total dispersion in the ring cavity to be nearly zero. The output light came out from 3dB coupler and optical

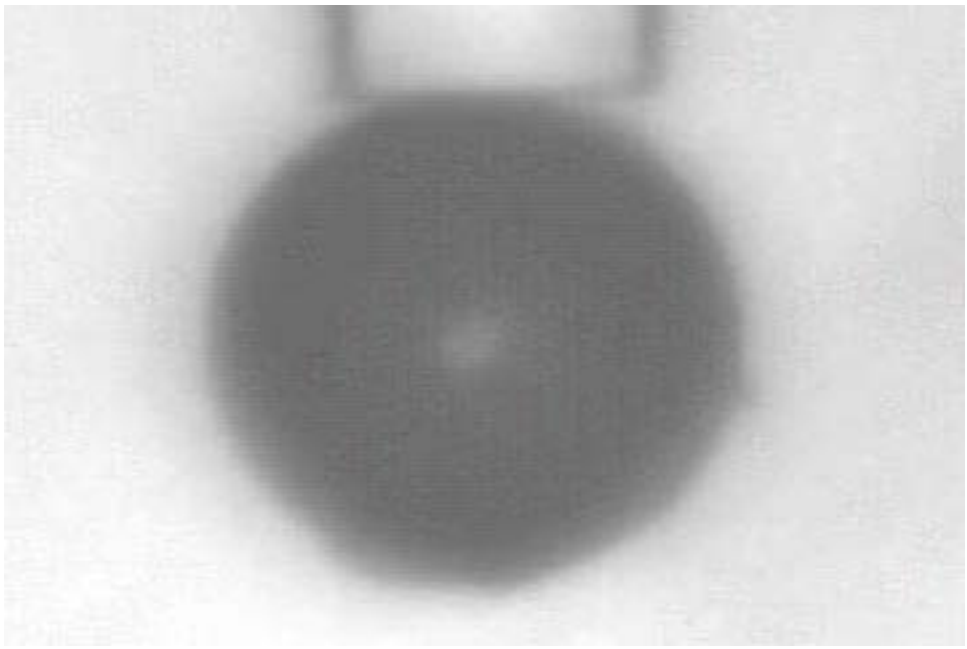

Fig. 4.17: Formation of CNT large sphere

spectrum was measured by OSA. Resolution of OSA was 0.1nm.

The gain of the EDFA was controlled to form a small CNT sphere. Once a small sphere was formed, optical path between the fiber gap changed. Therefore, the fiber alignment was slightly changed after the formation. Figure 4.23 shows the gap of two fibers with a small sphere. We obtained broad lasing spectrum which is the feature of pulsed laser as shown in Fig. 4.24. However, the oscillation was not stable enough to measure SHG autocorrelation trace. It is because the pulse inside the cavity has high peak power, and disturb the stability CNT sphere. Although stable pulsed output could not be maintained, we confirmed CNT existence in the sphere by this result.

Most probable mechanism of CNT sphere formation is that micro bubbles adsorbed the CNTs around their surface(Fig. 4.25). CNTs attached to a fiber end was heated by the high intensity laser light and evaporate DMF solution. Evaporated DMF formed a sphere shaped micro bubbles. Micro bubbles in a liquid tends to adsorb the small particles like CNTs to their surface. CNTs which were floated in DMF solution were gathered and deposited on the micro bubbles, and the sphere shaped super structure would be formed.

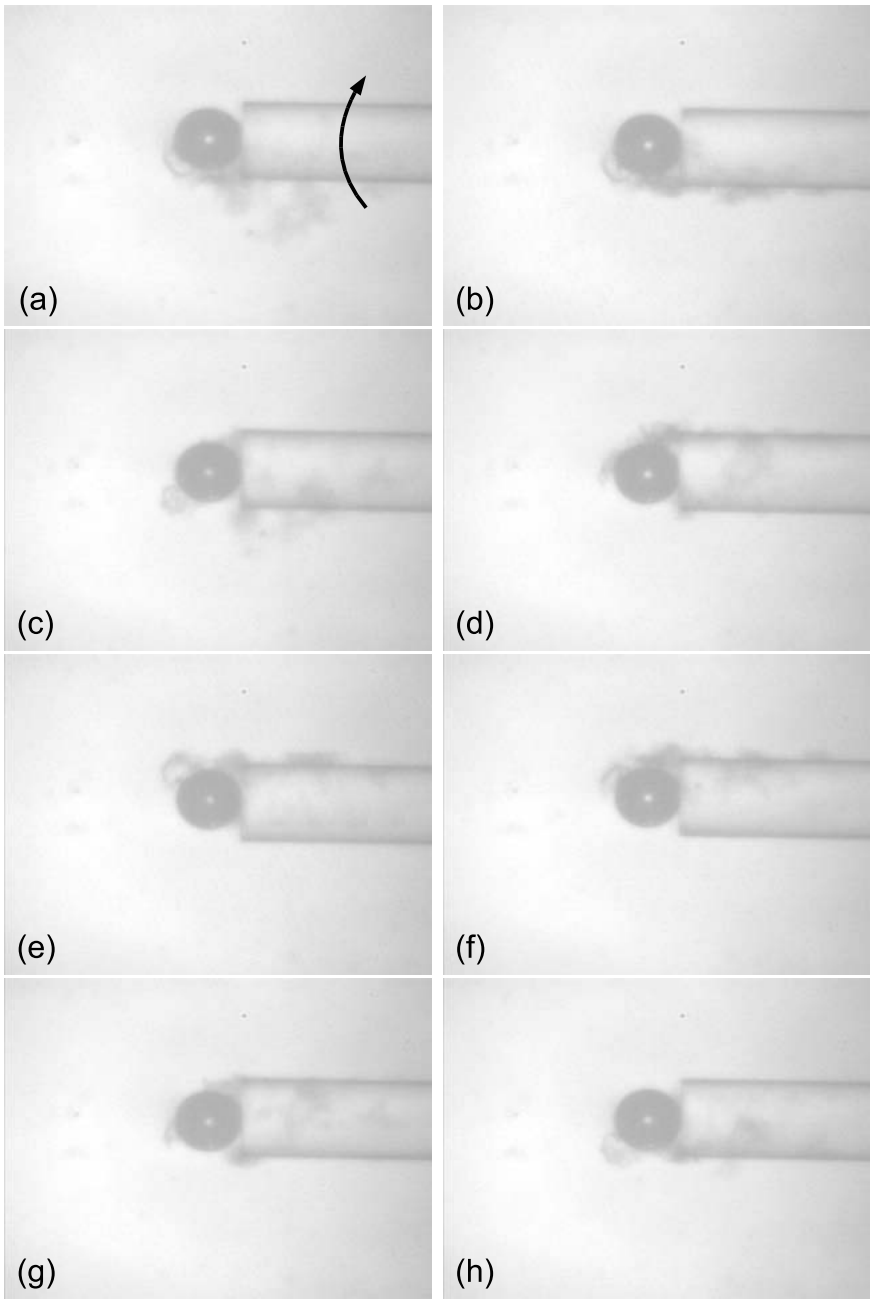

Fig. 4.18: Rotation of CNT sphere

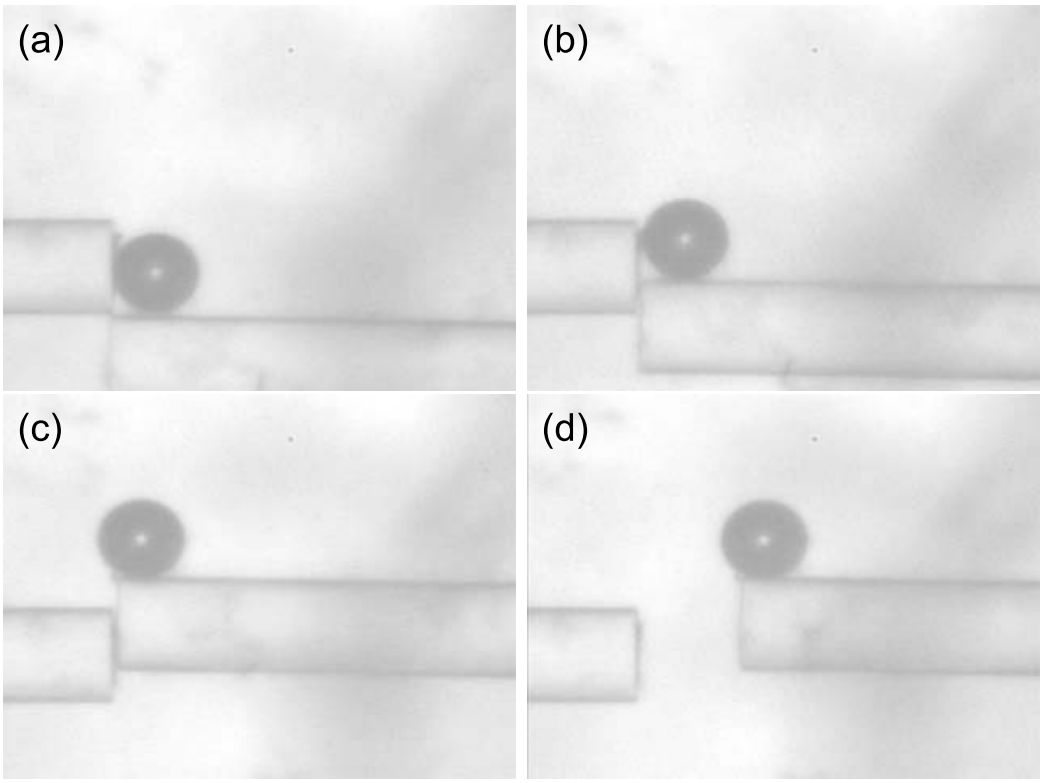

Fig. 4.19: Physical manipulation of CNT sphere

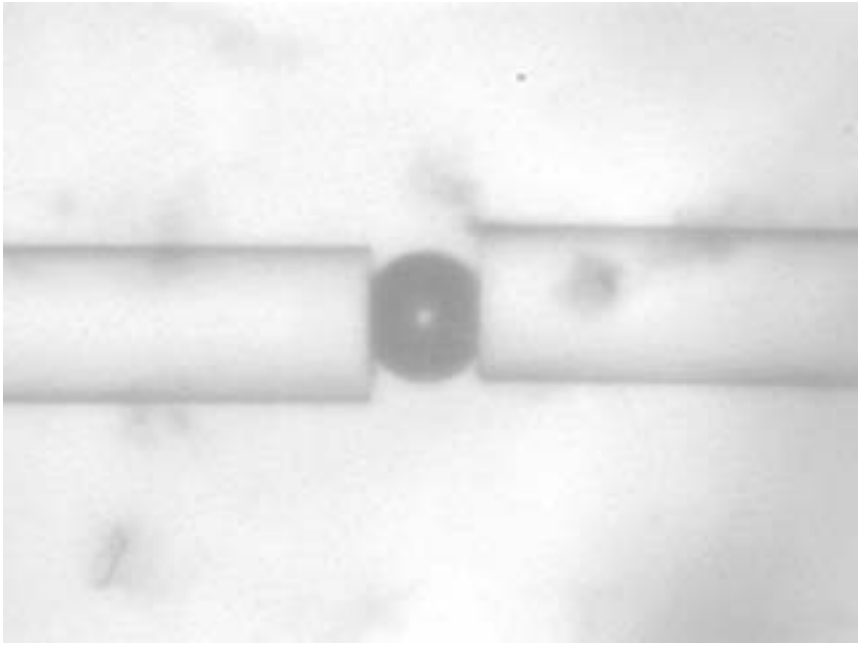

Fig. 4.20: Elasticity of CNT Sphere

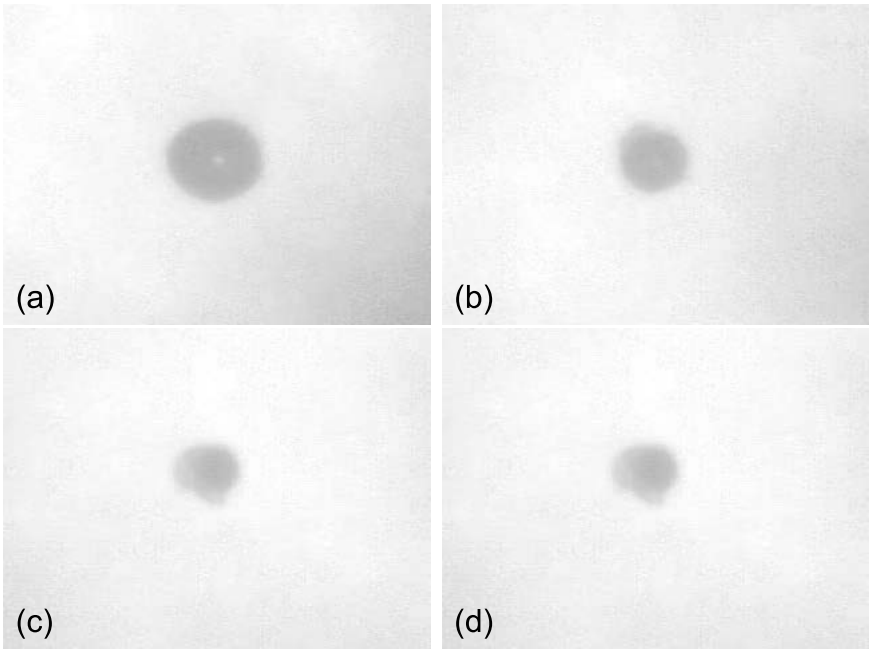

Fig. 4.21: Collapsing of CNT sphere

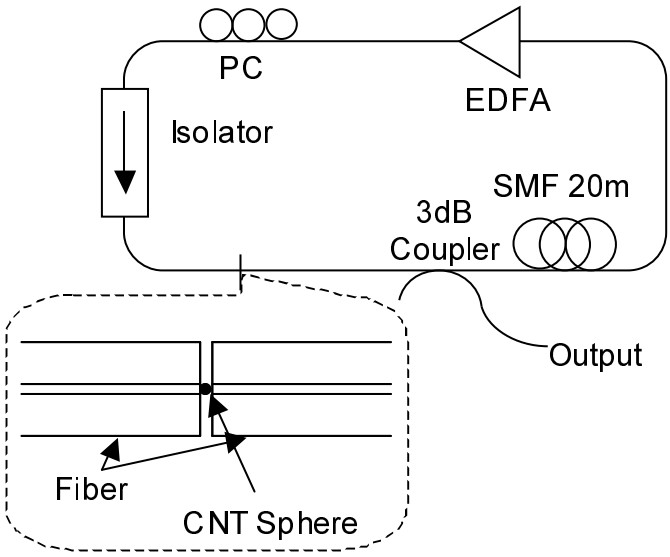

Fig. 4.22: Experimental setup for passively mode-locked fiber ring laser Using CNT sphere

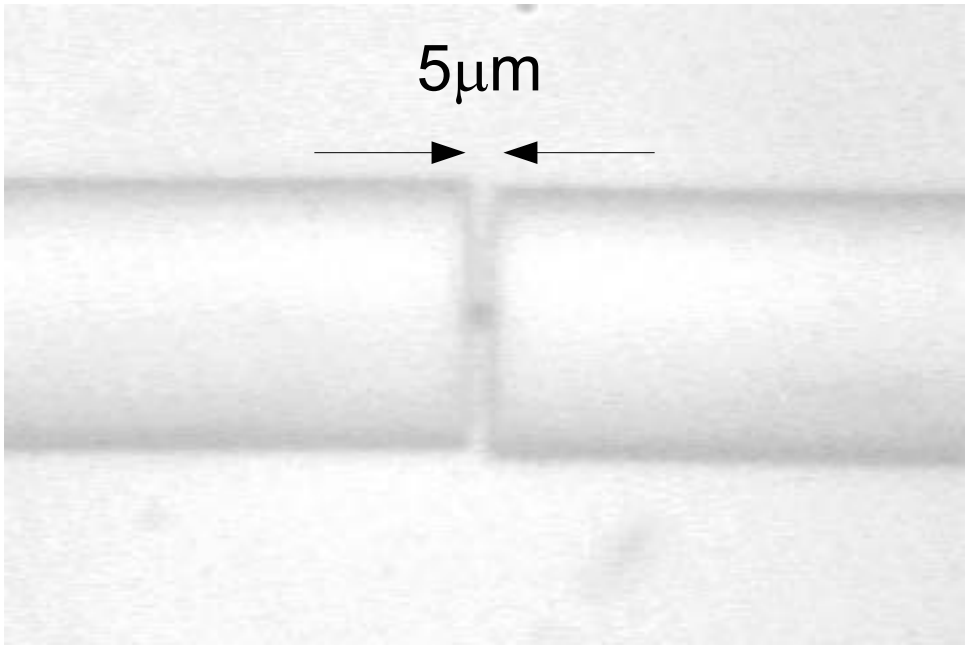

Fig. 4.23: CNT sphere for passively mode-locked laser (approximately 5μm diameter)

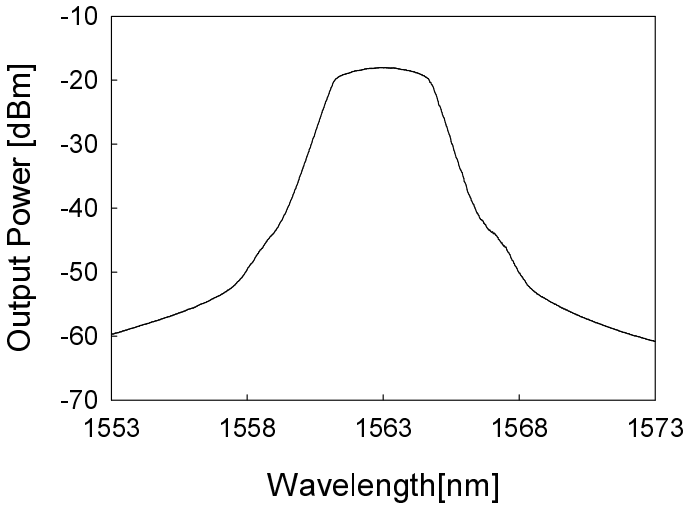

Fig. 4.24: Optical spectrum of passively mode-locked laser using CNT sphere

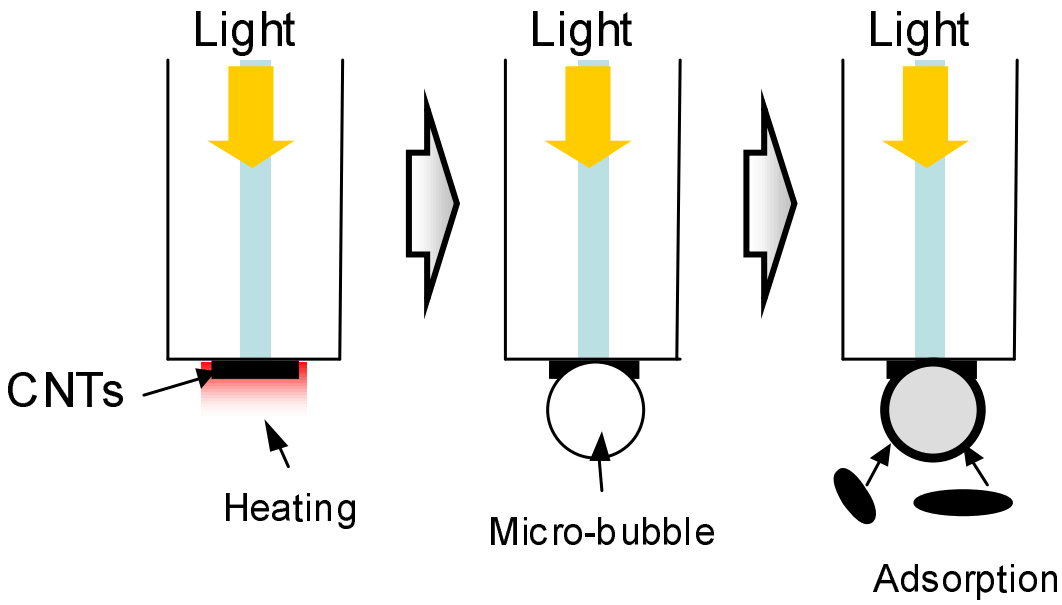

Fig. 4.25: Mechanism of CNT sphere formation

4.6 Summary of This Chapter

In this chapter, optical tweezers was employed to solve a handling problem of CNTs for many applications. In section 4.2, the principle of optical tweezers was explained using simple ray optics. Optical radiation force which "push" an object will change into the force which "pull" or "trap" the object by focusing the light. Large divergence of optical intensity can trap the micro-, nano- materials at focusing point.

In section 4.3, we proposed and demonstrated the deposition of CNTs onto optical fiber by optical tweezers. The light spreads out from the optical fiber end was used as an optical intensity divergence for optical tweezers. The experimental setup was very simple, composed only of a laser diode and an EDFA. We successfully deposited the CNTs onto the fiber end by injecting the light into CNT dispersed solution through a perpendicularly cleaved fiber end. Microscopic Raman spectroscopy proved the area selective CNT deposition only around the core region. Optimum optical intensity was found to be 21.5dBm for SMF, and 19.0dBm for DSF. The optimum intensity highly depends on the NA of the fibers and the condition of CNT dispersion. We also demonstrated a passively mode-locked fiber laser using a fiber whose one end was coated by CNTs with our technique. We generated short pulses with a temporal pulse width of as short as 400fs. This technique will reduce the fabrication cost of the CNT based devices, especially optical devices.

Section 4.4 represents the optical reflectometry for precise control of CNT deposition by optical tweezers. Only by the technique which was employed in section 4.3, we could not detect when CNT deposition started and how much CNTs were deposited. We introduced optical reflectometry to detect them for estimation of CNT layer condition. FE-SEM images supported the validity of this technique.

In section 4.5, fabrication of CNT spheres by optical tweezers without templates or chemical functionalizations was investigated. Formation of CNT sphere and growing of CNT sphere was shown by microscope images. CNT spheres had quite high stability so that they could be physically manipulated and had elasticity. It is difficult to take them out from DMF, and Raman spectroscopy and FE-SEM could not be performed.

By using the tiny sphere inside the laser cavity, passively mode-locked fiber ring laser was successfully realized. We confirmed that the sphere includes CNTs by the result.

Chapter 5 : Summary

In this thesis, we focused on fabrication of silica-based waveguides by UV beam scanning and CNT optical devices for future highly functional devices. Hybridization of silica-based optical waveguides and CNT devices were investigated in order to achieve synergistic effects of the two and compensate their disadvantages with each other. Finally, we investigated an optical tweezers based novel handling method of CNTs to develop efficient fabrication of CNT optical devices.

In chapter 2, we presented the UV beam scanning technique and the functional device fabrication by the technique. Section 2.2 gave comparison between conventional process and UV beam scanning technique. Principle of the UV beam scanning technique, photosensitivity in Ge-doped silica-glass, were also introduced. Results which were obtained in chapter 2 are followings:

- In section 2.3, we studied structure characterization of silica-based optical channel waveguides fabricated by UV beam scanning technique. By using refracted near field method, we measured the cross sectional refractive index profiles of the waveguides which had been fabricated at the scanning speed of 1000, 500, 250, 100, 90, 80 ,70, 60, 50 ,40 , 30, 20, 10 μm/s. The maximum refractive index increase saturated at the scanning speed of 100μm/s. The horizontal and vertical refractive index distribution were found to be Gaussian and uniform profile, respectively. We defined the waveguide width as the horizontal full width of 1/e maximum at the mid-plane of the Ge-doped layer. With slow scanning speed, saturation of refractive index increase occurs at the center of the UV beam spot, whereas it does not occur at the other area. Hence, we can control effective channel width with the scanning speed.

- Section 2.4 focused the fabrication of Bragg grating based devices by using only UV beam scanning technique. Optical channel waveguides containing sampled

Bragg grating were fabricated, and multiple phase shift technique was introduced to densify the channel spacing. We fabricated 10mm-long waveguide which contains sampled grating constructed by 9 Bragg gratings with 1mm sampling period, and achieved maximum reflectivity of 99%. By introducing MPS technique, 100GHz channel spacing was halved to be 50GHz.

In chapter3, we investigated the combination of CNTs and planar waveguides fabricated by UV beam scanning. In section 3.2, basic properties, especially the optical properties, of CNTs were explained. The CNTs properties are determined solely by their chirality. Once chirality is determined, all CNTs properties can be calculated. There are two types of CNTs, semiconducting and metallic CNTs, and semiconducting CNTs absorb the light which has the same energy as bandgap. For optical device applications, the absorption characteristics have been mainly focused, and the absorption wavelength is almost inversely proportional to the CNTs diameters. CNTs reveal the saturable absorption characteristics for the absorption band and used as saturable absorber for passively mode locker. CNTs have another attractive characteristics for optical device application, high optical nonlinearity. Their high optical nonlinearity can shorten the nonlinear optical processing devices. Results which were obtained in chapter 3 are followings:

- In section 3.3, we proposed and demonstrated planar waveguide type saturable absorber based on CNTs. For future highly integrated CNT devices, planar waveguide type CNTs device is required. Since this is the first step of integrated CNTs device, we demonstrated saturable absorber which have been already realized function by CNTs. To realize the planar waveguide type device, interaction between CNTs and evanescent wave component was employed. By spraying purified CNTs onto the over-cladding-less silica-based planar waveguide which was fabricated by UV beam scanning, we fabricated the waveguide-type saturable absorber samples. The samples have large polarization dependence because of their device structures. We constructed passively mode-locked fiber laser by inserting the sample as a passive mode-locker, and obtained the pulse train which has 187fs temporal width

and 1.55MHz repetition rate.

- Section 3.4 focused on all optical switching using CNTs. High optical nonlinearity of CNTs was used to shorten the optical nonlinear processing device length. We introduced 10mm-long CNTs loaded over cladding less planar waveguide as a nonlinear device in NOLM configuration. By using 95:5 coupler, splitting ratio contrast of about 20% was realized, and this result well matches with theory. The nonlinear coefficient (γ) of the device was estimated to be in the order of $10^6 \mathrm{W}^{-1}\mathrm{km}^{-1}$ which is two magnitude smaller than the simulated value. However, considering the results in section 3.3 the estimated value was too high. The phase shifts might be induced by the thermal effect in addition to SPM. We have to take into account the polarization effects.

In chapter 4, optical tweezers was employed to solve a handling problem of CNTs for many applications. In section 4.2, the principle of optical tweezers was explained using simple ray optics. Optical radiation force which "push" an object will change into the force which "pull" or "trap" the object by focusing the light. Large divergence of optical intensity can trap the micro-, nano- materials at focusing point.

- In section 4.3, we proposed and demonstrated the deposition of CNTs onto optical fiber by optical tweezers. The light spreads out from the optical fiber end was used as an optical intensity divergence for optical tweezers. The experimental setup was very simple, composed only of a laser diode and an EDFA. We successfully deposited the CNTs onto the fiber end by injecting the light into CNT dispersed solution through a perpendicularly cleaved fiber end. Microscopic Raman spectroscopy proved the area selective CNT deposition only around the core region. Optimum optical intensity was found to be 21.5dBm for SMF, and 19.0dBm for DSF. The optimum intensity highly depends on the NA of the fibers and the condition of CNT dispersion. We also demonstrated a passively mode-locked fiber laser using a fiber whose one end was coated by CNTs with our technique. We generated short pulses with a temporal pulse width of as short as 400fs. This

technique will reduce the fabrication cost of the CNT based devices, especially optical devices. Results which were obtained in chapter 4 are followings:

- Section 4.4 represents the optical reflectometry for precise control of CNT deposition by optical tweezers. Only by the technique which was employed in section 4.3, we could not detect when CNT deposition started and how much CNTs were deposited. We introduced optical reflectometry to detect them for estimation of CNT layer condition. FE-SEM images supported the validity of this technique.

- In section 4.5, fabrication of CNT spheres by optical tweezers without templates or chemical functionalizations was investigated. Formation of CNT sphere and growing of CNT sphere was shown by microscope images. CNT spheres had quite high stability so that they could be physically manipulated and had elasticity. It is difficult to take them out from DMF, and Raman spectroscopy and FE-SEM could not be performed. By using the tiny sphere inside the laser cavity, passively mode-locked fiber ring laser was successfully realized. We confirmed that the sphere include CNTs by the result. The techniques which are reported in this chapter allow us to easily fabricated CNT based devices, especially optical applications.

We investigated both UV beam scanning technique and CNTs to achieve synergistic effects of the two, and examined optical tweezers to efficiently and easily fabricate the planar waveguide-type CNT devices. Although we could not realize the synergistic devices, we demonstrated the fundamental results. We believe that our results obtained in this thesis will contribute the future developments of optical communication researches.

Acknowledgements

This thesis is a work which is supported by many people. I would like to thank them all, but mentioning a few is allowed here.

First and foremost, I would like to express my best gratitude to my supervisor, Prof. Shinji Yamashita, for his continuous advice and guidance through my course of research. Challenging theme which he allocated me to have been developed my research ability. I also would like to thank for allowing me to use discretion of selecting research theme and deciding how to work on the research.

I would like to thank Prof. Kazuo Hotate for his precious advice. From the discussion with him, I got a lot of knowledge in broad fields. Especially, research theme of optical reflectometry would not appear in this thesis without discussions with him and his laboratory members. Prof. He also gave me a lot of precious advice.

I would like to thank Dr. Yoshinori Hibino, Dr. Yasuyuki Inoue, Dr. Masaki Kotoku and Mr. Yusuke Nasu in NTT photonics laboratories for offering silica on silicon thin film samples and their great advice. Study of structure characterization of UV-written silica-based waveguides is done by collaboration with Mr. Nasu.

I would like to thank Dr. Sze Yun Set, Dr. Chee Seong Goh and Mr. Hiroshi Yaguchi in Alnair Laboratories corporation for collaboration about carbon nanotube based optical device applications. This theme is very attractive and their cutting edge technology supported my research in this thesis.

For precious advices and discussions on the thesis, I would like to express my gratitude to Dr. Yong-Won Song and Dr. Kwang-Yong Song. Thanks are also gratefully extended to Dr. Shigeru Ohtsuka for his kind assistances in SEM operations.I would like to thank secretaries in Hotate, Yamashita and He laboratories, Ms. Michiko Masuhara, Ms. Noriko Wakabayashi, Ms. Kaoru Machida, and Ms. Noriko Mizuno for supporting our dairy life in laboratories.

I am grateful to all my current and former lab-mates, with whom I have fortunately been enjoying my research life here.

Finally, I would like to express my gratitude to my parents for their kind support to concentrate on my research and giving me an occasion to engage myself to working on fulfillment of this thesis.

References

[1] M. Nakazawa, T. Yamamoto, and K. Tamura, "1.28Tbit/s-70km OTDM transmission using third- and fourth-order simultaneous dispersion compensation with a phase modulator," *Electronics Letters*, Vol. 36, No. 24, pp. 2027 – 2029, 2000.

[2] H. Suzuki, J.-I. Kani, H. Masuda, N. Takachio, K. Iwatsuki, Y. Tada, and M. Sumida, "1-Tb/s (100 × 10 Gb/s) super-dense WDM transmission with 25-GHz channel spacing in the zero-dispersion region employing distributed Raman amplification technology," *IEEE Photonics Technology Letters*, Vol. 12, No. 7, pp. 903–905, 2000.

[3] H. Suzuki, N. Takachio, H. Masuda, and K. Iwatsuki, "Super-dense WDM transmission technology in the zero-dispersion region employing distributed Raman amplification," *Journal of Lightwave Technology*, Vol. 21, No. 4, pp. 973–981, 2003.

[4] A. Himeno, K. Kato, and T. Miya, "Silica-based planar lightwave circuits," *IEEE Journal of Selected Topics in Quantum Electronics*, Vol. 4, No. 6, pp. 913–924, 1998.

[5] M. Svalgaard, C. Poulsen, A. Bjarklev, and O. Poulsen, "Direct UV writing of buried singlemode channel waveguides in Ge-doped silica films," *Electronics Letters*, Vol. 30, No. 17, pp. 1401 – 1403, 1994.

[6] K. Hill, Y. Fujii, D. Johnson, and B. Kawasaki, "Photosensitivity in optical fibre waveguides: Application to reflection filter fabrication," *Applied Physics Letters*, Vol. 32, No. 10, pp. 647–649, 1978.

[7] T. Erdogan, "Fiber grating spectra," *Journal of Lightwave Technology*, Vol. 15, No. 8, pp. 1277 – 1294, 1997.

[8] A. Vengsarkar, P. Lemaire, J. Judkins, V. Bhatia, T. Erdogan, and J. Sipe, "Long-period fiber gratings as band-rejection filters," *Journal of Lightwave Technology*, Vol. 14, No. 1, pp. 58 – 65, 1996.

[9] M. Yanagisawa, T. Hashimoto, F. Ebisawa, T. Kitagawa, H. Takahashi, A. Himeno, A. Sugita, Y. Yamada, and K. Okamoto, "A 2.5 Gb/s hybrid integrated multiwavelength light source composed of eight DFB-LDs and an MMI coupler on a silica PLC platform," *24th European Conference on Optical Communication. ECOC '98*, Vol. 1, pp. 77 – 78, 1998.

[10] J. Albert, F. Bilodeau, D. Johnson, K. Hill, K. Hattori, T. Kitagawa, Y. Hibino, and M. Abe, "Low-loss planar lightwave circuit OADM with high isolation and no polarization dependence," *IEEE Photonics Technology Letters*, Vol. 11, No. 3, pp. 346 – 348, 1999.

[11] Y. Hibino, T. Kominato, and Y. Ohmori, "Optical frequency tuning by laser-irradiation in silica-based Mach-Zehnder-type multi/demultiplexers," *IEEE Photonics Technology Letters*, Vol. 3, No. 7, pp. 640 – 642, 1991.

[12] K. Takada, M. Abe, T. Shibata, and K. Okamoto, "Low-loss 10-GHz-spaced tandem multi/demultiplexer with more than 1000 channels using a 1 × 5 interference multi/demultiplexer as a primary filter," *IEEE Photonics Technology Letters*, Vol. 14, No. 1, pp. 59 – 61, 2002.

[13] V. Mizrahi, P. J. Lemaire, T. Erdogan, W. Reed, D. J. DiGiovanni, and R. M. Atkins, "Ultraviolet laser fabrication of ultrastrong optical fiber gratings and of germania-doped channel waveguides," *Applied Physics Letters*, Vol. 63, No. 13, pp. 1727 – 1729, 1993.

[14] G. Maxwell and B. Ainslie, "Demonstration of a directly written directional coupler using UV-induced photosensitivity in a planar silica waveguide," *Electronics Letters*, Vol. 31, No. 2, pp. 95 – 96, 1995.

[15] M. Svalgaard and M. Kristensen, "Directly UV written silica-on-silicon planar waveguides with low loss," *Electronics Letters*, Vol. 33, No. 10, pp. 861 – 863, 1997.

[16] D. Zauner, K. Kulstad, J. Rathje, and M. Svalgaard, "Directly UV-written silica-on-silicon planar waveguides with low insertion loss," *Electronics Letters*, Vol. 34, No. 16, pp. 1582 – 1584, 1998.

[17] K. Faerch and M. Svalgaard, "Symmetrical waveguide devices fabricated by direct UV writing," *IEEE Photonics Technology Letters*, Vol. 14, No. 2, pp. 173 – 175, 2002.

[18] M. Svalgaard, "Direct writing of planar waveguide power splitters and directional couplers using a focused ultraviolet laser beam," *Electronics Letters*, Vol. 33, No. 20, pp. 1694 – 1695, 1997.

[19] M. Olivero and M. Svalgaard, "Direct UV-written broadband directional planar waveguide couplers," *Optics Express*, Vol. 13, No. 21, pp. 8390–8399, 2005.

[20] M. Svalgaard, K. Faerch, and L.-U. Andersen, "Variable optical attenuator fabricated by direct UV writing," *Journal of Lightwave Technology*, Vol. 21, No. 9, pp. 2097 – 2103, 2003.

[21] G. Emmerson, S. Watts, C. Gawith, V. Albanis, M. Ibsen, R. Williams, and P. Smith, "Fabrication of directly UV-written channel waveguides with simultaneously defined integral Bragg gratings," *Electronics Letters*, Vol. 38, No. 24, pp. 1531 – 1532, 2002.

[22] Y. Sakakibara, S. Tatsuura, H. Kataura, M. Tokumoto, and Y. Achiba, "Near-infrared saturable absorption of single-wall carbon nanotubes prepared by laser ablation method," *Japanese Journal of Applied Physics, Part 2: Letters*, Vol. 42, No. 5 A, pp. 494 – 496, 2003.

[23] S. Y. Set, H. Yaguchi, Y. Tanaka, and M. Jablonski, "Laser Mode Locking Using a Saturable Absorber Incorporating Carbon Nanotubes," *Journal of Lightwave Technology*, Vol. 22, No. 1, pp. 51 – 56, 2004.

[24] S. Y. Set, H. Yaguchi, Y. Tanaka, and M. Jablonski, "Ultrafast fiber pulsed lasers incorporating carbon nanotubes," *IEEE Journal on Selected Topics in Quantum Electronics*, Vol. 10, No. 1, pp. 137 – 146, 2004.

[25] M. Kawachi, "Silica waveguides on silicon and their application to integrated-optic components," *Optical and Quantum Electronics*, Vol. 22, No. 5, pp. 391 – 416, 1990.

[26] D. K. W. Lam and B. K. Garside, "Characterization of single-mode optical fiber filters," *Applied Optics*, Vol. 20, No. 3, pp. 440 – 445, 1981.

[27] P. Lemaire, R. Atkins, V. Mizrahi, and W. Reed, "High pressure H_2 loading as a technique for achieving ultrahigh UV photosensitivity and thermal sensitivity in GeO_2 doped optical fibres," *Electronics Letters*, Vol. 29, No. 13, pp. 1191 – 1193, 1993.

[28] M. Douay, W. Xie, T. Taunay, P. Bernage, P. Niay, P. Cordier, B. Poumellec, L. Dong, J. Bayon, H. Poignant, and E. Delevaque, "Densification involved in the UV-based photosensitivity of silica glasses and optical fibers," *Journal of Lightwave Technology*, Vol. 15, No. 8, pp. 1329 – 1342, 1997.

[29] K. Awazu, H. Kawazoe, and M. Yamane, "Simultaneous generation of optical absorption bands at 5.14 and 0.452 eV in nine SiO_2:GeO_2 glasses heated under an H_2 atmosphere," *Journal of Applied Physics*, Vol. 68, No. 6, pp. 2713 – 2718, 1990.

[30] L. Dong, J. Archambault, L. Reekie, P. Russell, and D. Payne, "Photoinduced absorption change in germanosilicate preforms: evidence for the color-center model of photosensitivity," *Applied Optics*, Vol. 34, No. 18, pp. 3436 – 3440, 1995.

[31] B. Poumellec, P. Niay, M. Douay, and J. Bayon, "UV-induced refractive index grating in Ge:SiO_2 preforms: additional CW experiments and the macroscopic

origin of the change in index," *Journal of Physics D: Applied Physics*, Vol. 29, No. 7, pp. 1842–1856, 1996.

[32] M. Svalgaard, S. Madsen, J. Hvam, and M. Kristensen, "Direct characterization of ultraviolet-light-induced refractive index structures by scanning near-field optical microscopy," *IEEE Photonics Technology Letters*, Vol. 10, No. 6, pp. 848–850, 1998.

[33] M. Svalgaard, "Effect of D¡sub¿2¡/sub¿ outdiffusion on direct UV writing of optical waveguides," *Electronics Letters*, Vol. 35, No. 21, pp. 1840 – 1842, 1999.

[34] L. Leick, A. Harpoth, and M. Svalgaard, "Empirical model for the waveguiding properties of directly UV-written waveguides," *Applied Optics*, Vol. 41, No. 21, pp. 4325–4330, 2002.

[35] K. White, "Practical application of the refracted near-field technique for the measurement of optical fibre refractive index profiles," *Optical and Quantum Electronics*, Vol. 11, No. 2, pp. 185 – 196, 1979.

[36] P. Oberson, B. Gisin, B. Huttner, and N. Gisin, "Refracted near-field measurements of refractive index and geometry of silica-on-silicon integrated optical waveguides," *Applied Optics*, Vol. 37, No. 31, pp. 7268 – 7272, 1998.

[37] M. Ibsen, M. K. Durkin, M. J. Cole, and R. I. Laming, "Sinc-sampled fiber Bragg gratings for identical multiple wavelength operation," *IEEE Photonics Technology Letters*, Vol. 10, No. 6, pp. 842–844, 1998.

[38] W. Loh, F. Zhou, and J. Pan, "Novel designs for sampled grating-based multiplexers-demultiplexers," *Optics Letters*, Vol. 24, No. 21, pp. 1457–1459, 1999.

[39] F. Ouellette, P. Krug, T. Stephens, G. Dhosi, and B. Eggleton, "Broadband and WDM dispersion compensation using chirped sampled fibre Bragg gratings," *Electronics Letters*, Vol. 31, No. 11, pp. 899–901, 1995.

[40] W. Loh, F. Zhou, and J. Pan, "Sampled fiber grating based-dispersion slope compensator," *IEEE Photonics Technology Letters*, Vol. 11, No. 10, pp. 1280–1282, 1999.

[41] X.-F. Chen, X.-H. Li, L. Xia, S.-Z. Xie, C.-C. Fan, and J.-P. Wang, "Experimental investigation of a sampled grating with a chirp in the sampling period," *Microwave and Optical Technology Letters*, Vol. 29, No. 2, pp. 128–130, 2001.

[42] Y. Nasu and S. Yamashita, "Densification of sampled fiber Bragg gratings using multiple-phase-shift (MPS) technique," *Journal of Lightwave Technology*, Vol. 23, No. 4, pp. 1808 – 1817, 2005.

[43] B. Malo, S. Theriault, D. Johnson, F. Bilodeau, J. Albert, and K. Hill, "Apodised in-fibre Bragg grating reflectors photoimprinted using a phase mask," *Electronics Letters*, Vol. 31, No. 3, pp. 223 – 225, 1995.

[44] J. Albert, K. Hill, B. Malo, S. Theriault, F. Bilodeau, D. Johnson, and L. Erickson, "Apodisation of the spectral response of fibre Bragg gratings using a phase mask with variable diffraction efficiency," *Electronics Letters*, Vol. 31, No. 3, pp. 222 – 223, 1995.

[45] M. Cole, W. Loh, R. Laming, M. Zervas, and S. Barcelos, "Moving fibre/phase mask-scanning beam technique for enhanced flexibility in producing fibre gratings with uniform phase mask," *Electronics Letters*, Vol. 31, No. 17, pp. 1488 – 1490, 1995.

[46] R. Kashyap, J. Armitage, R. Wyatt, S. Davey, and D. Williams, "All-fibre narrowband reflection gratings at 1500 nm," *Electronics Letters*, Vol. 26, No. 11, pp. 730 – 732, 1990.

[47] Y.-W. Song, S. Y. Set, S. Yamashita, C. S. Goh, and T. Kotake, "1300-nm pulsed fiber lasers mode-locked by purified carbon nanotubes," *IEEE Photonics Technology Letters*, Vol. 17, No. 8, pp. 1623 – 1625, 2005.

[48] V. A. Margulis, E. Gaiduk, and E. Zhidkin, "Third-order optical nonlinearity of semiconductor carbon nanotubes third harmonic generation," *Diamond and Related Materials*, Vol. 8, No. 7, pp. 1240 – 1245, 1999.

[49] Y.-C. Chen, N. Raravikar, L. Schadler, P. Ajayan, Y.-P. Zhao, T.-M. Lu, G.-C. Wang, and X.-C. Zhang, "Ultrafast optical switching properties of single-wall carbon nanotube polymer composites at 1.55 μm," *Applied Physics Letters*, Vol. 81, No. 6, pp. 975–977, 2002.

[50] M. Ichida, Y. Hamanaka, H. Kataura, Y. Achiba, and A. Nakamura, "Ultrafast relaxation dynamics of photoexcited states in semiconducting single-walled carbon nanotubes," *Physica B: Condensed Matter*, Vol. 323, No. 1-4, pp. 237 – 238, 2002.

[51] S. Tatsuura, M. Furuki, Y. Sato, I. Iwasa, M. Tian, and H. Mitsu, "Semiconductor carbon nanotubes as ultrafast switching materials for optical telecommunications," *Advanced Materials*, Vol. 15, No. 6, pp. 534 – 537, 2003.

[52] S. Yamashita, Y. Inoue, S. Maruyama, Y. Murakami, H. Yaguchi, M. Jablonski, and S. Set, "Saturable absorbers incorporating carbon nanotubes directly synthesized onto substrates and fibers and their application to mode-locked fiber lasers," *Optics Letters*, Vol. 29, No. 14, pp. 1581 – 1583, 2004.

[53] Y. Sakakibara, A. G. Rozhin, H. Kataura, Y. Achiba, and M. Tokumoto, "Carbon nanotube-poly(vinylalcohol) nanocomposite film devices: Applications for femtosecond fiber laser mode lockers and optical amplifier noise suppressors," *Japanese Journal of Applied Physics, Part 1: Regular Papers and Short Notes and Review Papers*, Vol. 44, No. 4 A, pp. 1621 – 1625, 2005.

[54] H. Kroto, J. Heath, S. O'Brien, R. Curl, and R. Smalley, "C_{60}: Buckminsterfullerene," *Nature*, Vol. 318, No. 6042, pp. 162–163, 1985.

[55] S. Iijima, "Helical microtubules of graphitic carbon," *Nature*, Vol. 354, No. 6348, pp. 56–58, 1991.

[56] R. Saito, M. Fujita, G. Dresselhaus, and M. Dresselhaus, "Electronic structure of chiral graphene tubules," *Applied Physics Letters*, Vol. 60, No. 18, pp. 2204 – 2206, 1992.

[57] T. Guo, P. Nikolaev, A. Thess, D. Colbert, and R. Smalley, "Catalytic growth of single-walled nanotubes by laser vaporization," *Chemical Physics Letters*, Vol. 243, No. 1-2, pp. 49 – 54, 1995.

[58] C. Journet, W. K. Maser, P. Bernier, A. Loiseau, M. L. de la Chapelle, S. Lefrant, P. Deniard, R. Lee, and J. E. Fischer, "Large-scale production of single-walled carbon nanotubes by the electric-arc technique," *Nature*, Vol. 388, No. 6644, pp. 756–758, 1997.

[59] H. Dai, A. Rinzler, P. Nikolaev, A. Thess, D. Colbert, and R. Smalley, "Single-wall nanotubes produced by metal-catalyzed disproportionation of carbon monoxide," *Chemical Physics Letters*, Vol. 260, No. 3-4, pp. 471 – 475, 1996.

[60] B. Satishkumar, A. Govindaraj, R. Sen, and C. Rao, "Single-walled nanotubes by the pyrolysis of acetylene-organometallic mixtures," *Chemical Physics Letters*, Vol. 293, No. 1-2, pp. 47 – 52, 1998.

[61] S. Bandow, S. Asaka, X. Zhao, and Y. Ando, "Purification and magnetic properties of carbon nanotubes," *Applied Physics A: Materials Science & Processing*, Vol. 67, No. 1, pp. 23 – 27, 1998.

[62] K. Morishita and T. Takarada, "Scanning electron microscope observation of the purification behaviour of carbon nanotubes," *Journal of Materials Science*, Vol. 34, No. 6, pp. 1169 – 1174, 1999.

[63] I. Chiang, B. Brinson, A. Huang, P. Willis, M. Bronikowski, J. Margrave, R. Smalley, and R. Hauge, "Purification and characterization of single-wall carbon nanotubes (SWNTs) obtained from the gas-phase decomposition of CO (HiPco process)," *Journal of Physical Chemistry B*, Vol. 105, No. 35, pp. 8297 – 8301, 2001.

[64] J.-F. Colomer, P. Piedigrosso, A. Fonseca, and J. Nagy, "Different purification methods of carbon nanotubes produced by catalytic synthesis," *Synthetic Metals*, Vol. 103, No. 1-3 pt 3, pp. 2482 – 2483, 1999.

[65] X. Bai, D. Li, D. Du, H. Zhang, L. Chen, and J. Liang, "Laser irradiation for purification of aligned carbon nanotube films," *Carbon*, Vol. 42, No. 10, pp. 2125 – 2127, 2004.

[66] T.-J. Park, S. Banerjee, T. Hemraj-Benny, and S. S. Wong, "Purification strategies and purity visualization techniques for single-walled carbon nanotubes," *Journal of Materials Chemistry*, Vol. 16, No. 2, pp. 141 – 154, 2006.

[67] P. Nikolaev, M. Bronikowski, K. Bradley, F. Rohmund, D. Colbert, K. Smith, and R. Smalley, "Gas-phase catalytic growth of single-walled carbon nanotubes from carbon monoxide," *Chemical Physics Letters*, Vol. 313, No. 1-2, pp. 91 – 97, 1999.

[68] S. Maruyama, R. Kojima, Y. Miyauchi, S. Chiashi, and M. Kohno, "Low-temperature synthesis of high-purity single-walled carbon nanotubes from alcohol," *Chemical Physics Letters*, Vol. 360, No. 3-4, pp. 229 – 234, 2002.

[69] S. Tans, M. Devoret, H. Dai, A. Thess, R. Smalley, L. Georliga, and C. Dekker, "Individual single-wall carbon nanotubes as quantum wires," *Nature*, Vol. 386, No. 6624, pp. 474 – 477, 1997.

[70] R. Martel, T. Schmidt, H. Shea, T. Hertel, and P. Avouris, "Single- and multi-wall carbon nanotube field-effect transistors," *Applied Physics Letters*, Vol. 73, No. 17, pp. 2447 – 2449, 1998.

[71] V. Derycke, R. Martel, J. Appenzeller, and P. Avouris, "Carbon nanotube inter- and intramolecular logic gates," *Nano Letters*, Vol. 1, No. 9, pp. 453 – 456, 2001.

[72] Y. Saito, K. Hata, and T. Murata, "Field emission patterns originating from pentagons at the tip of a carbon nanotube," *Japanese Journal of Applied Physics, Part 2: Letters*, Vol. 39, No. 4A, pp. 271–272, 2000.

[73] N. Lee, D. Chung, I. Han, J. Kang, Y. Choi, H. Kim, S. Park, Y. Jin, W. Yi, M. Yun, J. Jung, C. Lee, J. You, S. Jo, C. Lee, and J. Kim, "Application of carbon nanotubes to field emission displays," *Diamond and Related Materials*, Vol. 10, No. 2, pp. 265 – 270, 2001.

[74] M. Yasutake, Y. Shirakawabe, T. Okawa, S. Mizooka, and Y. Nakayama, "Performance of the carbon nano-tube assembled tip for surface shape characterization," *Ultramicroscopy*, Vol. 91, No. 1-4, pp. 57–62, 2002.

[75] Q. Ye, A. Cassell, H. Liu, K.-J. Chao, J. Han, and M. Meyyappan, "Large-scale fabrication of carbon nanotube probe tips for atomic force microscopy critical dimension imaging applications," *Nano Letters*, Vol. 4, No. 7, pp. 1301 – 1308, 2004.

[76] H. Kataura, Y. Kumazawa, Y. Maniwa, I. Umezu, S. Suzuki, Y. Ohtsuka, and Y. Achiba, "Optical properties of single-wall carbon nanotubes," *Synthetic Metals*, Vol. 103, No. 1-3 pt 3, pp. 2555 – 2558, 1999.

[77] I. Rubtsov, R. Russo, T. Albers, P. Deria, D. Luzzi, and M. Therien, "Visible and near-infrared excited-state dynamics of single-walled carbon nanotubes," *Applied Physics A: Materials Science and Processing*, Vol. 79, No. 7, pp. 1747 – 1751, 2004.

[78] V. Margulis and T. Sizikova, "Theoretical study of third-order nonlinear optical response of semiconductor carbon nanotubes," *Physica B: Condensed Matter*, Vol. 245, No. 2, pp. 173 – 189, 1998.

[79] M. Ichida, S. Mizuno, Y. Saito, H. Kataura, Y. Achiba, and A. Nakamura, "Coulomb effects on the fundamental optical transition in semiconducting single-walled carbon nanotubes: Divergent behavior in the small-diameter limit," *Physical Review B (Condensed Matter and Materials Physics)*, Vol. 65, No. 24, p. 241407, 2002.

[80] M. Ichida, S. Mizuno, H. Kataura, Y. Achiba, and A. Nakamura, "Anisotropic optical properties of mechanically aligned single-walled carbon nanotubes in

polymer," *Applied Physics A: Materials Science and Processing*, Vol. 78, No. 8, pp. 1117 – 1120, 2004.

[81] Y. Murakami, E. Einarsson, T. Edamura, and S. Maruyama, "Polarization dependence of the optical absorption of single-walled carbon nanotubes," *Physical Review Letters*, Vol. 94, No. 8, p. 087402, 2005.

[82] E. Greer, Y. Kimura, K. Suzuki, E. Yoshida, and M. Nakazawa, "Generation of 1.2ps, 10 GHz pulse train from all-optically modelocked, erbium fibre ring laser with active nonlinear polarization rotation," *Electronics Letters*, Vol. 30, No. 21, pp. 1764–1765, 1994.

[83] S. Pan and C. Lou, "Stable multiwavelength dispersion-tuned actively mode-locked erbium-doped fiber ring laser using nonlinear polarization rotation," *IEEE Photonics Technology Letters*, Vol. 18, No. 13, pp. 1451 – 1453, 2006.

[84] H. Ajiki and T. Ando, "Aharonov-Bohm effect in carbon nanotubes," *Physica B: Condensed Matter*, Vol. 201, pp. 349 – 352, 1994.

[85] N. Doran and D. Wood, "Nonlinear-optical loop mirror," *Optics Letters*, Vol. 13, No. 1, pp. 56 – 58, 1988.

[86] V. Margulis, E. Gaiduk, and E. Zhidkin, "Electric-field-induced optical second-harmonic generation and nonlinear optical rectification in semiconducting carbon nanotubes," *Optics Communications*, Vol. 183, No. 1, pp. 317 – 326, 2000.

[87] G. Guo, K. Chu, D. sheng Wang, and C. gang Duan, "Linear and nonlinear optical properties of carbon nanotubes from first-principles calculations," *Physical Review B (Condensed Matter and Materials Physics)*, Vol. 69, No. 20, p. 205416, 2004.

[88] A. Ashkin, "Trapping of atoms by resonance radiation pressure," *Physical Review Letters*, Vol. 40, No. 12, pp. 729 – 732, 1978.

[89] A. Ashkin, J. Dziedzic, J. Bjorkholm, and S. Chu, "Observation of a single-beam gradient force optical trap for dielectric particles," *Optics Letters*, Vol. 11, No. 5,

pp. 288 – 290, 1986.

[90] Y. Tajitsu, M. Kanesaki, M. Tsukiji, K. Imoto, M. Date, and E. Fukada, "Novel tweezers for biological cells using piezoelectric polylactic acid fibers," *Ferroelectrics*, Vol. 320, pp. 133–139, 2005.

[91] C.-H. Chiou, Y.-Y. Huang, M.-H. Chiang, H.-H. Lee, and G.-B. Lee, "New magnetic tweezers for investigation of the mechanical properties of single DNA molecules," *Nanotechnology*, Vol. 17, No. 5, pp. 1217 – 1224, 2006.

[92] M. Friese, H. Rubinsztein-Dunlop, J. Gold, P. Hagberg, and D. Hanstorp, "Optically driven micromachine elements," *Applied Physics Letters*, Vol. 78, No. 4, pp. 547–549, 2001.

[93] M. Barbic, "Magnetic wires in MEMS and bio-medical applications," *Journal of Magnetism and Magnetic Materials*, Vol. 249, No. 1-2, pp. 357 – 367, 2002.

[94] D. G. Grier, "A revolution in optical manipulation," *Nature*, Vol. 424, No. 6950, pp. 810–816, 2003.

[95] E. Dufresne, G. Spalding, M. Dearing, S. Sheets, and D. Grier, "Computer-generated holographic optical tweezer arrays," *Review of Scientific Instruments*, Vol. 72, No. 3, pp. 1810 – 1816, 2001.

[96] H. W. Postma, A. Sellmeijer, and C. Dekker, "Manipulation and imaging of individual single-walled carbon nanotubes with an atomic force microscope," *Advanced Materials*, Vol. 12, No. 17, pp. 1299–1302, 2000.

[97] X. Chen, T. Saito, H. Yamada, and K. Matsushige, "Aligning single-wall carbon nanotubes with an alternating-current electric field," *Applied Physics Letters*, Vol. 78, No. 23, pp. 3714–3715, 2001.

[98] B. Smith, Z. Benes, D. Luzzi, J. Fischer, D. Walters, M. Casavant, J. Schmidt, and R. Smalley, "Structural anisotropy of magnetically aligned single wall carbon nanotube films," *Applied Physics Letters*, Vol. 77, No. 5, pp. 663–, 2000.

[99] J. Plewa, E. Tanner, D. M. Mueth, and D. G. Grier, "Processing carbon nanotubes with holographic optical tweezers," *Optics Express*, Vol. 12, No. 9, pp. 1978 – 1981, 2004.

[100] S. Tan, H. Lopez, C. Cai, and Y. Zhang, "Optical trapping of single-walled carbon nanotubes," *Nano Letters*, Vol. 4, No. 8, pp. 1415 – 1419, 2004.

[101] J. Zhang, H. I. Kim, C. H. Oh, X. Sun, and H. Lee, "Multidimensional manipulation of carbon nanotube bundles with optical tweezers," *Applied Physics Letters*, Vol. 88, No. 5, p. 053123, 2006.

[102] J. Zhang, H. I. Kim, X. Sun, C. H. Oh, and H. Lee, "Optical trapping carbon nanotubes," *Colloids and Surfaces A: Physicochemical and Engineering Aspects*, Vol. 284-285, pp. 369 – 372, 2006.

[103] V. Margulis and E. Gaiduk, "Nature of near-infrared absorption in single-wall carbon nanotubes," *Physics Letters A*, Vol. 281, No. 1, pp. 52 – 58, 2001.

[104] A. Rao, E. Richter, S. Bandow, B. Chase, P. Eklund, K. Williams, S. Fang, K. Subbaswamy, M. Menon, A. Thess, R. Smalley, G. Dresselhaus, and M. Dresselhaus, "Diameter-selective Raman scattering from vibrational modes in carbon nanotubes," *Science*, Vol. 275, No. 5297, pp. 187 – 191, 1997.

[105] M. Dresselhaus and P. Eklund, "Phonons in carbon nanotubes," *Advances in Physics*, Vol. 49, No. 6, pp. 705 – 814, 2000.

[106] H. Li, K. Yue, Z. Lian, Y. Zhan, L. Zhou, S. Zhang, Z. Shi, Z. Gu, B. Liu, R. Yang, H. Yang, G. Zou, Y. Zhang, and S. Iijima, "Temperature dependence of the Raman spectra of single-wall carbon nanotubes," *Applied Physics Letters*, Vol. 76, No. 15, pp. 2053 – 2055, 2000.

[107] Q. Zhang, D. Yang, S. Wang, S. Yoon, and J. Ahn, "Influences of temperature on the Raman spectra of single-walled carbon nanotubes," *Smart Materials and Structures*, Vol. 15, No. 1, pp. 1–4, 2006.

[108] K. Strong, D. Anderson, K. Lafdi, and J. Kuhn, "Purification process for single-wall carbon nanotubes," *Carbon*, Vol. 41, No. 8, pp. 1477 – 1488, 2003.

[109] D.-H. Kim, H.-S. Jang, C.-D. Kim, D.-S. Cho, H.-D. Kang, J.-G. Jee, and H.-R. Lee, "In situ monitoring of carbon nanotube growth," *Carbon*, Vol. 41, No. 3, pp. 583–585, 2003.

[110] B. Panella, M. Hirscher, and S. Roth, "Hydrogen adsorption in different carbon nanostructures," *Carbon*, Vol. 43, No. 10, pp. 2209 – 2214, 2005.

[111] Y. Kojima, Y. Kawai, A. Koiwai, N. Suzuki, T. Haga, T. Hioki, and K. Tange, "Hydrogen adsorption and desorption by carbon materials," *Journal of Alloys and Compounds*, Vol. 421, No. 1-2, pp. 204–208, 2006.

[112] M. Sano, A. Kamino, J. Okamura, and S. Shinkai, "Ring closure of carbon nanotubes," *Science*, Vol. 293, No. 5533, pp. 1299 – 1301, 2001.

[113] M. Sano, A. Kamino, and S. Shinkai, "Construction of carbon nanotube "stars" with dendrimers," *Angewandte Chemie - International Edition*, Vol. 40, No. 24, pp. 4661 – 4663, 2001.

[114] M. Sano, A. Kamino, J. Okamura, and S. Shinkait, "Noncovalent self-assembly of carbon nanotubes for construction of "cages"," *Nano Letters*, Vol. 2, No. 5, pp. 531 – 533, 2002.

List of Figures

List of Publications

Publications :

1. Shinji Yamashita, Teruyuki Baba, and **Ken Kashiwagi**, "Frequency-shifted multiwavelength fiber Bragg grating laser sensor," *Japanese Journal of Applied Physics, Part 1 (Regular Papers, Short Notes & Review Papers*, Vol. 43, No. 12, pp. 8322–8324, 2004.

2. **Ken Kashiwagi** and Shinji Yamashita, "Fabrication of silica-based glass optical waveguide by UV beam scanning," *Japanese Journal of Applied Physics, Part 1 (Regular Papers, Short Notes & Review Papers)*, Vol. 43, No. 8B, pp. 5850 – 5853, 2004.

3. **Ken Kashiwagi**, Shinji Yamashita, Yusuke Nasu, Hiroshi Yaguchi, Chee Seong Goh, and Sze Yun Set, "Planar waveguide-type saturable absorber based on carbon nanotubes," *Applied Physics Letters*, Vol. 89, No. 8, pp. 081125, 2006.

International Conferences:

1. Shinji Yamashita, Teruyuki Baba, and **Ken Kashiwagi**, "Frequency-shifted multiwavelength FBG laser sensor," In *2002 15th Optical Fiber Sensors Conference Technical Digest. OFS 2002*, Vol. 1, pp. 285 – 288, Portland, OR, USA, 2002.

2. **Ken Kashiwagi** and Shinji Yamashita, "Fabrication of Silica-based glass optical waveguide by UV beam scanning," In *9th Microoptics Conference (MOC 2003)*, No. H-46, Odaiba, Tokyo, 2003.

3. **Ken Kashiwagi** and Shinji Yamashita, "Fabrication of Silica-based Optical Channel Waveguide Containing Long Period Grating by UV Beam Scanning,"

In *The 9th OptoElectronics and Communications Conference (OECC2004)*, No. 15F3-2, Yokohama, Kanagawa, 2004.

4. **Ken Kashiwagi**, Yusuke Nasu, and Shinji Yamashita, "Characterization of Silica-Based Channel Waveguides Fabricated by UV Beam Scanning," In *The 10th OptoElectronics and Communications Conference (OECC2005)*, No. 5E1-6, Seoul, Korea, 2005.

5. **Ken Kashiwagi**, Shinji Yamashita, Yusuke Nasu, Hiroshi Yaguchi, Chee Seong Goh, and Sze Yun Set, "Waveguide-type saturable absorber based on carbon nanotubes," In *31st European Conference on Optical Communication (ECOC 2005)*, Vol. 3, pp. 517 – 518, Glasgow, UK, 2005.

6. **Ken Kashiwagi**, Shinji Yamashita, Hiroshi Yaguchi, Chee Seong Goh, and Sze Yun Set, "All Optical Switching Using Carbon Nanotubes Loaded Planar Waveguide," In *The Conference on Lasers and Electro-Optics (CLEO 2006)*, No. CMA5, 2006.

7. **Ken Kashiwagi**, and Shinji Yamashita, "Fabrication of Silica-Based Optical Channel Waveguide Containing Sampled Grating by UV Beam Scanning," In *The 11th OptoElectronics and Communications Conference (OECC2006)*, No. 7B1-1, Kaoshung, Taiwan, 2006.

8. **Ken Kashiwagi**, Shinji Yamashita, Hiroshi Yaguchi, Chee Seong Goh, and Sze Yun Set, "Novel Cost Effective Carbon Nanotubes Deposition Technique Using Optical Tweezer Effect," In *Photonics West 2007*, No. 6478-15, San Jose, California, USA, 2007.

9. **Ken Kashiwagi** and Shinji Yamashita, "Fabrication of Silica-Based Optical Waveguide Containing Densified Sampled Grating by UV Beam Scanning," In *Optical Fiber Communication Conference (OFC) 2007*, No. OThU2, Anaheim, California, USA, 2007.

10. **Ken Kashiwagi**, Shinji Yamashita, and Sze Yun Set. "Optical Reflectometry for In-situ Monitoring of Carbon Nanotubes Deposition by Optical Tweezers," In *The Conference on Lasers and Electro-Optics (CLEO 2007)*, Baltimore, Maryland, USA, 2007. submitted.

Domestic Conferences:

1. Shinji Yamashita, Teruyuki Baba, and **Ken Kashiwagi**, "Frequency-shifted multiwavelength FBG laser sensor," In *Institute of Electronics, Information and Communication Engineers(IEICE), General Conference 2002*, No. B-13-14, 2002. (in Japanese)
(山下真司, 馬場輝幸, **柏木謙**, "周波数シフト型多波長光ファイバグレーティングレーザセンサ," 2002 年 電子情報通信学会 総合大会, No. B-13-14, 2002.)

2. **Ken Kashiwagi**, and Shinji Yamashita, "Fabrication of planar waveguides by UV beam scanning," In *Institute of Electronics, Information and Communication Engineers(IEICE), General Conference 2003*, No. C-3-76, 2003. (in Japanese)
(**柏木謙**, 山下真司, "UV 光照射による光導波路の作製," 2003 年 電子情報通信学会 総合大会, No. C-3-76, 2003.)

3. **Ken Kashiwagi** and Shinji Yamashita, "Simultaneous fabrication of channel waveguide and Bragg grating by UV beam scanning through a phase mask," In *Institute of Electronics, Information and Communication Engineers(IEICE), Electronics Society Conference 2003*, No. C-3-68, 2003. (in Japanese)
(**柏木謙**, 山下真司, "位相マスクを用いた UV 光照射によるブラッググレーティングと光導波路の同時作製," 2003 年電子情報通信学会ソサイエティ大会, No. C-3-68, 2003.)

4. **Ken Kashiwagi**, and Shinji Yamashita, "Fabrication of Optical Channel Waveguide Containing Long Period Grating by UV Beam Scanning," In *Institute of Electronics, Information and Communication Engineers(IEICE), General*

Conference 2004, No. C-3-149, 2004. (in Japanese)
(**柏木謙**, 山下真司, “UV 光照射による石英系光導波路作製技術を利用した長周期グレーティング導波路の作製,” 2004 年 電子情報通信学会 総合大会, No. C-3-149, 2004.)

5. **Ken Kashiwagi**, and Shinji Yamashita, “Fabrication of Silica-Based Grating Assisted Codirectional Coupler by UV Beam Scanning,” In *Institute of Electronics, Information and Communication Engineers(IEICE), Electronics Society Conference 2004*, No. C-3-47, 2004. (in Japanese)
(**柏木謙**, 山下真司, “UV 光照射による石英系光導波路作製技術を利用した GACC の作製,” 2004 年 電子情報通信学会 ソサイエティ大会, No. C-3-47, 2004.)

6. **Ken Kashiwagi**, Yusuke Nasu, and Shinji Yamashita, “Characterization of Silica-Based Channel Waveguides Fabricated by UV Beam Scanning,” In *Institute of Electronics, Information and Communication Engineers(IEICE), General Conference 2005*, No. C-3-12, 2005. (in Japanese)
(**柏木謙**, 那須悠介, 山下真司, “UV 光照射により作製した石英系光導波路構造の解析,” 2005 年 電子情報通信学会 総合大会, No. C-3-12, 2005.)

7. **Ken Kashiwagi**, Shinji Yamashita, Yusuke Nasu, Hiroshi Yaguchi, Chee Seong Goh, and Sze Yun Set, “Waveguide-Type Saturable Absorber Based on Carbon Nanotubes,” In *Institute of Electronics, Information and Communication Engineers(IEICE), Electronics Society Conference 2005*, No. C-3-69, 2005. (in Japanese)
(**柏木謙**, 山下真司, 那須悠介, 矢口寛, ゴー チーション, セット ジイヨン, “カーボンナノチューブを用いた導波路型可飽和吸収素子,” 2005 年 電子情報通信学会 ソサイエティ大会, No. C-3-69, 2005.)

8. **Ken Kashiwagi**, Shinji Yamashita, Hiroshi Yaguchi, Chee Seong Goh, and Sze Yun Set, “All Optical Switching Using Carbon Nanotubes Loaded Planar Waveguide,” In *Institute of Electronics, Information and Communication Engineers(IEICE), General Conference 2006*, No. C-3-12, 2006. (in Japanese)

(柏木謙, 山下真司, 矢口寛, ゴー チーション, セット ジイヨン, “カーボンナノチューブ蒸着平面導波路を用いた全光型スイッチング,” 2006 年 電子情報通信学会 総合大会, No. C-3-12, 2006.)

9. **Ken Kashiwagi**, and Shinji Yamashita, “Fabrication of Silica-Based Optical Channel Waveguide Containing Sampled Grating by UV Beam Scanning,” In *Institute of Electronics, Information and Communication Engineers(IEICE), Electronics Society Conference 2006*, No. C-3-16, 2006. (in Japanese)
(**柏木謙**, 山下真司, “紫外光照射による石英系導波路作製技術を用いたサンプルトグレーティング導波路の作製,” 2006 年 電子情報通信学会 ソサイエティ大会, No. C-3-16, 2006.)

Meetings :

1. Shinji Yamashita, Teruyuki Baba, and **Ken Kashiwagi**, “Frequency shifted multiwavelength FBG laser sensor,” In *28th Meeting of Lightwave Sensing and Technology*, No. LST28-8, 2001. (in Japanese)
(山下真司, 馬場輝幸, **柏木謙**, “周波数シフト型多波長光ファイバグレーティングレーザセンサ,”. 第 28 回光波センシング技術研究会, No. LST28-8, 2001.)

2. **Ken Kashiwagi**, and Shinji Yamashita, “Fabrication of functional silica-based glass optical channel waveguide by UV beam scanning,” In *Meeting of Optoelectronics, Institute of Electronics, Information and Communication Engineers(IEICE) technical report*, No. OPE2004-123, 2004. (in Japanese)
(**柏木謙**, 山下真司, “UV 光照射による高機能石英系光導波路の作製,” 2004 年 電子情報通信学会 光エレクトロニクス (OPE) 研究会, No. OPE2004-123, 2004.)

3. **Ken Kashiwagi**, Shinji Yamashita, Yusuke Nasu, Chee Seong Goh, and Sze Yun Set, “Waveguide-type saturable absorber based on carbon nanotubes,” In *Meeting of Optoelectornics, Institute of Electronics, Information and Communication Engineers(IEICE) technical report*, No. OPE2005-67, 2005. (in Japanese)
(**柏木謙**, 山下真司, 那須悠介, 矢口寛, ゴー チー ション, セット ジ イヨン, “カー

ボンナノチューブを用いた導波路型可飽和吸収素子," 2005 年 電子情報通信学会光エレクトロニクス (OPE) 研究会, No. OPE2005-67, 2005.)

Others :

1. Shinji Yamashita, **Ken Kashiwagi** and Sze Yun Set, "Optical devices utilizing interaction between evanecent wave and carbon nanotubes," Japanese Patent 2005-258172, 6th Sep. 2005. (in Japanese) (山下真司, **柏木謙**, セット ジイヨン. "エバネッセント波とＣＮＴとの相互作用を利用した光デバイス," 2005. 特願 2005-258172, 2005/09/06.)

2. **Ken Kashiwagi**, Shinji Yamashita and Sze Yun Set, "Optical devices utilizing interaction between evanecent wave and carbon nanotubes," Third The University of Tokyo Student Invention Award, Encouragement Prize, 2006. (in Japanese) (**柏木謙**, 山下真司, セット ジイヨン. "エバネッセント波とカーボンナノチューブとの相互作用を利用した光デバイス," 第 3 回 東京大学 学生発明コンテスト 奨励賞, 2006.)